UNIVERSIDADE DE LISBOA
FACULDADE DE CIÊNCIAS
DEPARTAMENTO DE QUÍMICA E BIOQUÍMICA

Magnetic Properties of First-row Transition Metal Compounds with Different Nuclearities

Frederico de Lacerda Ferreira dos Santos Martins

Mestrado em Química
Especialização em Química

Dissertação orientada por:
Dr Paulo Nuno Martinho

2018

Agradecimentos

Gostaria de agradecer, em primeiro lugar, ao Dr Paulo Martinho, pela oportunidade de trabalhar, uma vez mais, num dos seus projectos e por toda a sua orientação pessoal e profissional ao longo deste ano lectivo. A minha forma de estar na Ciência será sempre condicionada pelo seu Exemplo.

Queria agradecer à Prof Maria José Calhorda, por toda a constante ajuda "nos bastidores", pelo seu contributo para a Química em Portugal e na Faculdade de Ciências.

Devo agradecer, também, às pessoas que contribuíram directamente para o conteúdo desta dissertação: Dr Liliana Ferreira, pelo seu contributo na caracterização magnética dos compostos, pela sua simpatia e pelos seus esclarecimentos das questões que sempre surgem de Física; Dr Nuno Bandeira, pela sua ajuda com os cálculos teóricos; Dr Ana Vicente, pela sua contribuição de AFM; Dr Ana Mourato, pelas análises de PXRD; Varun Kumar for his help with the Mössbauer measurements; Rafaela Marques pelo seu excelente trabalho com os compostos binucleares.

Uma palavra de apreço às pessoas que tornaram a minha estadia na FCUL mais agradável: os membros do QITP6, pela partilha de sucessos e infortúnios; os meus camaradas Filipe e Gonçalo, por todos os momentos bem passados.

I must thank COST Action ECOSTBio for the scientific opportunities I had throughout this year and to Prof Yann Garcia and his group members, who made sure my stay at Louvain-la-Neuve was pleasant and filled with Chemistry.

Por fim, tenho que agradecer aos meus pais e à minha namorada, Lígia Coelho, por todo o seu apoio.

Abstract

Spin crossover is a phenomenon, exhibited by transition metal complexes with appropriate spin pairing and ligand field energies, which shows great promise for the design of high-density information storage devices and molecular switches and sensors. The final application of the spin crossover device is determined by the spin transition profile. In the present work, several spin crossover candidate compounds with different nuclearities are presented. New materials were also fabricated based on a known spin crossover molecule.

In chapter 2.1, several Fe^{III} mononuclear related compounds, of the $[Fe(5\text{-}X\text{-}salEen)_2]Y$ type, were synthesised with varying halogens as substituents and most of these exhibited a gradual spin crossover, when studied by SQUID magnetometry. Different magnetic behaviour was observed for different solvates and compounds with a different ionic pair, as had been also noted in the literature. Density Functional Theory calculations suggested that the halogen electronic effect is not noticeable for the fluorine substituted compounds. The effect of ligand rigidity was also shown to affect the spin crossover phenomenon as one hexadentate compound was synthesised and exhibited no spin transition in the studied temperature range.

In chapter 2.2, binuclear compounds with hydrazide ligands of the $[Fe_2(L)_3]$ type, were also synthesised and studied by SQUID magnetometry. While none of the compounds exhibited any kind of spin transition, an antiferromagnetic coupling between both Fe^{III} centres was observed for all compounds and later confirmed with Density Functional Theory calculations.

Chapter 2.3 addresses an Fe^{II} cage that was designed and its synthesis attempted, however, the current available characterisation methods do not confirm the synthesis of the proposed cage. The isolated purple powder did not show spin crossover, but it exhibited different coupling effects between the Fe centres, depending on the temperature.

Chapter 2.4 contains the fabrication of materials from spin crossover complexes based on $[Fe(5\text{-}I\text{-}salEen)_2]ClO_4$. Nano-sized structures were synthesised, from a known spin crossover compound, in a PEG matrix. Their size was studied by both NANO-flex measurements and AFM imaging, however, the results were not in agreement, as the particles observed by AFM probably corresponded to aggregates and the particles were destroyed when the sample for the NANO-flex measurements was prepared, hence, one can only conclude they are indeed in the nano-scale. Magnetometry measurements of these particles showed a gradual spin crossover behaviour which is expected for this kind of structures. Although no magnetic behaviour was determined, a few nano-rods were synthesised from the same compound and observed by AFM imaging. In a different approach, gold nanoparticles were coated with a spin crossover candidate compound, as suggested by UV-Vis spectroscopy and AFM imaging, however it was not possible to determine the magnetic behaviour of the resulting particles.

Finally, in chapter 2.5, one can find a thermal analysis by Differential Scanning Calorimetry that was conducted on previously synthesised spin crossover compounds. Sharp peaks were observed at the same temperatures as the abrupt spin transitions, however, nothing is observed when the transition was gradual.

Keywords: Magnetic materials; Spin crossover; Nanoparticles; Transition metal complexes; Molecular cages.

Resumo

A transição de spin é um fenómeno que ocorre em complexos de metais de transição com energias de emparelhamento e de campo de ligandos apropriadas e com grande potencial para o desenvolvimento de aparelhos de armazenamento de informação de elevada densidade, sensores e interruptores moleculares. A aplicação final de cada aparelho é determinada pelo perfil da sua transição de spin sendo as transições de spin abruptas ideais para a fabricação de interruptores moleculares, as graduais preferíveis para o desenho de sensores e, por fim, as transições de spin com histerese são óptimas para o desenvolvimento de dispositivos de armazenamento de informação. Este fenómeno pode ser despoletado por variados estímulos externos tais como a variação de temperatura, pressão, luz ou aplicação de campo eléctrico ou magnético. Neste trabalho, vários compostos de ferro(III) e (II), candidatos a exibir o fenómeno da transição de spin, com diferentes nuclearidades, são apresentados. Foram também fabricados novos materiais a partir de uma molécula conhecida que exibe este fenómeno. O ferro foi seleccionado para a obtenção destes compostos devido à sua elevada abundância na Terra, o que permite uma exploração mais sustentável caso estes materiais sejam cruciais para a sociedade do futuro, assim como as características electrónicas que possui.

No capítulo 1, é feita uma introdução ao tema da transição de spin e é discutido o estado da arte para compostos com diferentes nuclearidades: mono-, bi- e multi-nucleares. A fabricação de materiais a partir destes compostos é também introduzida.

No capítulo 2.1, são apresentados os vários compostos de Fe^{III} mononucleares, do tipo $[Fe(5\text{-}X\text{-}salEen)_2]Y$, que foram sintetizados com diferentes halogéneos como substituintes nos anéis fenilo e a maior parte exibiu perfis de transição de spin graduais, quando estudados por magnetometria de SQUID. Foi também estudado o efeito da presença de solvente na rede cristalina e de diferentes aniões para a mesma estrutura catiónica contendo o ião metálico e verificou-se que estes efeitos afectam o comportamento magnético dos compostos, o que está de acordo com os resultados já reportados na literatura, incluindo o facto de o comportamento magnético dos cristais se modificar drasticamente após remoção do solvente incluído nas redes cristalinas. Foram também efectuados cálculos recorrendo à Teoria do Funcional de Densidade, que sugeriram que o efeito electrónico associado ao halogéneo não é relevante nos compostos com fluoreto, e que este efeito é superior à medida que o número de electrões do halogéneo aumenta. Verificou-se, também, que a rigidez dos ligandos é um factor que afecta a transição de spin. Com efeito, um composto com ligando hexadentado, análogo a outro previamente sintetizado com dois ligandos tridentados, foi sintetizado e não transitou de spin na gama de temperatura estudada, ao contrário do que foi observado para o composto com ligandos tridentados.

No capítulo 2.2, é apresentada a síntese de compostos binucleares de Fe^{III} e o seu estudo por magnetometria de SQUID. Estes compostos foram sintetizados com ligandos hidrazida novos, um simétrico e três assimétricos. Foi possível obter a estrutura de raios-X de cristal único apenas para o composto sintetizado com o ligando hidrazida simétrica. Apesar de nenhum transitar de spin, verificou-se um acoplamento antiferromagnético entre os centros metálicos de cada composto, efeito confirmado posteriormente por cálculos de Teoria do Funcional de Densidade. Estes cálculos permitiram, também, verificar que este acoplamento é significativamente superior nos compostos assimétricos, tal como esperado.

No capítulo 2.3, descreve-se a concepção de uma gaiola de Fe^{II} e a sua possível síntese, contudo, os métodos de caracterização disponíveis não permitiram confirmar a obtenção da gaiola proposta. O pó roxo obtido não demonstrou qualquer tipo de transição de spin, mas sim efeitos de acoplamento entre os centros metálicos dependentes da temperatura, já que se verificou um acoplamento ferromagnético na maior parte da gama de temperaturas estudada e um acoplamento antiferromagnético a baixas

temperaturas. Dever-se-á obter cristais deste composto num futuro próximo de forma a que se possam retirar melhores conclusões sobre as suas características e estrutura.

O capítulo 2.4 contém a obtenção de novos materiais a partir de moléculas conhecidas baseadas no composto $[Fe(5\text{-I-salEen})_2]ClO_4$, que exibem transição de spin. Para tal, estruturas à escala nanométrica foram sintetizadas numa matriz polimérica de PEG (polietilenoglicol). As suas dimensões foram estudadas através de medições NANO-flex e Microscopia de Força Atómica (AFM), no entanto, os resultados obtidos não foram concordantes, já que foram observados agregados através de AFM e as partículas se degradaram aquando da preparação das amostras para as medições NANO-flex, em clorofórmio. Assim, foi apenas possível determinar que as estruturas obtidas terão dimensões na escala nanométrica e têm uma morfologia aparentemente esférica, que será estudada com mais pormenor através de técnicas como a Microscopia Electrónica de Varrimento e Transmissão. A determinação do perfil magnético destas estruturas mostrou perfis de transição de spin graduais, tal como é esperado para este tipo de estruturas, no entanto, todas apresentaram um comportamento magnético semelhante ao exibido pelo cristal. Recorreu-se, também, à espectroscopia de UV-Visível que mostrou que as excitações electrónicas destes materiais são equivalentes às do respectivo cristal e a análise por Difracção de Raios-X de Pós mostrou um perfil típico de nano-estruturas. Apesar de o seu comportamento magnético não ter sido determinado, visto que seria necessária a técnica de espectroscopia de Raman que não está acessível ao nosso grupo de trabalho para já, foram também obtidos nano-varões, a partir do mesmo composto, que foram observados por AFM. Estes nano-varões foram sintetizados recorrendo a uma técnica diferente que consiste na aplicação de pressão, durante um intervalo de tempo considerável, a uma amostra de concentração reduzida depositada entre uma lâmina e uma lamela, ocorrendo a formação dos varões na superfície das lamelas. Numa abordagem diferente, nanopartículas de ouro foram cobertas com um composto candidato a exibir transição de spin, facto sugerido por medições de espectroscopia UV-Visível e AFM. Inicialmente sintetizou-se um composto derivatizado com grupos tiol e, de seguida, efectuou-se o acoplamento S-Au no interior de um reactor, a 323 K. É de notar que as nanopartículas de ouro, quando sujeitas ao mesmo tratamento mas sem a molécula tiolada no reactor, simplesmente agregaram e depositaram-se, facto que contribui para a suposição de que as partículas foram de facto cobertas pela molécula seleccionada. Não foi ainda possível a determinação do comportamento magnético das partículas resultantes.

Por fim, no capítulo 2.5, uma análise térmica recorrendo a Calorimetria Diferencial de Varrimento efectuada em compostos sintetizados anteriormente é descrita. É apresentado um estudo em duas moléculas semelhantes com substituintes de silício e a análise de outras duas moléculas. Foram observados picos bem definidos nas curvas obtidas com variações térmicas correspondentes às esperadas para transições de spin e a temperaturas concordantes com os perfis magnéticos traçados anteriormente. Foram observadas histereses nas transições de spin detectadas por Calorimetria Diferencial de Varrimento que não foram notadas através de magnetometria de SQUID. É de notar, também, que quando se observou uma pequena transição através de magnetometria, o pico correspondente na curva de Calorimetria que se obteve verificou-se consideravelmente inferior aos picos obtidos para transições abruptas consideráveis e nada se observa através de Calorimetria Diferencial de Varrimento quando a transição de spin no composto ocorre de forma gradual.

No capítulo 3, é apresentado um resumo das conclusões inferidas a partir de todo o trabalho.

No capítulo 4, são apresentados os detalhes experimentais relativos a todas as experiências da dissertação.

Este trabalho, que consistiu no estudo de diferentes abordagens para a obtenção de moléculas e materiais com o fenómeno de transição de spin permitiu a confirmação de alguma informação já extensamente reportada na literatura e suscitou questões relevantes para a comunidade científica da área, nomeadamente relativamente ao equilíbrio entre os factores electrónicos e estruturais neste tipo de compostos e o seu efeito final na concepção de dispositivos úteis para a sociedade do futuro. Sobretudo,

permitiu ao candidato a Mestre adquirir uma vasta formação em diferentes áreas da Química, experimental e teórica, principalmente no estudo da Spintrónica.

O conteúdo científico desta dissertação foi apresentado e discutido em vários encontros nacionais e internacionais. A lista detalhada encontra-se de seguida:

Apresentações orais:

The Effect of Halogen Substitution on the Properties of Iron(III) Spin Crossover Compounds, Institute of Condensed Matter and Nanosciences / Molecules, Solids and Reactivity (IMCN/MOST), Université Catholique de Louvain, Mar 8, 2018, Louvain-la-Neuve, Belgium.

Harnessing the Spin Crossover Phenomenon: A Study on the Anion and the Halogen Effects, 7th ECOSTBIO Scientific Workshop, Dec 14-15, 2017, Dublin, Ireland.

Póster:

Particle Size Effect on the Magnetic Behaviour of Fe(III) Schiff-base Complexes, 3rd meeting of Colégio de Química da Universidade de Lisboa, Chesmitry at ULisboa, Jun 27, 2018, Lisboa, Portugal.

No âmbito do trabalho, participei, também, na *2018 Summer School* do Colégio de Química da Universidade de Lisboa.

Palavras-chave: Materiais magnéticos; Transição de spin; Nanopartículas; Complexos de metais de transição; Gaiolas moleculares.

Contents

List of figures, schemes and tables

List of symbols and abbreviations

δ – Isomer shift
γ – Molar fraction
μ – Magnetic moment
χ_M – Molar magnetic susceptibility
ΔE_Q – Quadrupole splitting
Δ_{oct} – Delta octahedral
3D – Three dimensional
ACN – Acetonitrile
AFM – Atomic force microscopy
Ang – Angle
CFT – Crystal Field Theory
DFT – Density functional theory
DMF – Dimethylformamide
DMFT – Dynamic mean-field theory
DSC – Differential scanning calorimetry
EA – Elemental analysis
FTIR – Fourier-transform infrared
G – Gibbs energy
HS – High-spin
IUPAC – International Union for Pure and Applied Chemistry
J – Isotropic interaction parameter
k_B – Boltzmann constant
LFT – Ligand Field Theory
LIESST – Light-induced excited spin state trapping
LS – Low-spin
MeOH – Methanol
n – Number of unpaired electrons
NMR – Nuclear magnetic resonance
P – Spin pairing energy
PEG – Polyethylene glycol
PXRD – Powder X-ray diffraction
S – Total spin
SCO – Spin crossover
SCXRD – Single crystal X-ray diffraction
SEM – Scanning electron microscopy
SQUID – Superconducting quantum interference device
STM – Scanning Tunnelling Microscopy
T - Temperature
$T_{1/2}$ – Temperature at which half of the metal centres are in the low-spin state and half are in the high-spin state
TEM – Transmission electron microscopy

1 Introduction

1.1 Transition metal compounds

Transition elements are, according to the International Union of Pure and Applied Chemistry (IUPAC), the elements "whose atom has an incomplete *d* sub-shell, or which can give rise to cations with an incomplete *d* sub-shell"[1] and are found in the centre of the periodic table, in the *d*-block, along with those of group 12.

When in the presence of other ions or molecules, given the appropriate conditions, the transition elements are able to form bonds of mixed ionic and covalent nature with so-called ligands, thus resulting in transition metal complexes. Due to their incomplete *d* sub-shell, the valence molecular orbitals which arise upon the formation of these bonds are often populated with unpaired electrons, thus giving rise to paramagnetism. Usually, a change in colour is observed when the formation of transition metal complexes takes occurs.[2]

1.1.1 Electronic structure and bonding

The elements in the third period of the periodic table that belong to the *d*-block, often referred to as "first row transition metals", have particularly interesting properties due to their low ionisation energies,[3] which allow them to easily form cations with a wide range of oxidation states. The atoms with the widest array of possible oxidation states are found in the middle of this row (Cr, Mn, Fe and Co have 10, 11, 10 and 8 possible oxidation states in total – negative and positive - , respectively). Their electronic configuration is of the type [Ar]3d^n, with *n* depending on the oxidation state of the metal.

These cations may interact with other molecules in solution to form transition metal complexes. Even though they are positively charged, the nature of the bonding in the complexes that are thus formed cannot be thought of as ionic, because some ligands are neutral, in spite of their possible dipole. It is also not advisable to interpret the bonds as strictly covalent, since the metal ions have an electropositive nature that would not be rightfully taken into account in a purely covalent model. Thus, the most accurate way to describe the bonding in a transition metal complex is to consider mixed ionic and covalent nature, taking guidance from the electroneutrality principle of Linus Pauling.[4,5] This principle states that the charge on any single atom is within the range of ±1, resulting in a description of the bonds that is close to 50% ionic and 50% covalent, thus providing an approximate method of estimating charge distribution in complexes. The real proportion between the two bonding descriptions depends, mostly, on the nature of the ligands.

1.1.2 Crystal Field and Ligand Field theories

Now that bonding in transition metal complexes has been covered, one can wonder about how the ligands are arranged around the metal core. In order to tackle this concern, Kepert proposed a model,[2,6] based on the Valence Shell Electron Pair Repulsion theory,[7] in which the metal ion lies at the centre of a sphere and the ligands are considered to be point charges that are free to move over the surface of the said sphere, their location depending on steric and electronic – repulsive – effects. The repulsion caused by non-bonding electrons is ignored, here.

This model allows for the prediction of some of the geometries experimentally observed, however it is flawed in cases where the bulkiness of the ligand does not allow for the predicted arrangement – distorted geometries are often obtained – and where electronic effects drive the formation of completely different spatial arrangements.[2] One of the geometries predicted by Kepert is the octahedral geometry, which occurs for a coordination number – number of donor atoms, from the ligands, bound to the metal ion – of six and angles of 90º and will be the scope of most of this thesis.

According to the geometry of the complex and considering that *d*-orbitals have well defined spatial orientations, the interaction between the atomic orbitals of the ligands with those of metal can give rise to orbitals in different energy levels. One of the first theories to successfully explain these interactions was the Crystal Field Theory (CFT).[2] The CFT is a purely electrostatic model that suggests that the charges of the ligands create an electrostatic field around the metal centre. This approach is not in agreement with the actual bonding in most of these complexes, since no covalent interaction is taken into account and has a few repercussions. The *d*-orbitals of the metal must, thus, be split into different energy levels, depending on the relative alignment of the ligand point charges and the *d*-orbitals of the metal ion.

For the octahedral geometry, the expected splitting of the orbitals is observed in **Figure 1.1**. Note that if the mentioned electrostatic field was spherical, there would be no splitting of the orbitals. Instead, all five d-orbitals would increase in energy by the same amount.

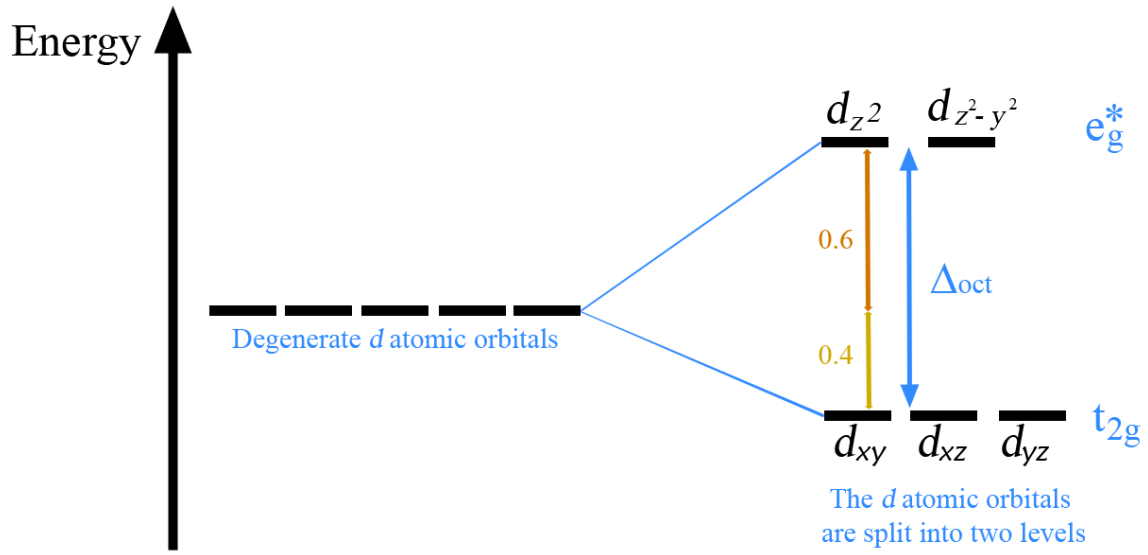

Figure 1.1 *d-orbital splitting for an octahedral transition metal complex, as predicted by the Crystal Field Theory.*

The splitting presented in **Figure 1.1** is predicted based on the relative orientations of the *d*-orbitals and the vertices of the octahedron, which are where the electrons of the donor atoms are located. The d_{z^2} and $d_{z^2-y^2}$ atomic orbitals point directly the vertices (**Figure 1.2**) and due to the electrostatic repulsion between the electrons that populate these orbitals and the electrons of the ligands, they are destabilized in regards to the average energy level for a spherical field, thus increasing in energy with the formation of the complex. On the other hand, the remaining *d* atomic orbitals (d_{xy} , d_{xz} and d_{yz}) are directed towards a point between the vertices of the octahedron (**Figure 1.2**), which undergoes less repulsion interaction and results in a stabilisation of these orbitals upon formation of an octahedral complex, relatively to the mean orbital energy value. The destabilisation of the formerly mentioned orbitals is of a greater extent than the stabilisation of the latter and the difference in energy between the two groups is referred to as delta octahedral (Δ_{oct}). This energy gap in transition metal compounds is of the utmost importance for many of their physical properties, like the ability to undergo spin crossover, which will be discussed later in this thesis.

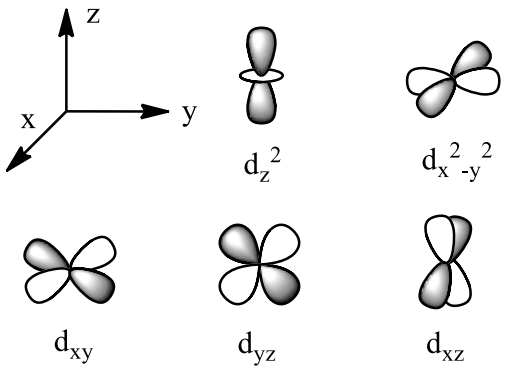

Figure 1.2 *Octahedral arrangement of d-orbitals.*

The magnitude of the Δ_{oct} is proportional to the strength of the electrostatic field created by the ligands and can be experimentally obtained by UV-visible spectroscopy,[2] for many complexes. It also depends on the nature and oxidation state of the metal.

Due to this splitting, and for transition metals between d^4 and d^7, electrons may populate the orbitals in different ways, resulting in two possible spin states. If Δ_{oct} is greater than the spin pairing energy (P),[8] the t_{2g} orbitals will be filled with most of the electrons and the complex will be in a low-spin (LS) state. If, however, P is greater than Δ_{oct}, the electrons will populate both t_{2g} and e_g^* groups of orbitals, following Hund's rule, thus resulting in a high-spin (HS) complex. This is only true for the 3*d* metals, as for the 4*d* and 5*d* metals the Δ_{oct} is of a much larger magnitude than the spin pairing energy.

$$\Delta_{oct} > P \rightarrow LS\ state \qquad (1.1)$$
$$\Delta_{oct} < P \rightarrow HS\ state \qquad (1.2)$$

The Ligand Field Theory (LFT)[9] was the most widely accepted theory in the 1970's for the description of transition metal complexes and it is based on the Crystal Field Theory. However, the most widely accepted theory today, which takes into account orbital mixing and σ and π covalent bonding, is the Molecular Orbital Theory.[10] The resulting bonding scheme in LFT is a mixed ionic and covalent approach, which is consistent with the previously mentioned electroneutrality principle of Pauling. Even though the LFT is the most consistent with experimental results, CFT will be the one used throughout this report, due to its simplicity and ability to describe most of the compounds presented.

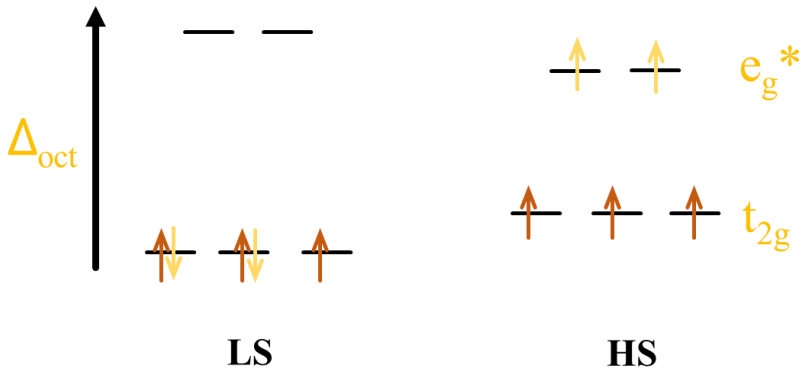

Figure 1.3 *The two possible spin states and respective electron distribution for an octahedral $3d^5$ metal ion.*

1.1.3 Magnetic properties of *d*-block compounds

As mentioned before, transition metal complexes have an incomplete valence sub-shell due to their unpaired *d*-electrons. The compounds are, therefore, called paramagnetic and exhibit a magnetic moment, which is related to the number of unpaired electrons, n, and total spin, S, through the following equation:[11]

$$\mu(spin-only) = \sqrt{n(n+2)} = \sqrt{4S(S+1)} \qquad (1.3)$$

Equation 1.3 is only considering the spin angular momentum of the electrons and not their orbital angular momentum (spin-orbit coupling effect). While most compounds can be described using the spin-only formula, spin-orbit coupling effects are particularly significant for complexes with t_{2g}^1, t_{2g}^2, $t_{2g}^4e_g^2$ and $t_{2g}^5e_g^2$ configurations and are more relevant at lower temperatures.

Even though the magnetic moment can be experimentally obtained through techniques such as superconducting quantum interference device (SQUID) magnetometry,[12] it is normally analysed in the form of molar magnetic susceptibility (χ_M) and the product of χ_M with temperature (T), if a temperature dependant measurement was conducted, is plotted. The effective magnetic moment (μ_{eff}) expressed in Bohr magnetons (μ_B = 9.27 x 10^{-24} J T^{-1}) and $\chi_M T$ are related through Equation 1.4. The 2.828 factor is derived from the full equation which contains the Boltzmann constant (k), the Avogadro number (L), temperature in Kelvin (T), and vacuum permeability (μ_0).[11]

$$\mu_{eff} = \sqrt{\frac{3k\chi_M T}{L\mu_0\mu_B^2}} = 2.828\sqrt{\chi_M T} \qquad (1.4)$$

When several paramagnetic centres interact with each another, cooperative phenomena such as ferromagnetic, antiferromagnetic[13] and ferrimagnetic interactions arise.[14] These depend on the relative alignment and position of the metal centres, however these will not be discussed in the present report, which will focus on regular paramagnetic compounds that follow the Curie-Weiss law.

1.2 Spin crossover

Spin crossover (SCO) is a phenomenon that octahedral compounds with a first row transition metal ion electronic configuration of d^4-d^7 exhibit when $P \cong \Delta_{oct}$.[15] P is roughly double the value for M^{3+} than it is for M^{2+} octahedral compounds, hence SCO is observed quite more often for M^{2+} complexes than M^{3+} complexes, as it is not as easy to synthesise ligands with suitable field.[8] Since the mentioned energies are very similar, a small stimulus is enough to trigger a transition from the LS state to the HS state and reverse. This phenomenon is in theory not possible for second and third row transition metal compounds, owing to their high nucleus density and charge which causes a major increase in Δ_{oct} and the resulting complexes are always found in the LS state, following Equation 1.1.

Several types of spin crossover profiles have been observed ranging from gradual (**Figure 1.4** a)), typical of SCO in solution since no cooperativity between the metal centres is expectable, to abrupt with hysteresis (**Figure 1.4** c)), which is usually observed in SCO solids with a high degree of cooperativity. The possible SCO profiles are shown in **Figure 1.4**.

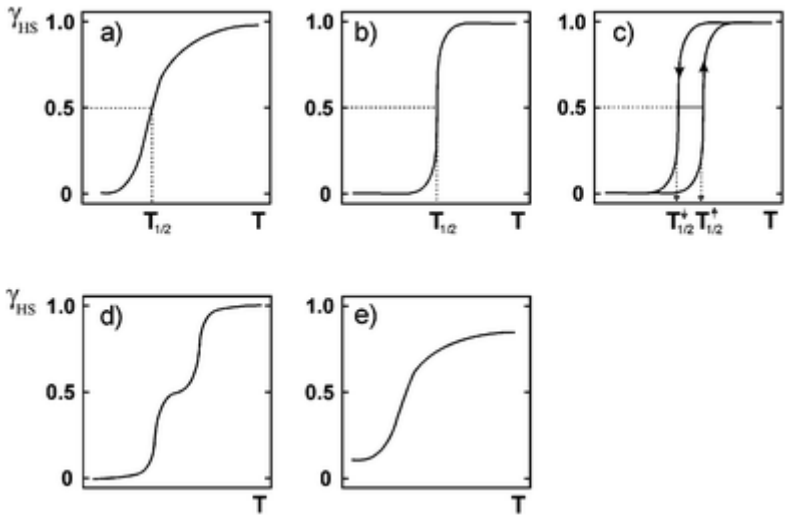

Figure 1.4 *Possible SCO profiles plotted in molar fraction of HS cores (γHS) vs temperature: a) Gradual transition; b) abrupt transition; c) abrupt with hysteresis transition; d) stepped transition; e) incomplete transition. Reproduced from elsewhere.*[16]

Even though the first evidence of the SCO phenomenon was reported for an Fe^{III} compound,[17] most SCO compounds that were discovered since were with Fe^{II} and Co^{II} cations.[18,19] There are only a few examples of SCO in Fe^{III} and Mn^{III} compounds.

The SCO phenomenon is accompanied not only by the electronic rearrangement, but also by a structural rearrangement, due to the longer distances between the metal core and the ligand donor atom in the HS state. This allows for the detection of SCO with several different techniques that either measure electron distribution-related phenomena (optical properties, vibrational properties, magnetic properties) or that measure structural properties. Thermochromism is also observed for many SCO compounds, thus making possible the detection of the phenomenon with the naked eye and through UV-vis spectroscopy, when the *d-d* transition bands are not concealed within bands from other electronic phenomena.

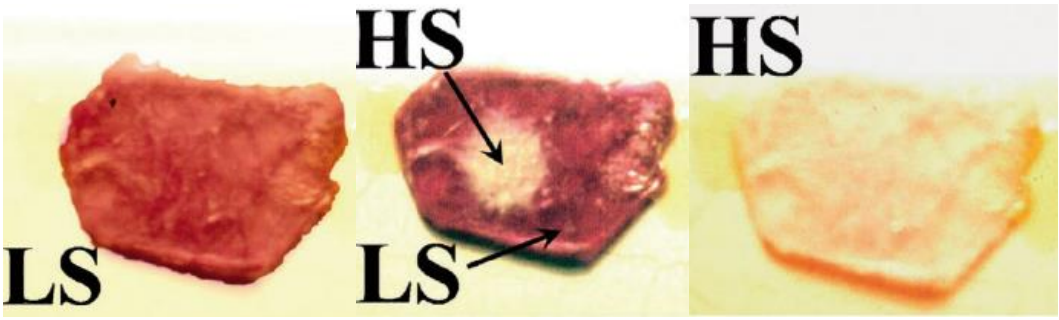

Figure 1.5 *Thermochromism observed for crystals of $[Fe(ptz)_6](BF_4)_2$ (ptz = 1-propyltetrazole). Adapted from elsewhere.*[20]

1.2.1 Mechanisms of SCO

The most common mechanism of triggering SCO is temperature variation.[21–24] Temperature triggering is possible when the difference in Gibbs energy between both spin states is roughly equal to the product of the temperature and the Boltzmann constant (k_B), following Equation 1.5.

$$\Delta G_{HS-LS} \approx k_B T \qquad (1.5)$$

One can note that Equation 1.5 is valid for any compound, but the temperature value calculated for compounds that do not exhibit this phenomenon is not reasonable. The temperature dependant

measurements are usually conducted on a SQUID magnetometer which measures magnetic moment as arbitrary units. The molar fraction of metal cores in each spin state, at a given temperature T, can be calculated using Equation 1.6.[20]

$$\chi(T) = \gamma_{HS}(T) \cdot \chi_{HS} + \big(1 - \gamma_{LS}(T)\big) \cdot \chi_{LS} \qquad (1.6)$$

Mössbauer spectroscopy can also be used to detect thermal-activated spin crossover.[25] For Fe, the isotope used for this purpose is ^{57}Fe, which allows for the identification of both the oxidation and spin state of iron ions in the sample. The two Mössbauer parameters which are relevant for this determination are the isomer shift (δ, **Figure 1.6**) and the quadrupole splitting (ΔE_Q). It is possible to calculate the fraction of iron ions in each spin state from the relative areas of the respective resonance peaks.

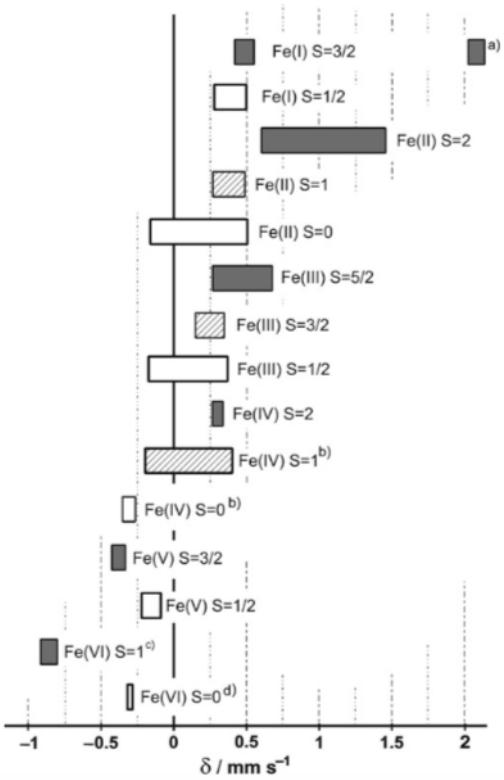

Figure 1.6 *Ranges of isomer shift values obtained for iron compounds in ^{57}Fe Mössbauer measurements, at room temperature. Reproduced from elsewhere.*[25]

Pressure can also be used to trigger SCO.[26] The decrease in bond distances caused by the application of considerably high pressure increases the ligand field strength, thus favouring the LS state. When the previously mentioned temperature dependant measurements are conducted while applying pressure, there is an increase in $T_{1/2}$, expected from the LS state stabilisation.[20]

At lower temperatures, light (specifically green light) has been shown to trigger the SCO phenomenon.[27–29] The irradiation of a solid compound at low temperatures – usually in the LS state – can excite a fraction of LS centres to a metastable HS state with a lifetime of several days under temperatures of 20 K but quickly decays at room temperature. This specific phenomenon is called Light-Induced Excited Spin State Trapping (LIESST).[30] The reverse conversion, from the HS state to the LS state, is performed with red light irradiation. To date, the relaxation temperature obtained for the LIESST effect that was closest to room temperature was 130 K, found in an Fe^{II} compound.[31]

Finally, electric current has also been able to trigger SCO and is one of the most promising stimulus for the development of devices. However, not many cases have been studied so far, mainly due to the insulating nature of most of these compounds. Only in 2009 was it found that a previously investigated SCO compound, $[Fe(HB(pz)_3)_2]$, exhibited electrical conductivity values consistent with the fabrication of devices.[32] Temperature dependant conductivity measurements have shown an increase of one order of magnitude from one spin state to the other. Hybrid materials combining spin crossover entities and conducting entities had already been though of and will be covered in chapter 1.3.

Calorimetry techniques are very useful to determine the order of transition and the cooperative interactions in a SCO solid, from the calculation of the ΔH and ΔS values. It is also possible to accurately determine $T_{1/2}$ from calorimetry measurements.

The structure changes that occur during a spin transition make it detectable by diffraction methods as well. Displacive transitions can be immediately identified from the rapid extension of the metal-ligand bonds in a LS-HS transition. Reconstructive transitions, on the other hand, are usually accompanied by a space group change, which also makes them detectable by the same methods. Hence, Single Crystal X-Ray (SCXRD) and Powder X-Ray Diffraction (PXRD) techniques are very useful for the classification of the spin transition, since they allow for the detailed examination of the variations on the cell parameters and crystal structure derived from the spin transition, especially when the measurements are performed close to $T_{1/2}$. SCXRD also provides information about the extended cooperative interactions in the crystal lattice, which have been proven to assist the SCO phenomenon.

Although less common, it is also possible to find SCO through vibrational spectroscopy in the far infra-red region, due to the different intensities for the stretching of the metal-ligand bonds in each spin state.

Phase transitions can be made to accompany spin transitions,[33,34] which allows for the detection of this phenomenon through techniques such as Differential Scanning Calorimetry (DSC). This kind of thermal-related events has been shown to induce interesting properties as *Martinho et al.* have reported the first observations of the thermosalient effect, which consists on a jumping or explosive motion of crystals upon a temperature variation that may be positive or negative,[35] for SCO compounds.[36]

1.2.2 Factors that affect SCO

Ligand modification is probably the most important factor that affects the SCO behaviour of a compound, since small changes in the molecules have been shown to deeply affect the magnetic behaviour of a given complex. The most common derivations noted in the literature are the substitution of hydrogens in the aromatic rings of the ligands for halogens, alkyl chains or alcohol derivatives, with varying carbon chain lengths. Halogen substitution (from fluoride to iodine) has been shown to generally increase $T_{1/2}$, in the cases where the packing of the molecules is the same.[37,38] Otherwise, the intermolecular interactions observed in the crystals are different and the magnetic profiles are, thus, not comparable.[39] The increase in size of alkyl chains present in the ligands leads to the development of strong van der Waals interactions between molecules, hence many variations to the magnetic behaviour of the compounds may be observed.[40,41]

Metal dilution has also been noted to affect spin crossover.[42] Since SCO is a phenomenon which depends on the cooperativity of metal centres, the substitution of SCO metal centres for non-SCO metal centres decreases the cooperativity in the crystal lattice and eventually transforms abrupt transitions into gradual ones. This will be discussed in further detail in the next chapter.

Different surfaces are known to affect the packing of SCO molecules, thus several polymorphs may be obtained with opposite SCO profiles.[43]

The magnetic profile of a crystal is also different according to the anion that is used in its synthesis.[44] Anions can either promote cooperativity through interactions such as hydrogen bonds,

halogen bonds or π-π interactions with the cation or supress cooperativity by increasing the distance between metal centres.

Polymorphism has been observed in many SCO solids and has been previously discussed in the literature.[45] It may be either solvent induced,[46] depending on the crystallisation method[47] or crystallisation conditions.[48] Magnetic profiles of the whole spectrum of possibilities have been obtained for polymorphs of the same compound.

Lastly, the presence of solvent in the crystal lattice also affects the SCO behaviour of a crystal and has been extensively studied.[46,49,50] This effect is very similar to the anion effect. It may either increase or decrease cooperativity between metal centres and varies according to the number of solvent molecules in the lattice.

1.2.3 Cooperativity between spin crossover entities

Aside from the observation that spin crossover in solution – when molecules are well separated and non-interacting – is always a gradual phenomenon and in the solid state abruptness is also found, there is experimental evidence for the cooperativity between metal centres in abrupt spin transitions. In 1976, for instance, a Mössbauer study was performed on ethanol solvated $[Fe_xZn_{1-x}(2\text{-pic})_3]Ch_2$ type crystals[42] in order to determine the effect of iron dilution on the transition in the SCO behaviour of the compounds. Results showed that the decrease in iron concentration transformed a rather abrupt transition into gradual with a decrease in $T_{1/2}$, thus proving that direct cooperative interactions between the metal centres that are able to undergo a spin transition is essential. The cooperativity can be achieved through covalent bridging of the metal centres or through intermolecular interactions.[51]

From these observations, Sorai proposed a model in which several domains with equal number of metal centres are formed during a phase transition.[52] These domains are randomly located in the crystal lattice (**Figure 1.7**) and the value which is often referred as $T_{1/2}$ is the temperature at which the number of domains in the LS and HS state is equivalent.

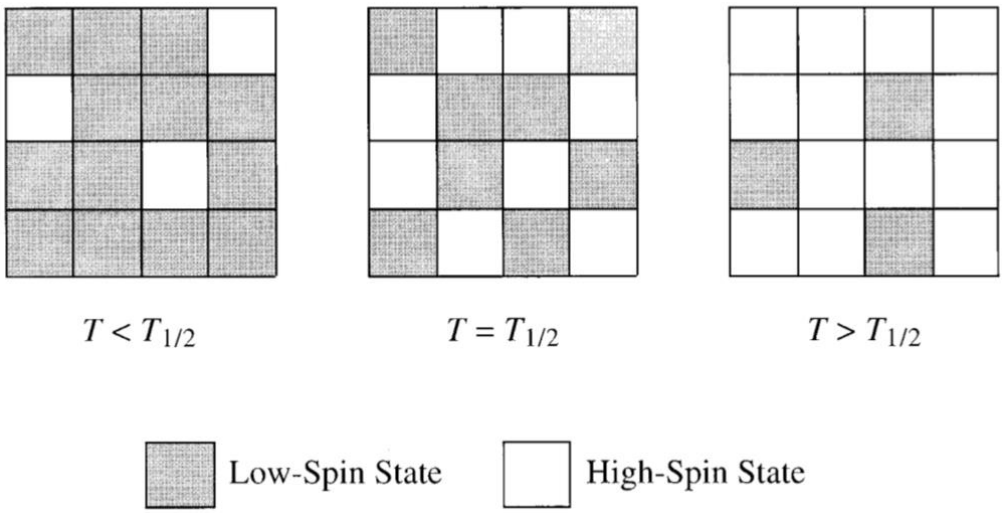

Figure 1.7 *Domain model in cooperative SCO systems proposed by Sorai. Reproduced from elsewhere.*[52]

Even though it has been possible to predict spin transition temperatures in solution,[53] it is very computationally demanding to make theoretical calculations for solids, and it is not yet possible to predict the packing of molecules in the solid state. Yet, there have been some attempts to use theory in order to rationalise systems with extended cooperative networks.

Initially, theoreticians resorted to Density Functional Theory[54] (DFT) owing to its widespread availability and low computational cost.[55] Once the packing of the molecules is known, it is possible

to define a periodic boundary consisting of a repetitive unit in the studied system – usually the unit cell of the crystal – and calculate the properties of a quasi-infinite system with DFT.[56] However, this approach falls short in several ways. The SCO behaviour of a solid depends not only on core interactions, but also on surface interactions,[57] and the latter are not described by periodic boundary conditions. Also, pure DFT methods treat electron densities only and cannot calculate electron-phonon coupling. Even if dispersion correction functions[58] are included to calculate the intermolecular interactions which often contribute to the propagation of the spin crossover phenomenon through the solid materials, the results are not too accurate.

The dynamical mean-field theory (DMFT)[59] was proposed in order to further elucidate these solid state phenomena by modifying the Kohn-Sham wave functions into many-body wavefunctions that allow for the hopping of electrons between metal cores, in the case of spin crossover.

One of the most recent and perhaps successful attempts to describe SCO solids was the design of a hybrid theoretical model, through the combination of DFT and DMFT, DFT+DMFT.[60] This model allows the calculation of electronic, magnetic and structural properties of some correlated systems, including phase transitions which are of the utmost importance for spin crossover solids.

1.2.4 Mononuclear compounds

Mononuclear SCO compounds have been obtained with ligands with various chelating properties. These ligands are usually subdivided in categories according to the donor atoms in the coordination sphere. Most SCO mononuclear compounds were obtained with ligands of the N_6,[61] N_4O_2[62] or N_4S_2[63] type, if we consider octahedral compounds.

Many Fe^{II} compounds with interesting properties were synthesised using two bidentate phenantroline or bipyridyl type ligands and two monodentate thiocyanate ligands. These are useful, since the resulting compounds have a N_6 coordination sphere, which is favourable for the occurrence of SCO, and the molecules can be coupled to gold surfaces or electrodes through covalent bonding of the sulphur atom present in the thiocyanate ligands.

The N_4O_2 compounds are usually obtained with Schiff-base ligands. These are synthesised from a condensation between an amine and an aldehyde and their use in SCO has been extensively studied.[36,64] They are often found as bidentate or tridentate ligands and yield neutral compounds with Fe^{II} or cationic Fe^{III} compounds, thus a negatively charged counter ion is often needed for crystallisation. These may range from the tetrahedral perchlorate to the octahedral hexafluorophosphates, however one must keep in mind that the size of the counter ion will surely influence the crystal packing of the resulting compound and, finally, its magnetic properties.

Some $N_2O_2S_2$ (such as the H_2thsa-R family)[65] compounds have also been obtained, and the first report of the SCO phenomenon was actually on S_6 compounds,[17] although they are not as common.

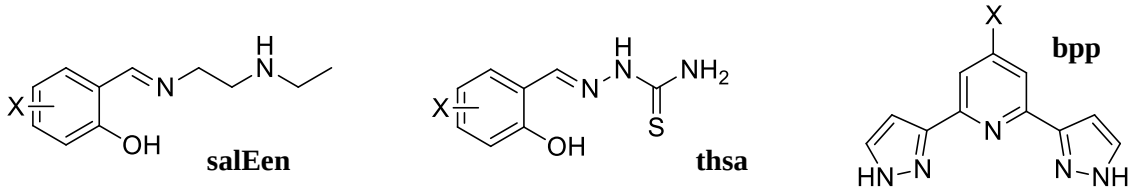

Figure 1.8 *Some of the ligands commonly used in SCO research.*

1.2.5 Spin crossover polymers and clusters

Several different types of multinuclear SCO compounds have been designed throughout the years, ranging from simple dimers to complex three dimensional (3D) structures. These structures would allow for the design of only mid-tier SCO materials, since the possible information density achieved is not the maximum, because the magnetic phenomena observed do not depend on a single molecule only.

Linear and two dimensional SCO polymers have been obtained with rather wide thermal hysteresis. Hysteresis of roughly 30 K was observed for the $[Fe(Htrz)_2(trz)]BF_4$ (Htrz = 1,2,4-triazole)

linear coordination polymer[66] and of 20 K for the two dimensional array of $[Fe(btrz)_2(NCS)_2]\cdot H_2O$ btrz = 4,4'-bis-1,2,4-triazole) molecules.[67]

Since then, many 3D SCO structures were synthesised, mainly with pyridine and pyrimidine derivatives as ligands or linkers, as well as Hofmann-like structures with two different metal sites, one with paramagnetic properties and the other with diamagnetic properties. These materials exhibit porosity, thus they are capable to incorporate guest molecules, such as solvent or small organic molecules, and these may affect their magnetic properties.[68–70]

Stepped SCO profiles are also often obtained in SCO polymers, due to the large amount of metal centres which may have different environments.[71] Some SCO clusters have also been synthesised displaying different types of magnetic profiles[72,73] and transitions in clusters were recently overviewed with theoretical calculations,[74] however these have not sparked much interest in the SCO community.

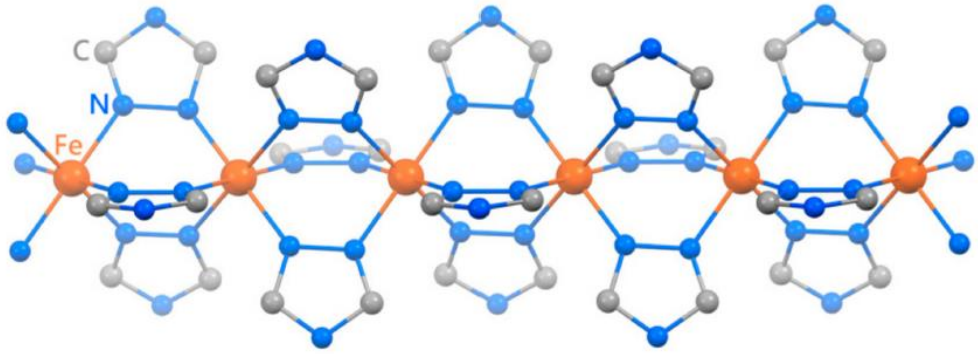

Figure 1.9 *Molecular structure of the SCO polymer which has been most explored, [Fe(II)(R-trz)$_3$]. Hydrogen and substituent atoms omitted for clarity. Adapted from elsewhere.*[75]

1.3 Spin crossover materials

The demand for higher density information storage and miniaturisation of many devices pushed chemists to design materials as close to the final application as possible based on spin crossover molecules. This included the coupling of the spin crossover phenomenon with other physical phenomena, such as conductivity, luminescence and charge/electron transfer.

1.3.1 Micro and Nanoparticles

One of the first efforts in that regard was to study how the decrease in particle size would affect the different magnetic profiles observed for macroscopic entities. Hence, nanoparticles were prepared with SCO coordination polymers, mostly through the reverse micelle technique. In this technique, micelles containing the ligand and the metal salt are prepared in separate vessels with a surfactant and these are mixed in order to synthesise the SCO nanoparticles in their interior. The resulting SCO polymers, obtained after precipitation, exhibit a decrease in the cooperativity between mental centres, which is observed from lower $T_{1/2}$ values and more gradual profiles when compared to the respective bulk material.

Ruben et al. developed interesting work on the coupling of SCO molecules to gold nanoparticles.[76] Molecules with Fe^{II} SCO centres and thioacetate terminal groups were synthesised and formerly coupled with gold nanoparticles. The resulting Nano-sized bodies were then assembled in arrays in three substrates. While the SCO molecules exhibited a rather abrupt and complete SCO profile with a small thermal hysteresis, the gold arrays only exhibited partial spin transition with two different resistance minima between 260 and 290 K.

Nanostructures have also been designed using single SCO complexes. These include nanowires and nanojunctions.

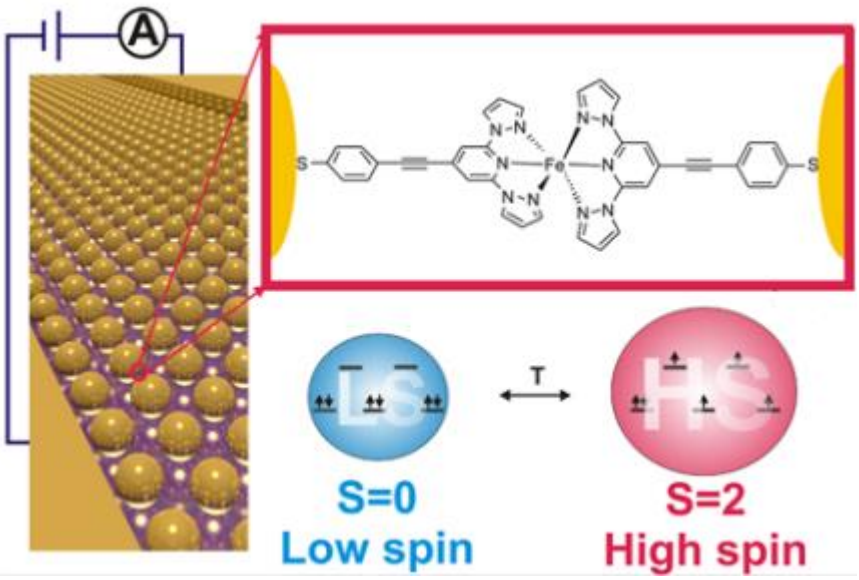

Figure 1.10 *Arrays of gold nanoparticles modified with a SCO molecule, as synthesized by Ruben et al. Adapted from elsewhere.*[76]

1.3.2 Hybrid spin crossover materials

Spin crossover centres can be coupled with luminophores in order to either probe the spin state of the metal through quenching of the luminescence phenomenon or induce the SCO by light absorption. With this goal in mind, two types of systems were designed for mononuclear compounds: donor-acceptor and donor-bridge-acceptor (with the bridges being alkyl chain) systems. In the former, the acceptor can be either the ligand itself (if the ligand is a luminophore) or a luminescent derivatisation can be performed on a typical ligand used in SCO compounds.

Some research has also gone into the grafting of SCO molecules into surfaces such as graphene[77] or Au(111), due to their high conductivity and possibility to excite the SCO entities through electric current. Not long ago, Ossinger *et al.* published a study[78] in which a molecule, $[Fe(H_2B(pz)_2)_2(phenme_4)]$ (pz = pyrazole, $phenme_4$ = 3,4,7,8-tetramethyl-1,10-phenantroline), with a gradual temperature-dependant SCO profile in the bulk was deposited by vapour deposition into Bi(111) and Au(111) surfaces. While in the former the SCO phenomenon was still observed, even though in a lesser extent (only approximately 50% of the iron cores switched), in the latter the molecule dissociated when deposited on the gold surface, hence no magnetic profile was obtained and a comparison between both surfaces was not possible.

van der Zant et al. managed to deposit hybrid SCO and SiO_2 nanoparticles into graphene electrodes through dielectrophoresis.[79] *Conductance vs Temperature* measurements showed a hysteresis between roughly 340 and 360 K for various samples, thus proving their attempt at successfully designing an electric bistable system. In a very recent similar attempt, *Ruben et al.* decorated graphene sheets with Fe^{II} SCO complexes containing bulky anchoring groups.[80] In this case, the final hybrid materials were obtained in the form of dark powders and their magnetic profiles exhibited gradual spin crossover behaviours (**Figure 1.11**) with higher $T_{1/2}$, in contrast to the abrupt transition observed for the bulk Fe^{II} complex.

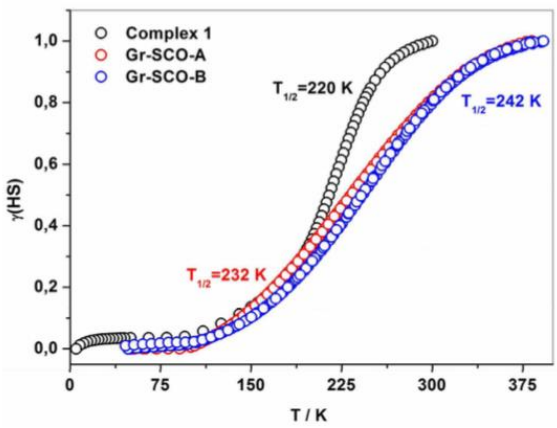

Figure 1.11 *Molar fraction of HS metal cores vs Temperature for a bulk crystal of the compounds obtained by Kumar et al. and the respective graphene sheet hybrid materials. Reproduced from elsewhere.*[80]

Room temperature conductance switching phenomena have also been found for SCO devices assembled in gold surfaces.[81] *Diéz-Pérez et al.* studied the interaction of an Fe^{II} paramagnetic compound with the gold atoms in a surface through Scanning Tunnelling Microscopy (STM). The modified surface was obtained from covalent binding to one of the thiocyanate ligands in the SCO molecule. The remaining thiocyanate was excited with a nickel STM tip, in order to probe the surface for conductance properties and the switching phenomenon was found at different temperatures. In a close approach, *Richard et al.* deposited an Fe^{III} charged SCO complex, $[Fe(pap)_2]^+$ (pap = N-2-pyridylmethylidene-2-hydroxyphenylaminato) onto an ordered gold surface, through sublimation.[82] The molecules were then excited by application of voltage pulses up to -3 V using an STM tip, in order to provoke a switching of their spin state. The authors noted that, although spin state switching was observed in two attempts, most of the energy transferred from the STM tip pulses to the cations resulted in a displacement or rotation of the molecule.

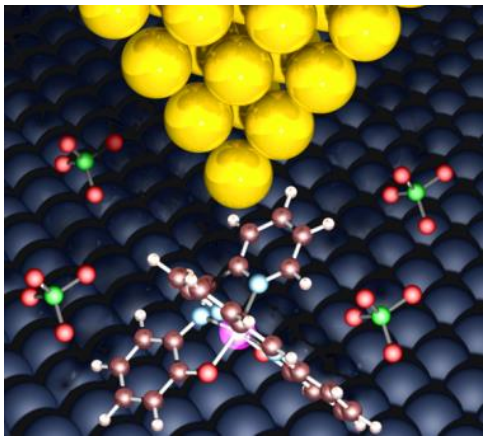

Figure 1.12 *Model of the excitation of a molecule by a STM tip. Black spheres represent the surface where the molecule is bound. Reproduced from elsewhere.*[82]

1.4 Iron

1.4.1 The element

Iron is the most abundant transition element on earth[83] and is easily recycled, thus making it the ideal candidate for materials of the future. It is found everywhere, from the molten core of our planet

to the building blocks of life-essential molecules in our body, such as the heme group.[84] It is the main component in several alloys important for materials in everyday life.

Usually it is obtained, as raw material, from the reduction of the iron oxides present in common ores, such as the hematite (Fe_2O_3), magnetite (Fe_3O_4), and limonite (FeOOH).[83]

1.4.2 Iron as a spin crossover backbone

The two iron ions reported with spin crossover capabilities are Fe^{II}, with electron populations in octahedral compounds of $t_{2g}^6e_g^0$ (S=0) and $t_{2g}^4e_g^2$ (S=2) for the LS and HS states[85] respectively and Fe^{III}, which may be populated as $t_{2g}^5e_g^0$ (S=1/2) if found in the LS state or $t_{2g}^3e_g^2$ (S=5/2) if found in the HS state.[86] Fe^{II} not only has the largest library of SCO compounds, but its spin transition has the interesting feature of switching between diamagnetic (LS) and paramagnetic (HS) states.

For these special characteristics, an obvious choice for the design of SCO molecules and materials is to use transition metal complexes built with iron units.

2 Results and discussion

2.1 Mononuclear compounds

The compounds in section 2.1 were synthesised and fully characterised by me. Dr Liliana P. Ferreira was responsible for the collection of the SQUID raw data. The Mössbauer data was collected and treated by me at IMCN/MOST during a STSM supported by the CM1305 (ECOSTBio) COST Action.

The simplest magnetic entity one can synthesise with transition metal complexes is the mononuclear compound. Thus, the initial efforts of the present thesis were directed towards the synthesis of mononuclear Fe^{III} spin crossover compounds.

A series of halogen-substituted Schiff-base tridentate ligands were synthesised to that effect, through condensation reactions with the general mechanism described below (**Scheme 2.1**).

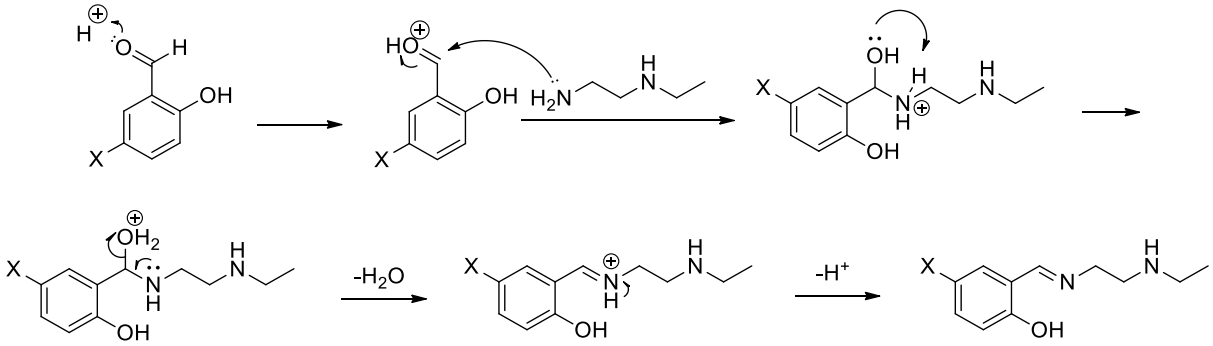

Scheme 2.1 *Reaction mechanism for the synthesis of the tridentate ligands (X=F, Cl, I).*

The desired aldehyde (5-X-salicylaldehyde; X=F, Cl, I) is dissolved in a protic solvent (usually methanol; in the case of non-protic solvents, a catalytic amount of hydrochloric acid is added), *N*-ethyl-ethylenediamine is added in stoichiometric amounts and the mixture is stirred for about 30 minutes at room-temperature. A change in colour is observed from colourless to yellow, confirming the imine formation. This reaction mixture is then used for coordination with a metal ion and this procedure is discussed below. The reaction for the synthesis of the hexadentate Schiff-base ligands follows the same reaction mechanism and is depicted in **Scheme 2.2**.

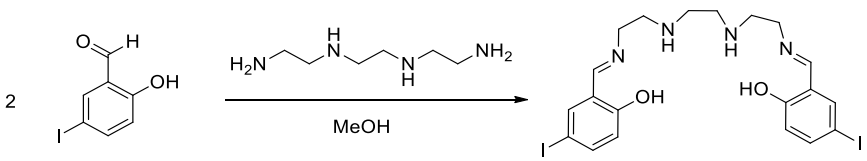

Scheme 2.2 *Synthesis of the hexadentate ligand.*

In a separate beaker, the appropriate Fe^{II} salt is dissolved in methanol and filtered into the beaker containing the Schiff-base solution. Immediately, the metal is oxidised to Fe^{III} by atmospheric oxygen and the final complex is formed with a change in colour from yellow to black. Black crystals are obtained in reasonably good yields (30-40%) by slow evaporation of the solvent at atmospheric pressure and room-temperature.

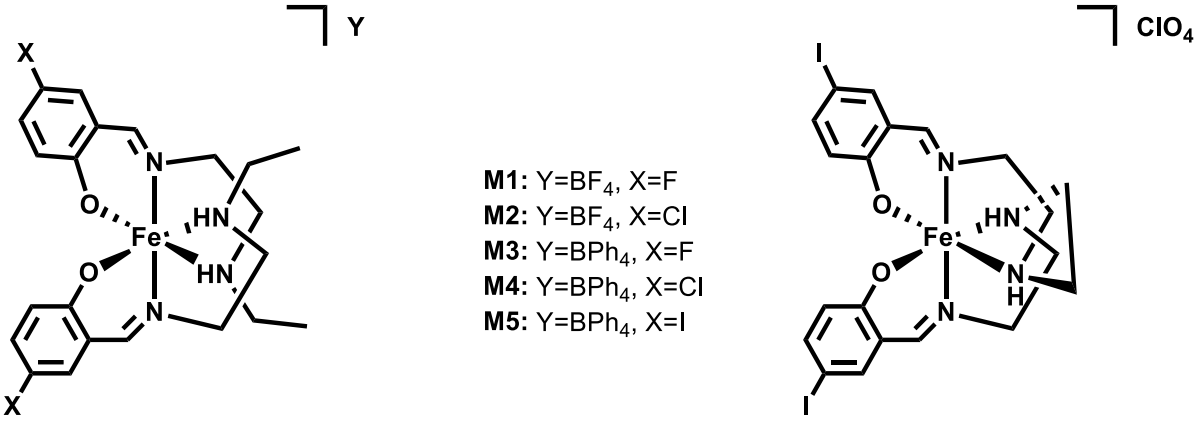

Scheme 2.3 *Complexes with tridentate ligands (left) and with the hexadentate ligand (right).*

2.1.1 Tetrafluoroborate complexes

The crystals obtained from the tridentate ligands, iron(II) chloride and sodium tetrafluoroborate were characterised by Fourier-Transform Infrared (FTIR) spectroscopy, Superconducting Quantum Interference Device (SQUID) magnetometry, Elemental Analysis (EA) and Mössbauer spectroscopy.

FTIR spectroscopy was mainly used to confirm the imine formation through the observation of a strong stretching vibration with a wavenumber close to 1600 cm^{-1} and the presence of the tetrafluoroborate anion through the observation of its characteristic vibrational modes (1070, 1460 cm^{-1}). The FTIR spectrum of the compound **M1** can be observed in **Figure 2.1**.

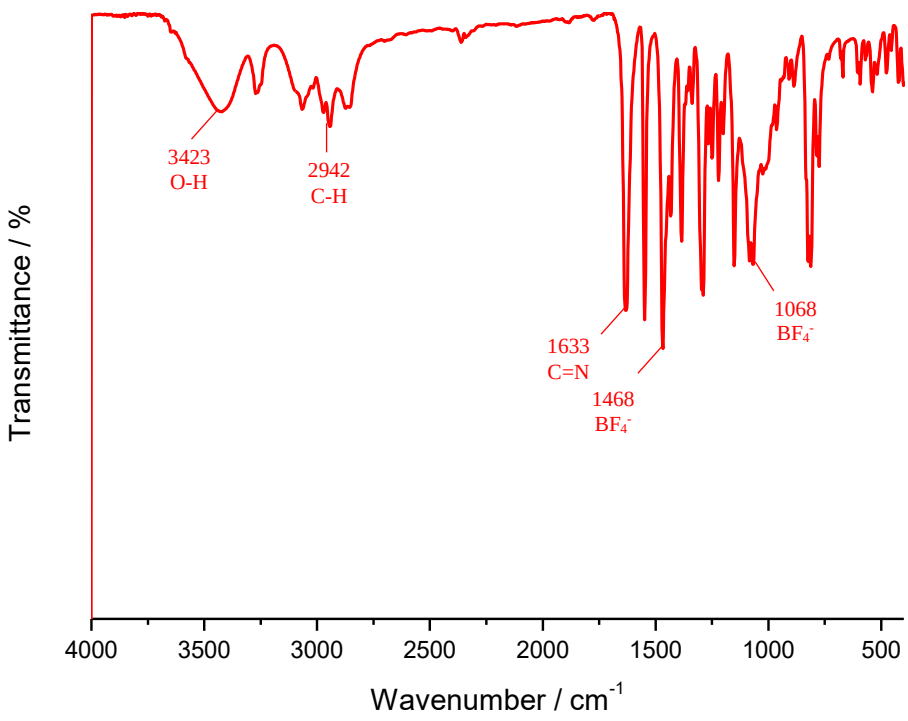

Figure 2.1 *FTIR spectrum of **M1**. The spectrum for **M2** can be found in the SI.*

As expected, one can note the strong vibration of the C=N bond at 1633 cm^{-1} and the patterns typical for the tetrafluoroborate anion with peaks at 1468 and 1068 cm^{-1}, thus indicating that the obtained crystals were constituted by the desired ionic pair. The chlorine (**M2**) substituted compound yielded an analogous FTIR spectrum (**Figure 6.1**).

2.1.1.1 Magnetic characterisation

The SQUID magnetometry plot for both compounds can be observed in **Figure 2.2**. These measurements were conducted on polycrystalline samples with three alternating cooling/warming runs at a rate of 5 K min^{-1}.

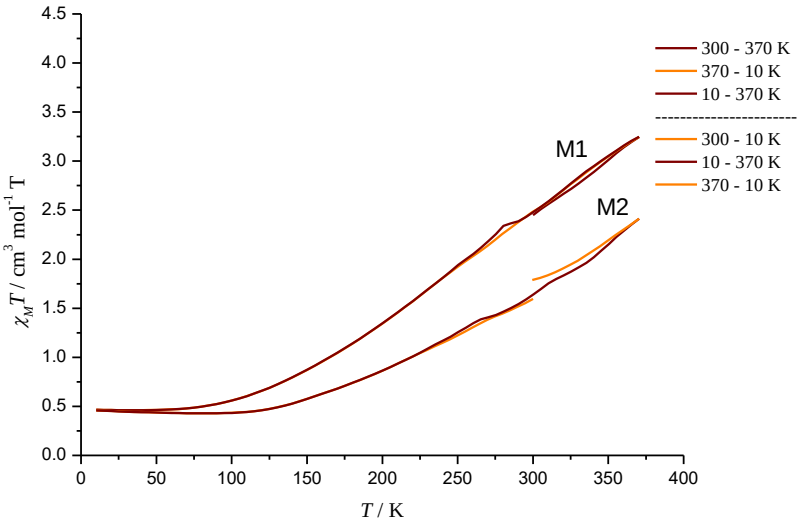

Figure 2.2 *$\chi_M T$ vs T plots for both F substituted (**M1**) and Cl substituted (**M2**) BF_4 compounds.*

The results are presented as plots of the product of molar susceptibility and temperature, in function of temperature. The theoretical value for Fe^{III} in each of the spin states is, approximately, $\chi_M T_{(LS)} = 0.37$ and $\chi_M T_{(HS)} = 4.38$.

In the case of **M1**, the measurement starts at 300 K with a $\chi_M T$ value of 2.45 cm^3 mol^{-1} K, which corresponds to, approximately (spin-only formula: $\% HS = \frac{\chi_{M(sample)} - \chi_{M(LS)}}{\chi_{M(HS)} - \chi_{M(LS)}} \times 100$), 52% of the Fe^{III} ions in the high-spin state. The sample is subsequently heated up to 370 K, displaying a $\chi_M T$ value of 3.24 cm^3 mol^{-1} K – 72% of the Fe centres are found in the high-spin state. Finally, the sample was cooled to 10 K at which temperature exhibited a $\chi_M T$ value of 0.47 cm^3 mol^{-1} K, typical for low-spin Fe^{III} complexes. The heating curve does not match the cooling curve just below room temperature, giving rise to a very small hysteresis. Hence, compound **M1** displays a gradual spin crossover profile.

In the case of **M2**, the measurement started at 300 K with a $\chi_M T$ value of 1.59 cm^3 mol^{-1} K, corresponding to a population of 30% of the Fe^{III} centres in the high-spin state. The sample was, then, cooled down to 10 K and a $\chi_M T$ value of 0.46 cm^3 mol^{-1} K was obtained, again, typical of low-spin Fe^{III} compounds. Then, the sample was warmed to 370 K, showing a $\chi_M T$ value of 2.41 cm^3 mol^{-1} K. Lastly, the compound was cooled to 300 K, essentially matching the previously obtained results for the same temperature range. Thus, compound **M2** also exhibits a gradual spin crossover profile, but with a smaller slope than **M1**, resulting in a higher apparent $T_{1/2}$, which is in agreement with previous findings that stated that an increase in halogen size should result in an increase in $T_{1/2}$,[87] although this is not the case for every series of compounds.

2.1.1.2 DFT calculations

DFT calculations (ADF, B3LYP*/TZP fc) were employed in order to understand the magnetic behaviour of these compounds in further detail. Geometry optimisations were carried out for the S=1/2 and S=5/2 spin states, their energies calculated, and the results are presented in **Table 2.1**.

Table 2.1 *Energy difference (kcal mol^{-1}) between the high-spin and low-spin DFT optimised structures for the BF_4^- series of compounds.*

Compound	ΔE_{HS-LS}
[Fe(5-F-salEen)$_2$]BF_4 (**M1**)	0.75
[Fe(5-Cl-salEen)$_2$]BF_4 (**M2**)	0.44
[Fe(5-I-salEen)$_2$]BF_4 (**M6**)	0.45

The ΔE value for **M2** is lower than the one for **M1**. This should indicate a spin transition at a lower temperature, since lower energy is required for the spin state switching, however, the opposite is observed in the magnetic profiles. These results suggest that the increase in $T_{1/2}$ does not occur due to intramolecular electronic interactions, but instead due to strain in the crystal lattice and/or intermolecular interactions that are not accounted for in these calculations.

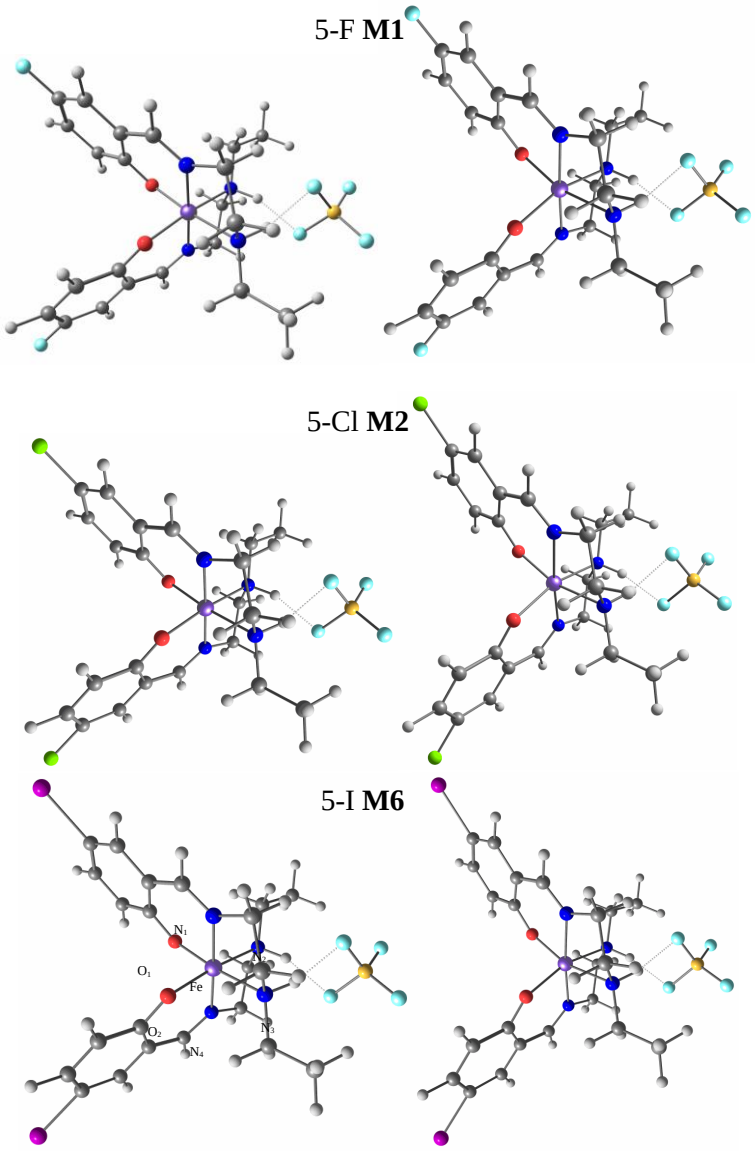

Figure 2.3 *DFT optimised structures obtained for the three tetrafluoroborate compounds (LS-left, HS-right).*

The bond lengths obtained for the coordination sphere are described in **Table 2.2** and they are discussed below as well as the relevant intermolecular bonding observed.

Table 2.2 *Fe-Ligand atom bond length for the DFT optimised structures of the tetrafluoroborate compounds.*

Bond length / Å		*5-F (**M1**)*	*5-Cl (**M2**)*	*5-I (**M6**)*
LS	Fe-N_1	1.984	1.985	1.986
	Fe-N_2	2.110	2.112	2.111
	Fe-N_3	2.109	2.112	2.111
	Fe-N_4	1.984	1.985	1.986
	Fe-O_1	1.923	1.925	1.926
	Fe-O_2	1.922	1.925	1.926
HS	Fe-N_1	2.184	2.187	2.190
	Fe-N_2	2.271	2.276	2.278
	Fe-N_3	2.272	2.276	2.278
	Fe-N_4	2.183	2.187	2.190
	Fe-O_1	1.978	1.980	1.983
	Fe-O_2	1.978	1.981	1.983

The values obtained and recorded in **Table 2.2** are consistent with the values obtained experimentally in the literature for such compounds. In the three compounds and in both spin states, there are hydrogen bonds between the fluorine atoms of the anion and the amine protons of the ligands. These N-H···F bonds have an average length of 1.928 Å and angle of 157º in the LS structures and average length and angle of 1.886 Å and 165º, respectively, in the HS structures.

While the halogen substitution seems to not affect the characteristics of the hydrogen bonds between the ionic pair – which is why the values were reported as averages – it does affect the bond length in the coordination sphere, key factor in the ability of compounds to undergo spin crossover. There is a significant increase in length from **M1** to **M2** in both spin states, indicating that **M2** should yield grater stability at the HS state. Even though there is a slight increase, in general, in bond length, from **M2** to **M6**, the difference is less significant. This is probably due to the fact that fluorine does not exhibit the halogen-typical sigma-hole electrostatic field and, thus, draws considerably less electron density from the iron centre.

2.1.2 Tetraphenylborate complexes

2.1.2.1 Crystals obtained in DMF and MeOH

The crystals obtained from the mentioned tridentate ligands and iron(II) tetraphenylborate hydrate were characterised by FTIR, SQUID, Elemental Analysis and Mössbauer spectroscopy.

FTIR spectroscopy was mainly used to confirm the imine formation through the observation of a strong stretching vibration with an energy close to 1600 cm^{-1} and the presence of the tetraphenylborate anion through its stretching bands at 740 and 710 cm^{-1}.

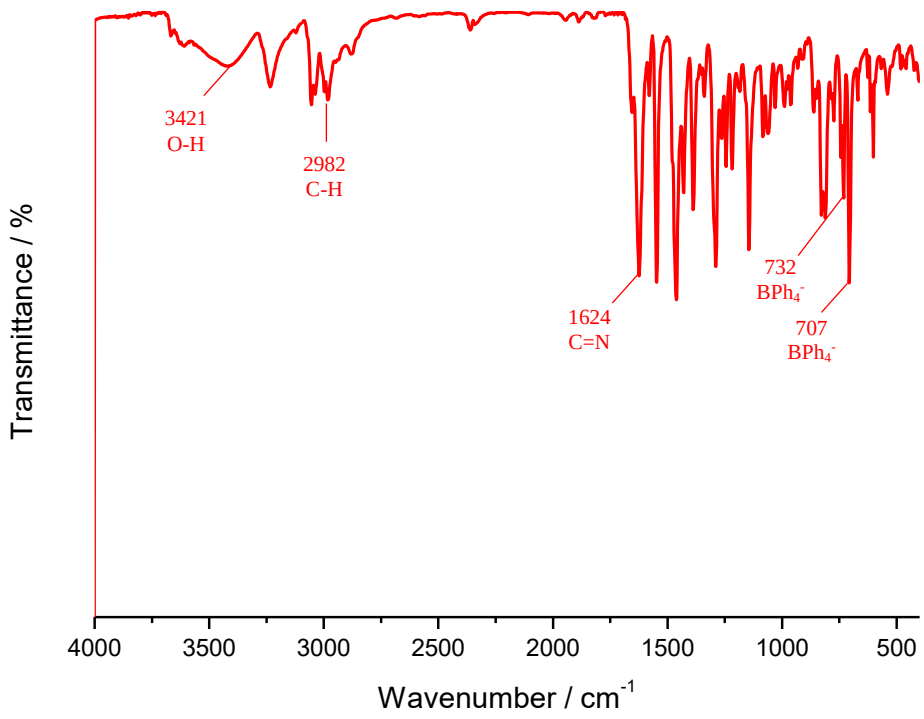

Figure 2.4 *FTIR spectrum of* ***M3****.* ***M4*** *and* ***M5*** *spectra can be found in* ***Figure 6.2*** *and* ***Figure 6.3****.*

2.1.2.2 Magnetic characterisation

The SQUID magnetometry plots for DMF/MeOH crystals of the tetraphenylborate compounds can be analysed in **Figure 2.5**. The measurements were again conducted in polycrystalline samples, with alternating cooling/warming runs at 5 K min^{-1}.

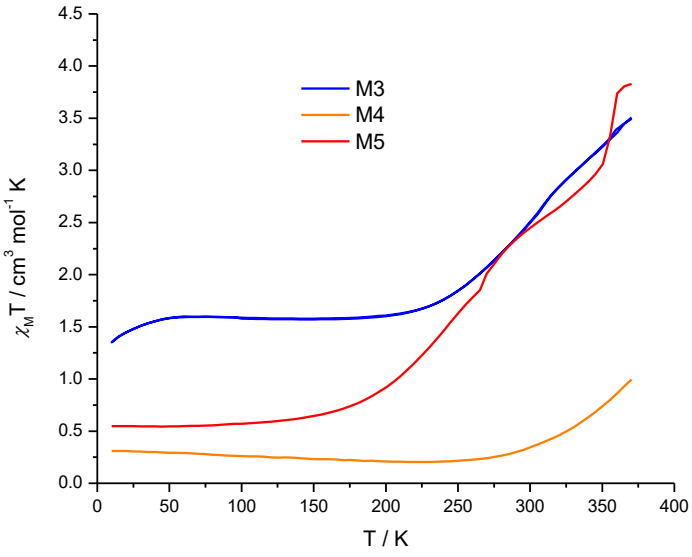

Figure 2.5 *$\chi_M T$ vs T plots for the three compounds synthesised with tetraphenylborate anions, in DMF [****M3*** *(F) and* ***M4*** *(Cl)] and MeOH [****M5*** *(I)].*

The measurement of **M3** started at 370 K with a $\chi_M T$ value of 3.49 $cm^3\ mol^{-1}\ K$, corresponding to a distribution comprised of, approximately, 78% high-spin Fe^{III} and 22% low-spin Fe^{III} centres. Then, the sample was cooled to 10 K and the $\chi_M T$ value decreased gradually to 1.35 $cm^3\ mol^{-1}\ K$, which does not correspond to a complete array of low-spin Fe^{III}, but to a 24% fraction of high-spin Fe^{III} centres. The $\chi_M T$ value obtained at 300 K for **M3** and for the analogous tetrafluoroborate compound was the same. Afterwards, there was a final warming run up to 370 K and the $\chi_M T$ value gradually increased to 3.51 $cm^3\ mol^{-1}\ K$, close to the one measured at the beginning of the experiment.

At the initial 300 K, a $\chi_M T$ value of 0.34 $cm^3\ mol^{-1}\ K$ was observed for **M4**. The sample was cooled to 10 K and displayed a $\chi_M T$ value of 0.31 $cm^3\ mol^{-1}\ K$. Finally, a warming run was employed up to 370 K until $\chi_M T$ reached 0.99 $cm^3\ mol^{-1}\ K$. These results indicate that all the Fe^{III} centres are stabilised at the LS state during most of the analysis. There is a slight gradual increase in $\chi_M T$ from 300 K onwards, suggesting there may be a spin transition at higher temperatures than 400 K. Therefore, a SQUID measurement installing an oven for high-temperature measurements would be extremely clarifying.

The final complex, **M5**, displays a rather unusual magnetic behaviour. The Fe centres are in the LS state at low temperatures and a gradual increase in $\chi_M T$ is observed from 0.69 $cm^3\ mol^{-1}\ K$ to 2.87 $cm^3\ mol^{-1}\ K$ at 300 K. Afterwards, a sharp increase in $\chi_M T$ to 4.72 $cm^3\ mol^{-1}\ K$ is noted. Finally, on cooling the sample, $\chi_M T$ stabilises close to 4.32 $cm^3\ mol^{-1}\ K$, suggesting that solvent (MeOH) molecules leave the crystal lattice and the Fe^{III} stabilises in the HS state, from then on.

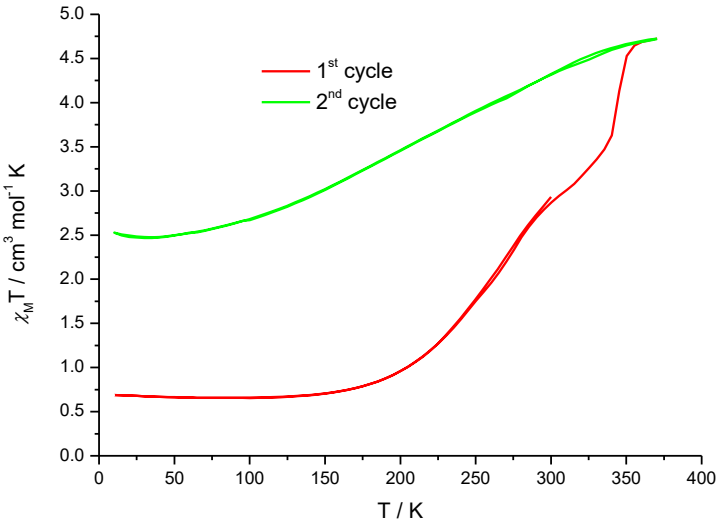

Figure 2.6 *$\chi_M T$ vs T plot for **M5**.*

Mössbauer spectroscopy was used in samples containing ground crystals of these compounds at room temperature, in order to confirm the oxidation state of iron and obtain further information about the spin state of the metal centres (**Figure 2.7**). Two doublets were fitted in the spectrum of **M4**. It was not possible yet no get good fitting for the spectra obtained for **M3** and **M5**.

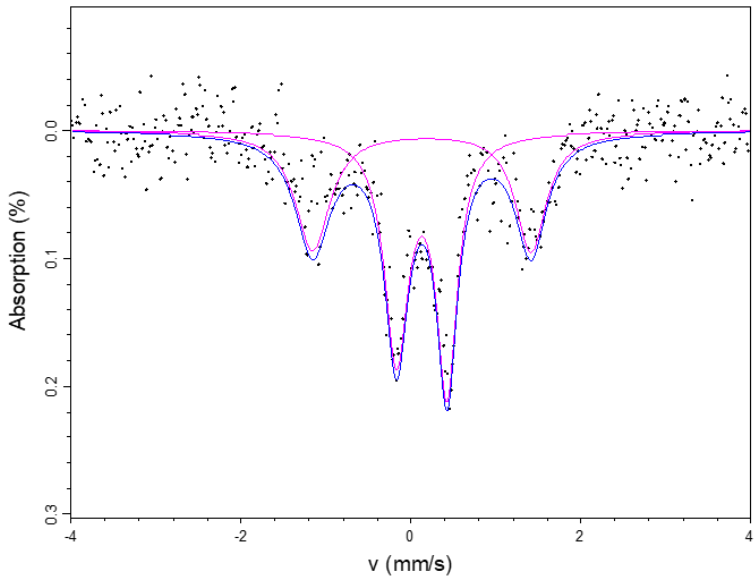

Figure 2.7 *Mössbauer spectrum for* ***M4*** *crystals obtained from a DMF solution.*

The relevant parameters obtained from this spectrum are shown in **Table 2.3**.

Table 2.3 *Mössbauer parameters for* ***M4****. The relative widths and intensities of the doublets were close to 1.0 (1.14 and 1.0, respectively).*

	Doublet 1			*Doublet 2*		
	IS / mm s^{-1}	QS / mm s^{-1}	Site Population	IS / mm s^{-1}	QS / mm s^{-1}	Site Population
M4	0.124	0.595	57 %	0.126	2.570	43 %

The Mössbauer spectrum for **M4** was fitted with two doublets with isomer shifts characteristic of LS Fe^{III}, which is in agreement with the SQUID magnetometry results. The existence of two doublets in the spectrum suggests that there are two isomers of the same molecule in the grounded sample, with an almost 50/50 distribution. The doublet with the highest quadrupole splitting corresponds to the least symmetric isomer.

2.1.2.3 Crystals obtained in acetonitrile

M3 and **M4** were also crystallized from acetonitrile and the magnetic properties obtained were rather different (**Figure 2.8** and **Figure 2.9**), although the method used for the measurements was equivalent.

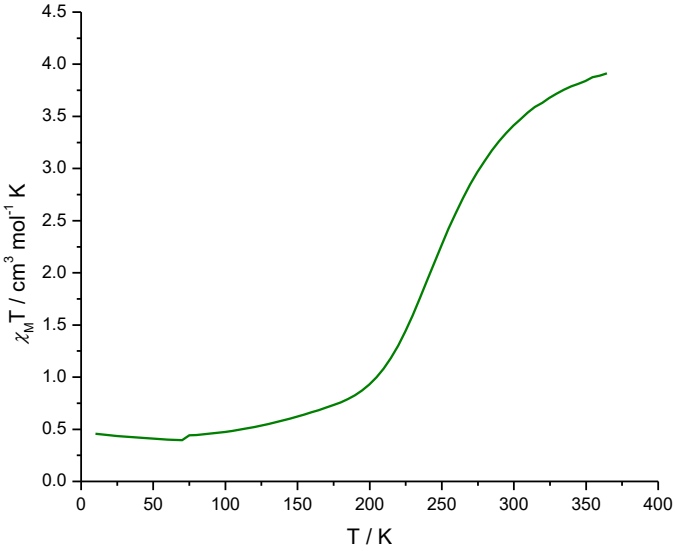

Figure 2.8 *χ_MT vs T plot for **M3** (F, ACN).*

The magnetisation measurement for **M3** (ACN) started at 300 K with a χ_MT value of 3.59 cm^3 mol^{-1} K which corresponds to a distribution of 80% of HS Fe^{III}, very close to the previously mentioned compounds. Then, the sample was cooled to 10 K, displaying a χ_MT value of 0.43 cm^3 mol^{-1} K, the value expected for LS Fe^{III}. Finally, a warming run showed a χ_MT increase up to 3.93 cm^3 mol^{-1} K, indicating a population of 89% of the Fe^{III} centres in the HS state. A second cooling/warming cycle was measured, and the magnetic profile exhibited was analogous, only with a slight decrease in absolute χ_MT values, which suggests that the crystals have no solvent molecules in their structure, but probably have some acetonitrile molecules adsorbed in their surface, which evaporate at 370 K.

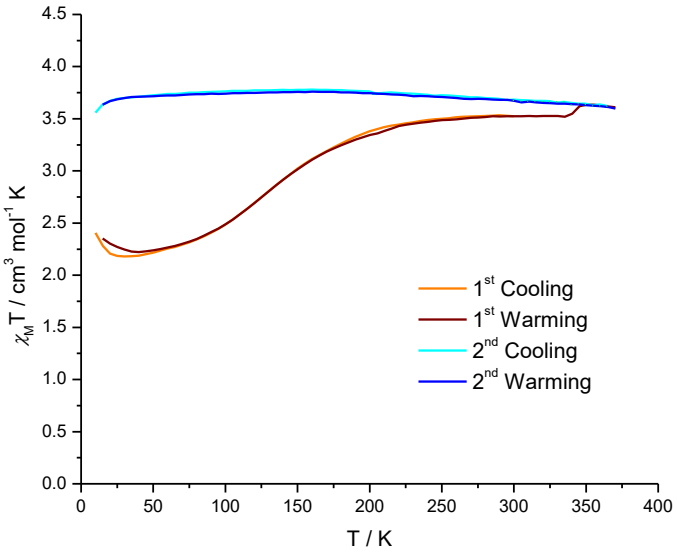

Figure 2.9 *χ_MT vs T plot for **M4**(Cl, ACN).*

The SQUID results for **M4** (ACN) clearly shows that acetonitrile molecules were included in the crystal structure of the compound. While the first cooling/warming run shows a gradual and very incomplete spin crossover between two mixed population states, the second cooling/warming run registered an almost constant $\chi_M T$ value of 3.67 cm^3 mol^{-1} K, showing a stable population of 82% HS Fe^{III} centres.

2.1.2.4 DFT calculations

DFT calculations (ADF, B3LYP*/TZP fc) were employed to try to understand the magnetic behaviour of the compounds in further detail, although no explicit solvent molecules were included in the structures. Geometry optimisations were carried out for the S=1/2 and S=5/2 spin states, their energies calculated, and the results are presented in **Table 2.4**.

Table 2.4 *Energy difference (kcal mol^{-1}) between the high-spin and low-spin DFT optimised structures for the BPh_4 series of compounds.*

Compound	ΔE_{HS-LS}
*[Fe(5-F-salEen)$_2$]BPh_4 (**M3**)*	3.84
*[Fe(5-Cl-salEen)$_2$]BPh_4 (**M4**)*	6.25
*[Fe(5-I-salEen)$_2$]BPh_4 (**M5**)*	6.02

If we compare the DFT results with the $T_{1/2}$ of these compounds, they are actually in quite good agreement with the experimental results for the crystals obtained, in spite of the crystallisation solvent. A lower $T_{1/2}$ was expected for **M3** and that is observed both in the DMF crystals and the ACN crystals. **M4** has an energy difference between both spin states of almost double of **M3**, which may be the reason why **M4** does not undergo SCO in either crystal. **M5** exhibited a change in its magnetic profile, due to a likely solvent evaporation and, thus, no considerations may be undertaken from the comparison with the theoretical calculations.

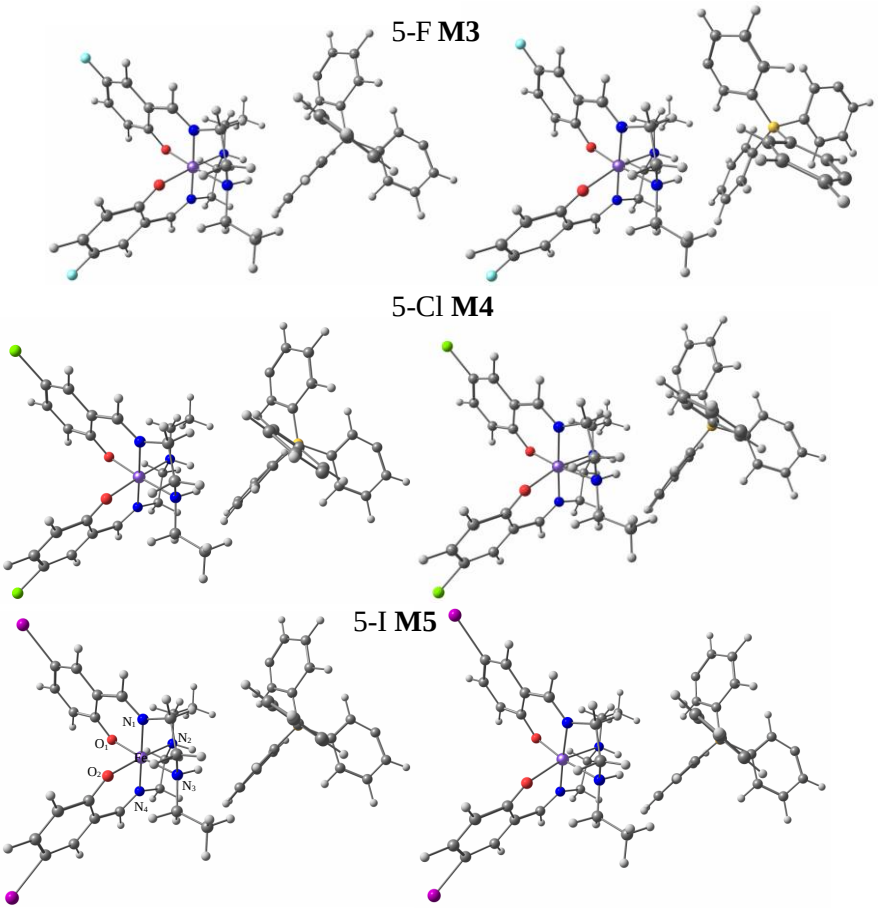

Figure 2.10 *DFT optimised structures for the three tetraphenylborate compounds (LS-left, HS-right).*

The bond lengths obtained for the coordination sphere are described in **Table 2.5** and are discussed below.

Table 2.5 *Fe-Ligand atom bond length for the DFT optimised structures of the tetraphenylborate compounds.*

Bond length / Å		*5-F (**M3**)*	*5-Cl (**M4**)*	*5-I (**M5**)*
LS	Fe-N_1	1.977	1.979	1.979
	Fe-N_2	2.135	2.138	2.139
	Fe-N_3	2.138	2.140	2.138
	Fe-N_4	1.976	1.978	1.981
	Fe-O_1	1.950	1.954	1.956
	Fe-O_2	1.950	1.955	1.958
HS	Fe-N_1	2.032	2.032	2.034
	Fe-N_2	2.163	2.167	2.175
	Fe-N_3	**2.454**	**2.470**	**2.465**
	Fe-N_4	1.952	1.958	1.956
	Fe-O_1	2.079	2.082	2.083
	Fe-O_2	1.942	1.948	1.956

The values obtained and recorded in **Table 2.5** are not consistent with those in the literature for each spin state, as the bonds are too long, particularly those highlighted in red. This may indicate that the theoretical model chosen is not adequate for the tetraphenylborate compounds and, thus, another model should be used, at least for the optimisation of the structure.

A final comparison between the DFT calculated values for both series of compounds can be found in **Figure 2.11**.

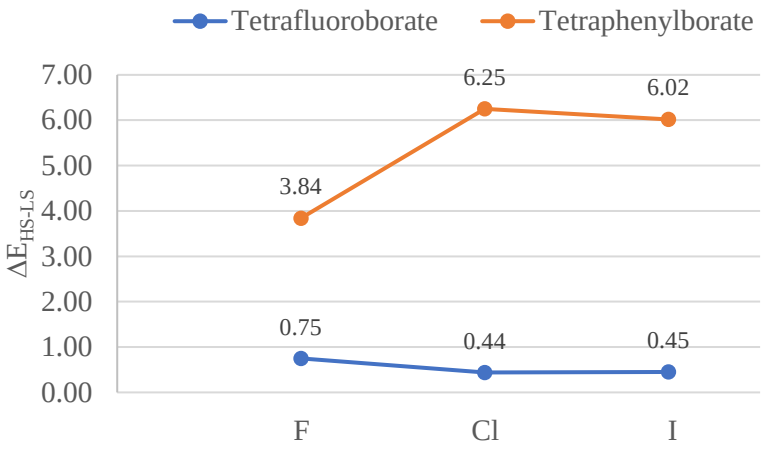

Figure 2.11 *Comparison between the $\Delta E_{(HS-LS)}$ values (kcal mol^{-1}) for the two different anions.*

The energy difference for the tetrafluoroborate series is of a much lower magnitude, thus these compounds have a higher probability of displaying the SCO phenomenon. This may be due to the hydrogen bonds that were obtained for the tetrafluoroborate compounds but not for the tetraphenylborate compounds as the latter do not have an electronegative atom. For both series, the fluorine substituted compounds represent a considerably different value than those for the remaining halogens. This is probably due to the fact that fluorine has such a negligible electron density that the electron-withdrawing effect from the Fe-donor atom does not affect the spin crossover behaviour of the compound significantly. The reason why there is a decrease in energy difference, for the tetraphenylborate compounds, and not an increase may be due to the model used for these structures not being ideal.

2.1.3 Complexes with hexadentate ligands

Crystals of a compound with an analogous hexadentate ligand and the perchlorate anion, **H1**, were also obtained. FTIR spectroscopy was employed in order to confirm the imine formation (1600 cm^{-1}) and the presence of the perchlorate counter ion (**Figure 2.12**).

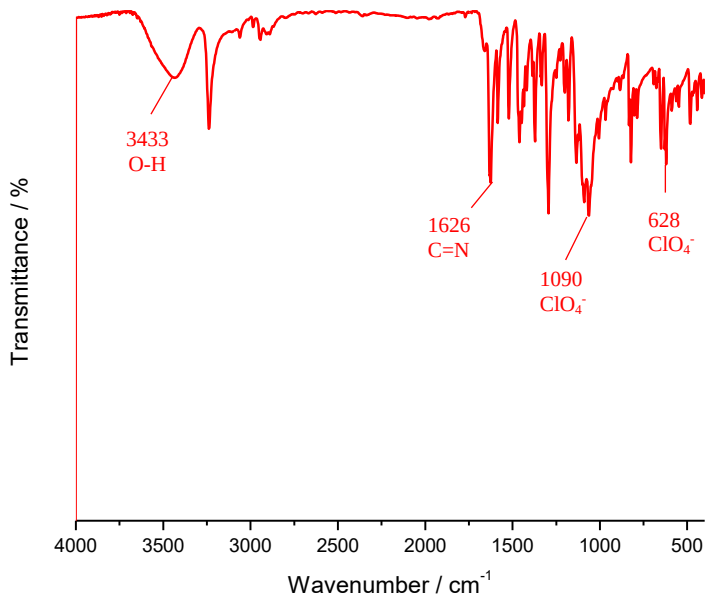

Figure 2.12 *FTIR spectrum for **H1**.*

2.1.3.1 Magnetic characterisation

The SQUID magnetometry plot was also traced for this compound and can be found in **Figure 2.13**. The method used here was analogous to that of the mononuclear, tridentate compounds.

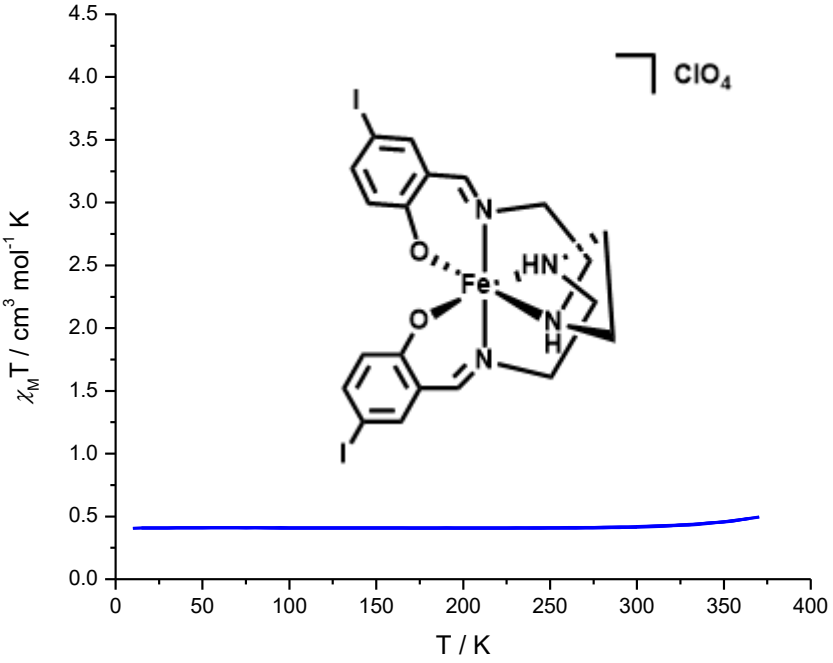

Figure 2.13 *$\chi_M T$ vs T plot for complex* ***H1****.*

H1 exhibits an almost constant $\chi_M T$ value of 0.41 cm^3 mol^{-1} K, which is characteristic of Fe^{III} LS metal ions, throughout the temperature range 10-370 K. $\chi_M T$ starts increasing around 300 K and reaches a maximum of 0.50 cm^3 mol^{-1} K at 370 K. The slight increase in $\chi_M T$ at high temperatures suggest that a spin transition may occur above 370 K, hence, in this case, high-temperature measurements with an oven instalment would also be useful for the clarification of this hypothesis.

2.1.3.2 DFT calculations

DFT calculations have been employed using a similar theoretical method as for the mononuclear compounds, in order to establish relationships between this compound and the analogous complex with tridentate ligands.[88] These, however, have not been finished in time.

2.2 Binuclear compounds

2.2.1 Hydrazide ligands

The compounds presented in section 2.2.1 were synthesised and characterised by NMR spectroscopy by the BSc Rafaela T. Marques. The single crystal X-ray structure presented was obtained by Dr Sónia Barroso at FCT, UNL (REQUIMTE). I was responsible for the synthesis supervision, treatment of the raw SQUID data and the theoretical calculations, the latter with help from Dr Nuno Bandeira.

Several binuclear Fe^{III} complexes were also synthesised, based in hydrazide ligands with different substituents in their phenyl rings. The reaction mechanism for the synthesis of the ligands is presented below (**Scheme 2.4**). Excess of hydrazine hydrate is dissolved in ethanol and the first salicylaldehyde is added dropwise. After 3 hours of stirring, a yellow solution is obtained, the solvent is evaporated and the mono-substituted hydrazine is recovered by cold precipitation in a methanol and water solution. Then, this compound is again dissolved in ethanol and the second salicylaldehyde is added in stoichiometric amounts. It is left stirring for 30 minutes until then final yellow product precipitates and is finally recovered by filtration.

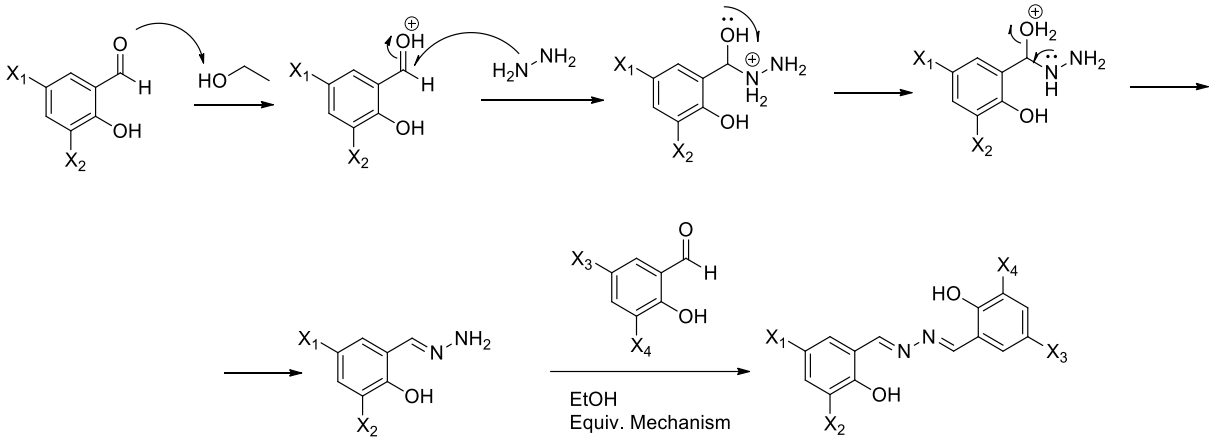

Scheme 2.4 *Reaction mechanism for the synthesis of the hydrazine ligands.*

Four different ligands were obtained following the said synthesis: L_1 (X_1, X_2, X_3, X_4 = H), L_2 (X_1, X_2, X_4 = H; X_3 = Br), L_3 (X_1, X_2 =H; X_3, X_4 = Br) and L_4 (X_1, X_2 = H; X_3 =Cl; X_4 = Br), **Figure 2.14**. The Nuclear Magnetic Resonance (NMR) spectroscopy characterisation of these compounds was done resorting to ^{1}H, ^{13}C APT, COSY, HSQC and HMBC experiments, since both homonuclear and heteronuclear experiments are usually necessary for the full attribution of the NMR peaks. These results can be found in the Supporting Information, as well as some sample spectra obtained.

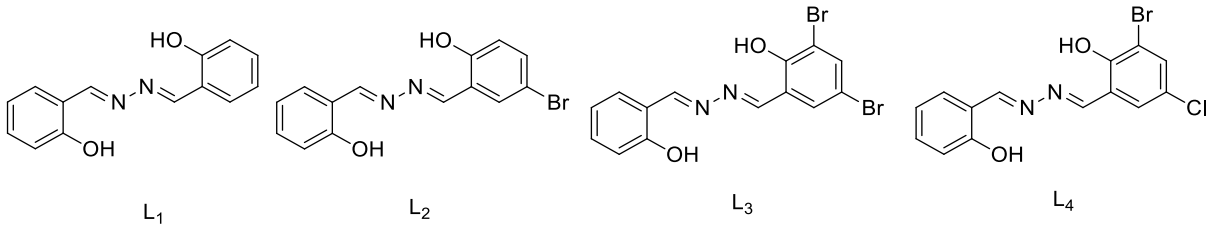

Figure 2.14 *Ligands used in the synthesis of binuclear Fe^{III} complexes.*

Iron complexes were then obtained by addition of iron(III) chloride (in a 2:3 proportion) to an acetonitrile solution of the desired ligand, under stirring and reflux for 3 hours, with a few drops of triethylamine. Crystals of the complexes (**B1** from L_1, **B2** from L_2, **B3** from L_3 and **B4** from L_4) were obtained by slow evaporation at room temperature.

SQUID magnetometry measurements were conducted in order to determine the magnetic properties of these compounds. The results obtained are shown in **Figure 2.15**.

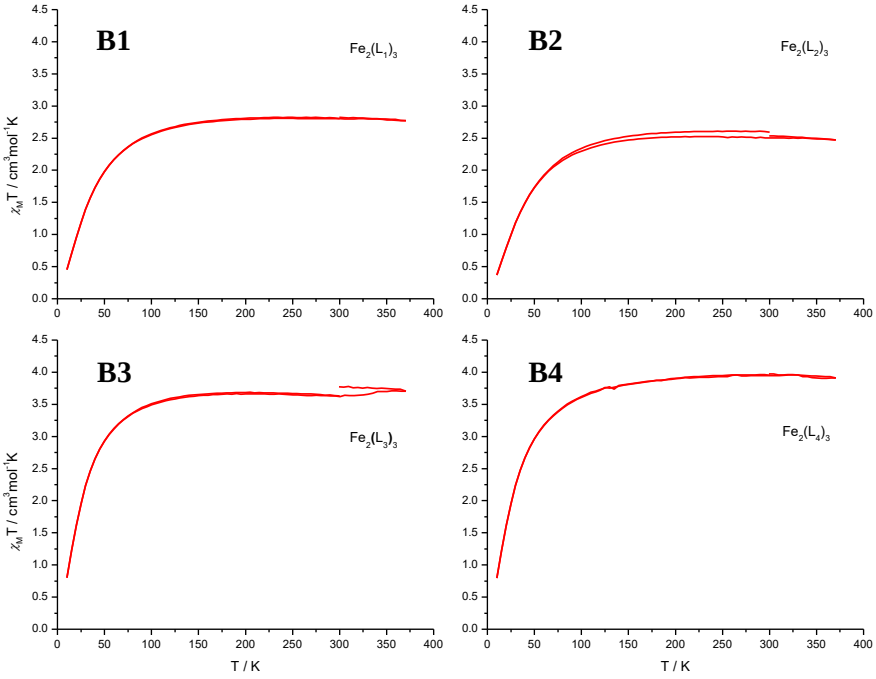

Figure 2.15 *$\chi_M T$ vs T plots for the binuclear Fe^{III} compounds.*

As one can observe in **Figure 2.15**, the magnetic behaviour for all four complexes is very similar. The results presented are for each iron atom, and not total $\chi_M T$ for the compounds. The complexes exhibit constant $\chi_M T$ values (2.80, 2.50, 3.62 and 3.95 $cm^3\ mol^{-1}\ K$, respectively) down to approximately 100 K, when antiferromagnetic ordering occurs and $\chi_M T$ starts decreasing gradually until spin-orbit effects are noticeable and $\chi_M T$ decreases abruptly. The antiferromagnetic effect was confirmed by a curve inversion noticeable in the χ_M plots displayed in **Figure 6.14**.

Theoretical calculations using the Broken Symmetry Approach[89] were thus performed in order to assess the magnitude of this antiferromagnetic ordering, through the calculation of the isotropic interaction parameter, *J* (one should note that for the case of a binuclear complex with Fe^{III} ions in the HS state, a pair of local $S_1=S_2=5/2$ spins is the best representation of the system).[90]

Geometry optimisations with no symmetry constraints were hence conducted, using a B3LYP*/TZP (core none) theoretical model, for all the four complexes. The starting geometry provided for the calculation was the crystal structure of the unit cell obtained for $Fe_2(L_1)_3$ at 296 K (**Figure 2.16**, Left). The solvent molecule was removed from the unit cell and the necessary atom replacements were performed to accurately model the remaining three compounds.

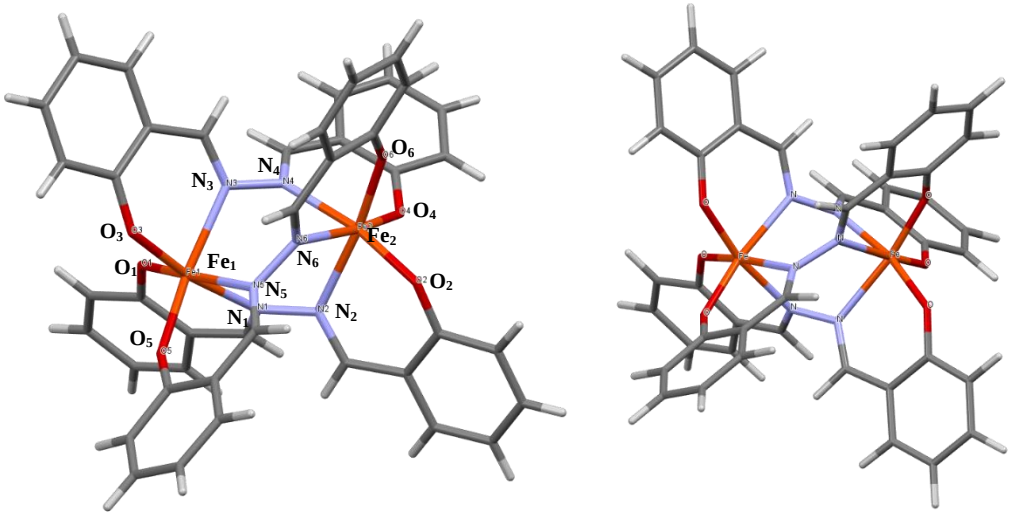

Figure 2.16 *Unit cell for* ***B1*** *as obtained through Single Crystal X-ray Crystallography at 296 K (left); solvent (acetonitrile) molecule removed since it is not relevant for the computational model. Right: DFT optimised structure for* ***B1*** *(right). The remaining DFT structures can be found in* ***Figure 2.17****.*

The theoretically obtained structure for **B1** was very similar to the SCXRD structure (**Figure 2.16**, Right). The Fe-ligand atom bond lengths are in agreement with those obtained experimentally, as these only increased slightly (the largest difference found was 2.76%). The relevant bonds are presented in **Table 2.6**. The bond lengths obtained by SCXRD and DFT are both consistent with Fe^{III} centres in the HS state.

Table 2.6 *Iron-Ligand atom bond lengths as obtained through SCXRD (Å) and corresponding increase (%) in the DFT structure for* $Fe_2(L_1)_3$*.*

	Bond length / Å					
Fe_2	2.180	2.195	2.170	1.906	1.922	1.925
Fe_2(DFT)	+2.34%	+2.00%	+2.76%	+1.42%	+0.57%	+0.42%
Fe_1	2.183	2.186	2.166	1.922	1.915	1.904
Fe_1(DFT)	+2.02%	+1.88%	+2.68%	+0.62%	+0.94%	+1.68%
	N_4/N_1	N_2/N_3	N_6/N_5	O_4/O_1	O_2/O_3	O_6/O_5

The DFT optimised structures were also obtained for the remaining compounds, starting from the SCXRD structure and upon substitution of the appropriate atoms. These can be observed in **Figure 2.17**.

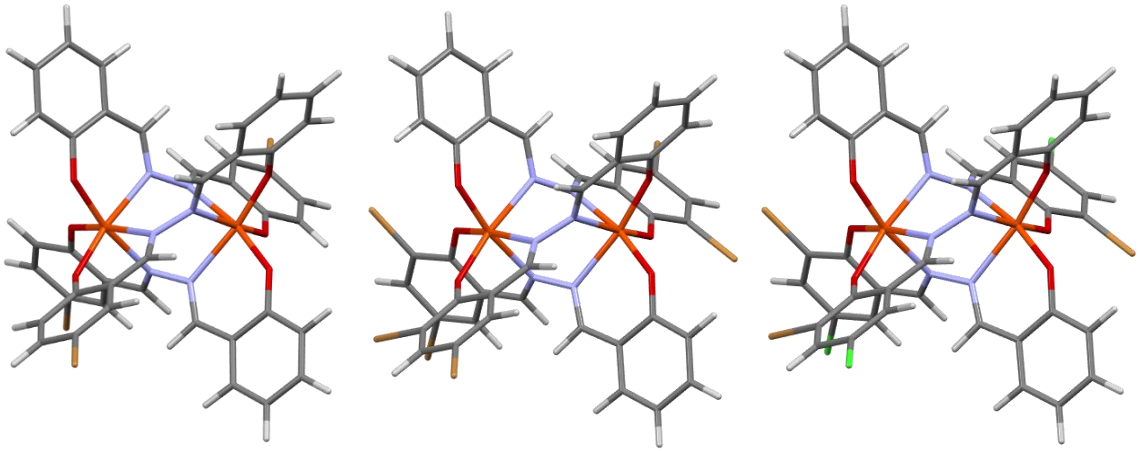

Figure 2.17 *DFT optimised structures of* ***B2*** *(left),* ***B3*** *(centre) and* ***B4*** *(right).*

A comparison of the bond lengths between all the DFT optimised structures can be established, with reference to **B1**. These may be observed in **Table 2.7**.

Table 2.7 *Fe-Donor atom bond lengths relative to those of* ***B1*** *of all the DFT optimised structures.*

Bond length / Å	***B1***	***B2***	***B3***	***B4***
Fe_1-N_1	0.000	-0.001	0.002	0.000
Fe_1-N_3	0.000	0.001	-0.010	-0.002
Fe_1-N_5	0.000	0.015	-0.008	-0.002
Fe_1-O_1	0.000	0.004	0.004	0.006
Fe_1-O_3	0.000	-0.004	-0.013	-0.012
Fe_1-O_5	0.000	0.003	0.015	0.013
Fe_2-N_2	0.000	-0.011	0.007	0.006
Fe_2-N_4	0.000	0.012	-0.006	-0.008
Fe_2-N_6	0.000	0.003	0.005	0.008
Fe_2-O_2	0.000	-0.002	-0.011	-0.011
Fe_2-O_4	0.000	0.005	0.014	0.015
Fe_2-O_6	0.000	-0.003	-0.003	-0.004

All the bond lengths correspond to Fe^{III} centres in the HS state. Although most bonds are very similar in length to those of the base compound, there are some that are clearly either elongated or shortened, due to the presence of the halogen atoms. These structural changes should be responsible for the differences observed in the magnetic profiles of the compounds.

An unrestricted calculation was first performed for the S=5 states. Then a spinflip was induced in one of the iron centres and symmetry is broken through an S=0 state energy calculation, localising five unpaired electrons in one of the iron centres. This was confirmed by the observation of a symmetric value in the density of the spin calculated for each of the iron atoms.

The energy difference between both spin states is then equal to 15*J*, due to the high multiplicity value associated to HS Fe^{III}. The calculated isotropic interaction parameters are presented in **Table 2.8**.

Table 2.8 *Exchange coupling constants calculated for the binuclear* Fe^{III} *compounds following the Broken Symmetry Approach (B3LYP*/TZP nc).*

Complex	**J / cm^{-1}**
B1	-8.74
B2	-18.65
B3	-18.65
B4	-18.65

As expected from the magnetic plots, an antiferromagnetic coupling was calculated for all the complexes. It is very interesting to note that although there is no difference between the substituted compounds, the presence of halogen atoms in the phenolic rings of the ligands seems to greatly increase this coupling.

B1 contains symmetric ligands but also exhibits some antiferromagnetic coupling, instead of a J equal to zero, as expected in symmetric molecules. This is due to the fact that both iron coordination spheres are not identical at all, which is observable in the different Fe-ligand atom bond lengths for each of the iron centres.

2.3 Multinuclear compounds

The compounds in section 2.3 were synthesised and characterised by the me. Dr Liliana P. Ferreira was responsible for the collection of the SQUID raw data.

Following the work of Nitschke's Group (University of Cambridge) on metal-organic molecular cages for the encapsulation of small molecules, we wondered if that kind of architectures would have interesting magnetic properties. Thus, a similar synthetic route was undertaken with a new Schiff-base ligand (**Scheme 2.5**) and a different metal salt (iron(II) triflate) and cobalt(II) perchlorate hydrate.

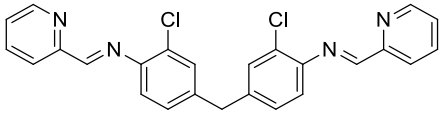

Scheme 2.5 *Ligand synthesised for the molecular cages.*

Under inert atmosphere, 4,4′-Methylene-bis(2-chloroaniline) was dissolved in previously distilled acetonitrile and the aldehyde was added to the solution, along with a drop of hydrochloric acid. After the synthesis of the ligand, the Fe^{II} salt was added in a 2:3 proportion and the mixture was left to react at 323 K for two days. A purple powder was obtained after the addition of diisopropylether. Several attempts to crystallise the compound were made, mainly through layer diffusion techniques, but crystals have not been formed so far. The 2:3 - Fe:Ligand ratio was used in order to induce the formation of tetrahedron-shaped cages (**Figure 2.18**).

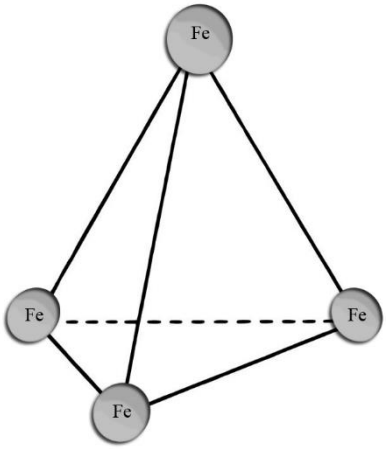

Figure 2.18 *Shape predicted for the resulting cage from the Metal:Ligand ratio chosen for the synthesis.*

2.3.1 Fe(II) cage characterisation

The purple powder obtained from the synthesis was characterised by FTIR spectroscopy and SQUID magnetometry.

FTIR spectroscopy was mainly used to confirm the imine formation through the observation of a strong stretching vibration with an energy close to 1600 cm^{-1} and the presence of the trifluoromethanosulfate anion through its stretching band near 1030 cm^{-1}.

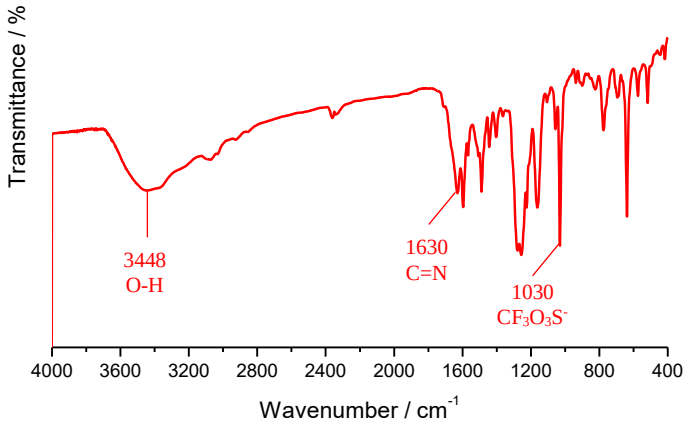

Figure 2.19 *FTIR spectrum of the Fe Cage.*

The magnetic behaviour of the powdered sample was analysed by SQUID and can be observed in **Figure 2.20**.

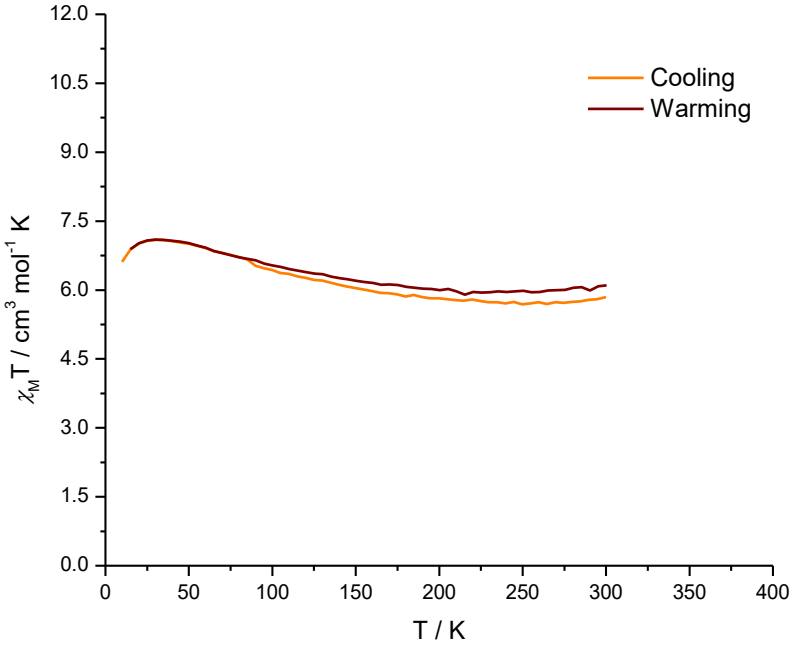

Figure 2.20 *$\chi_M T$ vs T plot for the Fe cage.*

The compound exhibits an almost constant value of $\chi_M T$ from 300 K to 200 K and then there is a slight increase in $\chi_M T$. This result suggests that there may be a weak ferromagnetic coupling between the iron centres when the temperature is lower. An antiferromagnetic coupling effect and/or zero field splitting is observable at temperatures below 20 K.

2.4 Micro- and nano-structures

The compounds in section 2.4 were synthesised by me. Dr Liliana P. Ferreira was responsible for the collection of the SQUID raw data. Dr Ana I. Vicente was responsible for the AFM images collection. Dr Ana C. Mourato was responsible for the PXRD analysis.

In order to study the size effect on the magnetic properties of aggregates of molecules, attempts were made in order to synthesise micro/nanostructures with spin crossover behaviour, from a previously reported compound, **NP** ([Fe(5-I-salEen)$_2$)]ClO_4, **Scheme 2.6**).[88] Two methods were used, essentially: one that consisted on the slow evaporation of the solvent in a diluted solution under pressure; other that consisted on the synthesis of particles in solution, in a polymeric polyethylene glycol (PEG) matrix, containing the desired iron salt and ligand in adequate proportions.

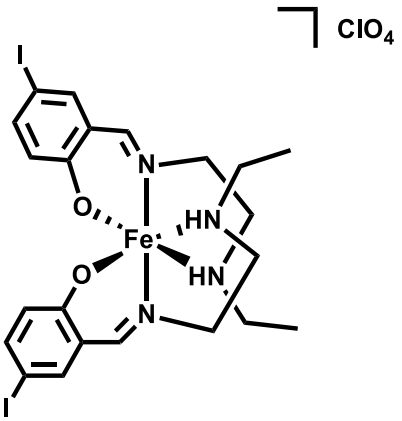

Scheme 2.6 *NP molecular structure.*

2.4.1 PEG matrix particles

Particles of **NP** with different sizes were obtained following a previously published method[91] in which the desired iron salt and ligand are dissolved in separate solutions of Millipore water and methanol, with a controlled amount of PEG and PEG/Fe ratio. The ligand/PEG solution is then slowly added to the Fe/PEG solution while stirring (**Scheme 2.7**). Finally, the resulting dispersion is filtered and the particles are washed with Millipore water and methanol.

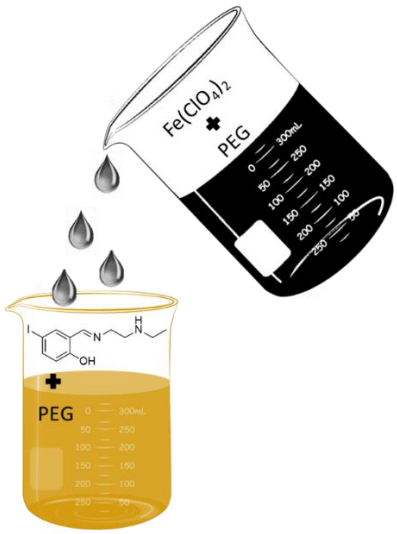

Scheme 2.7 *Method for the preparation of the **NP** particles.*

The synthesis was also attempted using only methanol solutions, however, no particles were obtained, which suggests that water plays a critical role on the particle formation possibly because PEG shows surfactant behaviour thus creating aggregates where the particle formation occurs. Rather homogeneous particle dispersions were obtained with size dependant of the amount of PEG added during the syntheses. The diameter of the aggregates/particles, as obtained through Atomic Force Microscopy (AFM) image measurements, is recorded in **Table 2.9**.

Table 2.9 *Apparent average particle size as obtained through AFM imaging for the different particle syntheses.*

Total amount of PEG added during the synthesis / ml	Apparent average particle size / nm
0.50	**10.4**
0.70	**12.6**
1.00	**26.9**
1.50	**13.0**
2.00	**20.3**

A decrease of the particle size was expected as the amount of PEG added diminished, since the amount of Fe in all the syntheses was maintained. However, this is not the case, it seems. The outlier observed for the particles synthesised with 1.00 ml of PEG may be due to a higher degree of aggregation of the particles, in spite of the sample preparation for the AFM images having been the same.

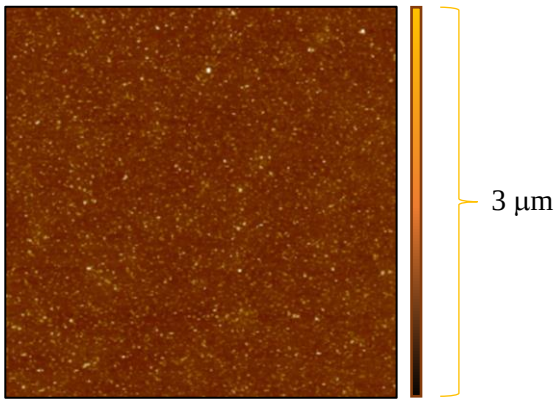

Figure 2.21 *AFM image of the particles synthesised with 0.50 of PEG. Window size: 3x3 μm. The images for the remaining particles can be observed in* ***Figure 6.15*** *and* ***Figure 6.16****.*

In order to further study the size of these particles, NANO-flex measurements were performed in chloroform dispersions of these particles, with a concentration of $1x10^{-5}$ M. The results obtained for the two particles with lowest amount of PEG added, are displayed in **Figure 2.22** and **Figure 2.23**. It was not possible for the apparatus to perform accurate measurements on the remaining samples, probably due to a low total amount of particles in the dispersions that were prepared.

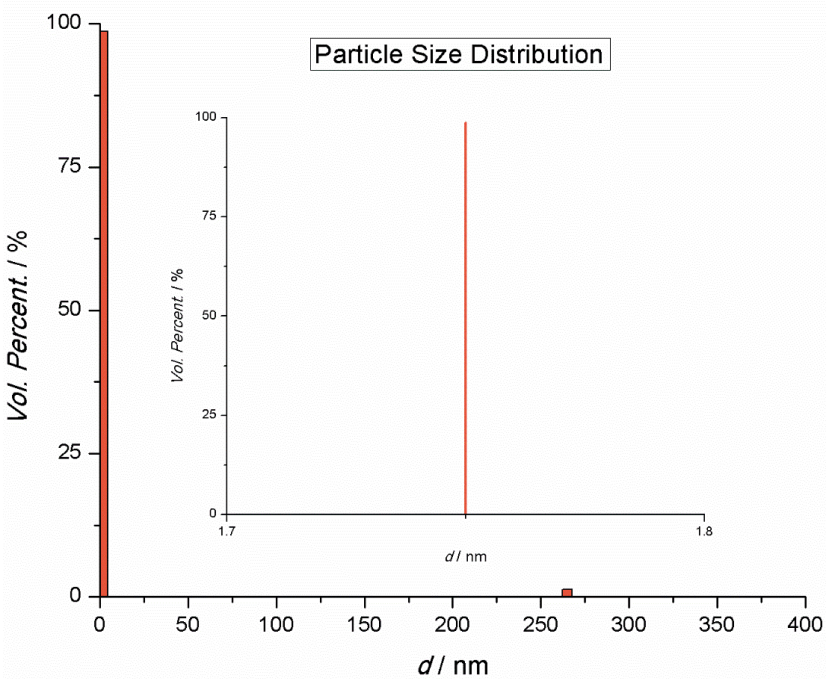

Figure 2.22 *Particle size distribution as determined by NANO-flex for the 0.50 PEG Nano-particles.*

In the case of the particles synthesised with the lowest amount of PEG, 98.7% of these displayed a size of 1.75 nm and 1.3% a size of 265.00 nm. The largest particles either correspond to aggregates or, possibly, to polymeric chains. The high volume percentage of particles with 1.75 nm, which is almost the molecule size, indicates that most of the sample has suffered degradation in the solvent. The value is much lower than the one obtained through AFM, suggesting that the particles observed by the latter technique were also aggregates.

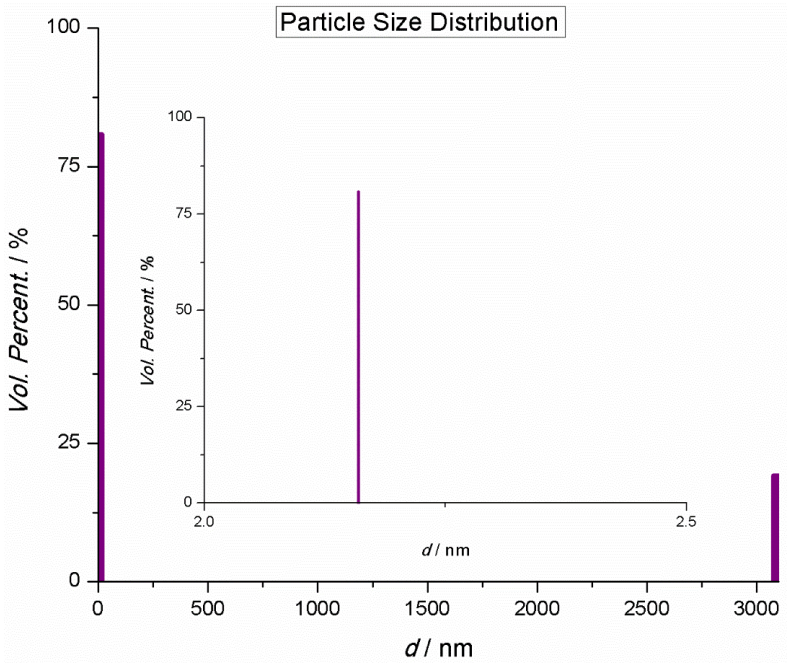

Figure 2.23 *Particle size distribution as determined by NANO-flex for the 1.00 PEG Nano-particles.*

The particles synthesised with 1.00 ml of PEG presented a distribution of 80.8% with 2.16 nm and 19.2% with 3090.00 nm. The same aggregation phenomenon is expected. Although the particle size is larger than the one obtained for the particles synthesised with 0.50 ml of PEG, which was expected, the size obtained through the NANO-flex was again much lower than that obtained by AFM.

The magnetic properties of these nanoparticles were studied by SQUID magnetometry, using a similar method than that for the remaining compounds, with a cooling/warming rate of 5 K min^{-1}. The results, taking into account only the molar mass of **NP**, are presented below.

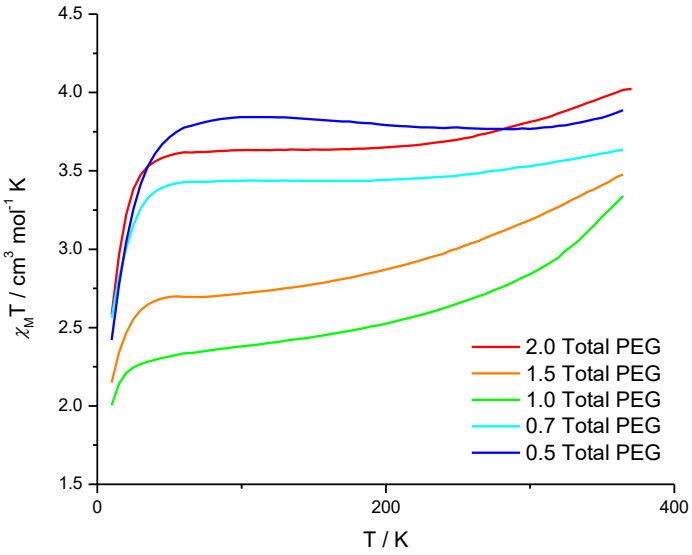

Figure 2.24 *$\chi_M T$ vs T plot for the synthesised nanoparticles. The value presented as line identifier corresponds to the amount of PEG added to each solution during the syntheses.*

As one can observe in **Figure 2.24**, all the particles that were obtained exhibit the SCO phenomenon to some extent. It is not accurate to make considerations on the $\chi_M T$, because the amount of polymer that is covering the particles is impossible to assess and it affects the molar mass which is required for the calculation of the molar magnetic susceptibilities. One can, however, still evaluate the difference $\Delta\chi_M T$, and the three cases for which the amount of PEG added was higher (and, thus, particles of bigger size should be obtained) are those who exhibit the largest $\Delta\chi_M T$, while the remaining two samples of particles exhibit almost no $\Delta\chi_M T$. This result suggests that the SCO phenomenon is curtailed as size diminishes, for this compound.

PXRD measurements were also conducted on the nanoparticles in order to further characterise them (**Figure 2.25**).

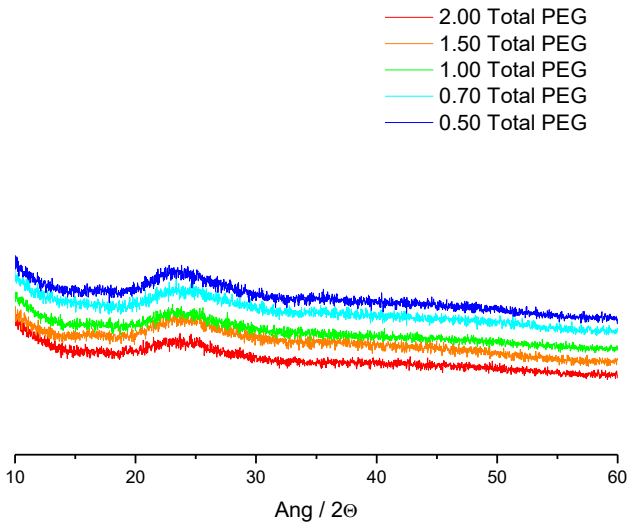

Figure 2.25 *PXRD measurements for the synthesised nanoparticles.*

For all the PXRD measurements, only one broad peak is observed close to 12 θ. This was expected, as PXRD line broadening is usually observed in nanoparticle samples.[92] In spite of the broadening, if the only contribution to this effect was the reduced size of the particles, methods like the Scherrer method could be employed in order to study the size of the particles. In this case, however, the presence of PEG in the samples is also contributing to the line broadening effect and, thus, it is not possible to make any sensible quantitative treatment of the data.

Finally, UV-Vis spectra were recorded in chloroform dispersions for all the samples, including the crystalline sample obtained previously[88] and can be observed in **Figure 2.26**.

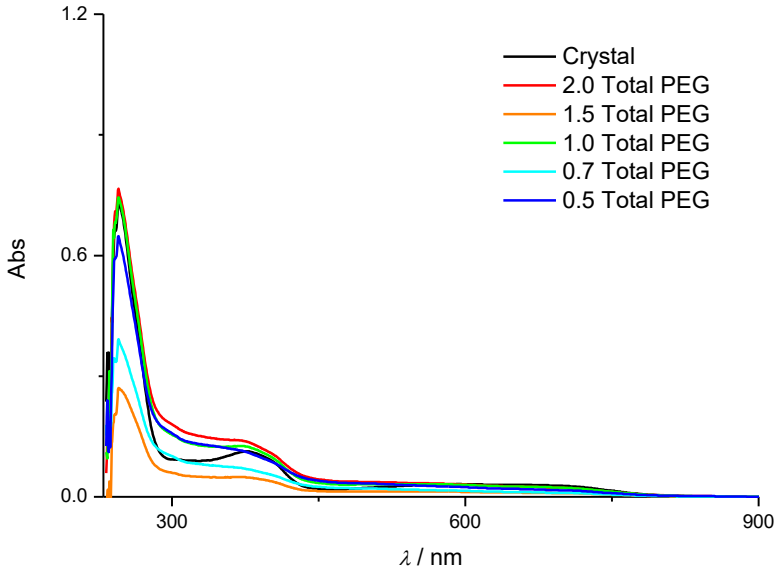

Figure 2.26 *UV-Vis spectra for the synthesised nanoparticles and for the same compound from a crystalline sample.*

The spectrum obtained for the chloroform solution of the bulk sample contains three bands that are characterised in **Table 2.10**.

Table 2.10 *UV-Vis data analysed from the spectrum obtained for the crystal solution, in a concentration of $1x10^{-5}$ M.*

Wavelength / nm	*Abs*	*ε / M^{-1} cm^{-1}*
246	0.729	72900
376	0.113	11300
594	0.032	3200

The bands at 246 and 376 nm should be attributed to charge-transfer between the ligands and the iron, or vice-versa. The band at 594 nm is typically observed in the spectra of compounds with Fe^{III} centres in the high-spin state. Neither of the bands correspond to *d-d* transitions, as their molar absorption coefficients are much higher than those expected for *d-d* transitions (1-100 M^{-1} cm^{-1}).

All the nanoparticle dispersions exhibited the exact same bands as the solution of the compound in crystal form, providing further evidence that the desired transition metal compound was synthesised in the polymeric matrix. The varying Abs values were recorded probably due to the error in the mass determination of the nanoparticles during the dispersion preparation, since a very small mass of sample had to be used in each dispersion.

2.4.2 Nanorods

Nanorods of **NP** were also obtained, although through a different synthesis procedure. A solution of **NP** with controlled concentration was prepared and a small droplet was transferred onto a microscope glass slide and covered. Constant pressure was applied while the solvent evaporated in air and the nanorods were found on the glass coverslip, after 48 hours (**Scheme 2.8**).

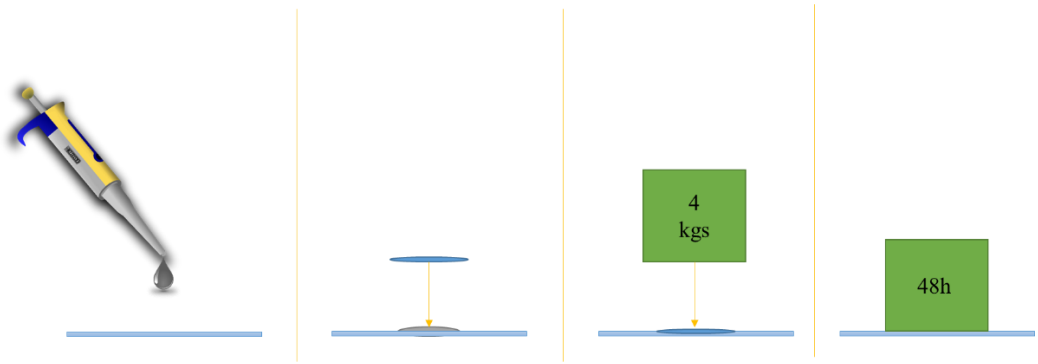

Scheme 2.8 *Method used to promote the assembly of nano-rods.*

AFM imaging of the coverslips can be observed in **Figure 2.27**.

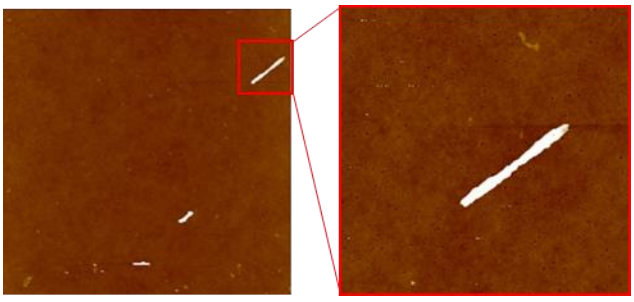

Figure 2.27 *AFM images of the nanorods obtained. The sizes of the windows are 10.0 μm (left) and 1.1 μm (right). The rod which is augmented has a length of 1.5 μm and a width of 92.0 nm.*

These nanorods are to be characterised by Raman Spectroscopy in order to determine their magnetic response to temperature.

2.4.3 Gold nanoparticles

Homogeneously dispersed citrate-stabilised gold nanoparticles were synthesised following a published method,[93] in order to functionalise them with spin crossover molecules through sulphur bridges. The SCO candidate chosen for this coupling was a system based on those Schiff-base ligands previously described, but with a thiol substitution in the phenolate rings, in order to provide a covalent way to bind the SCO candidate to the gold particles (S-Au bond, **Scheme 2.9**).

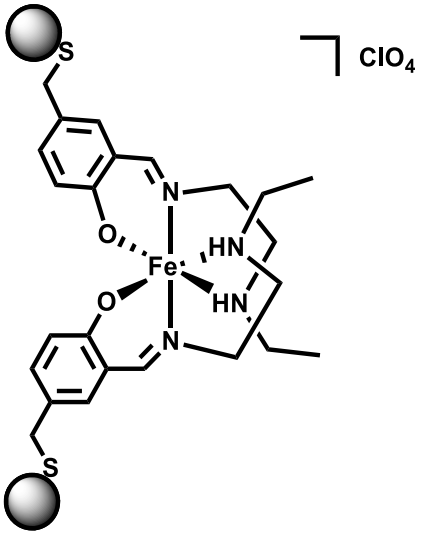

Scheme 2.9 *Gold nanoparticles capped with the SCO candidate.*

The synthesis of this candidate involved 3 steps: synthesis of the ligand with a methylchloride substituent; synthesis of the respective Fe^{III} complex; substitution of the chloride atom for a thiol functional group. This resulted in a black-coloured polymer, which was insoluble in regular laboratory solvents.

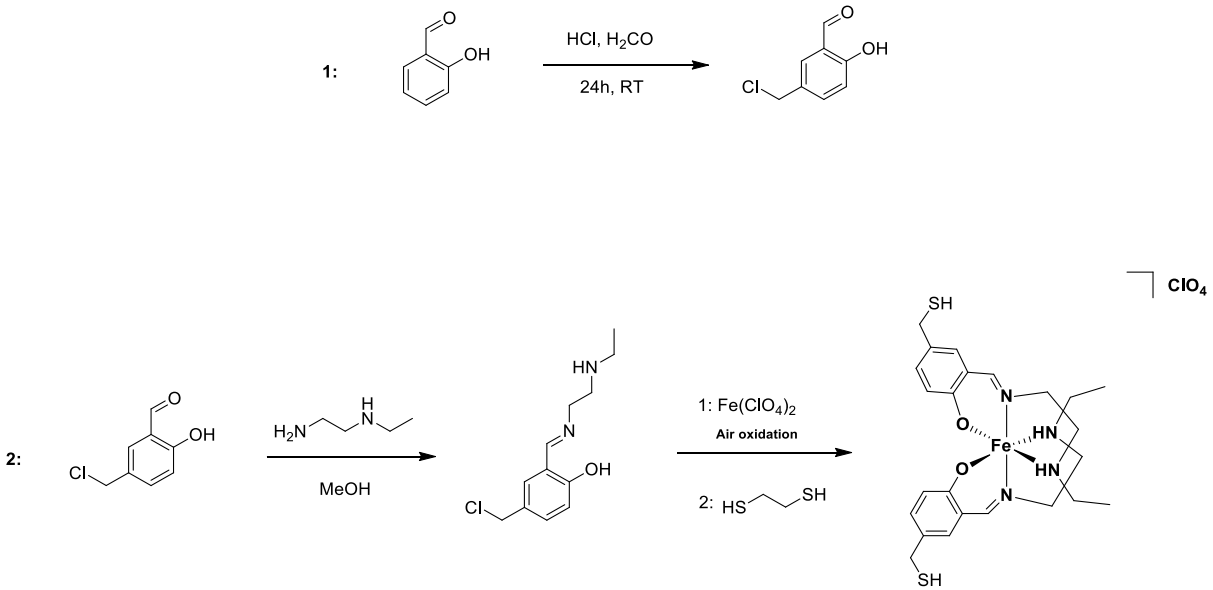

Scheme 2.10 *Reaction scheme for the synthesis of the SCO candidate to be bound to gold nanoparticles.*

The previously synthesised gold nanoparticles (8.5 nm) were then incubated in a reactor for 72h, at 373 K, along with a controlled amount of the SCO candidate. The resulting dispersion changed in colour from red to yellow.

AFM was employed in order to determine if the capping of the particle yielded any difference.

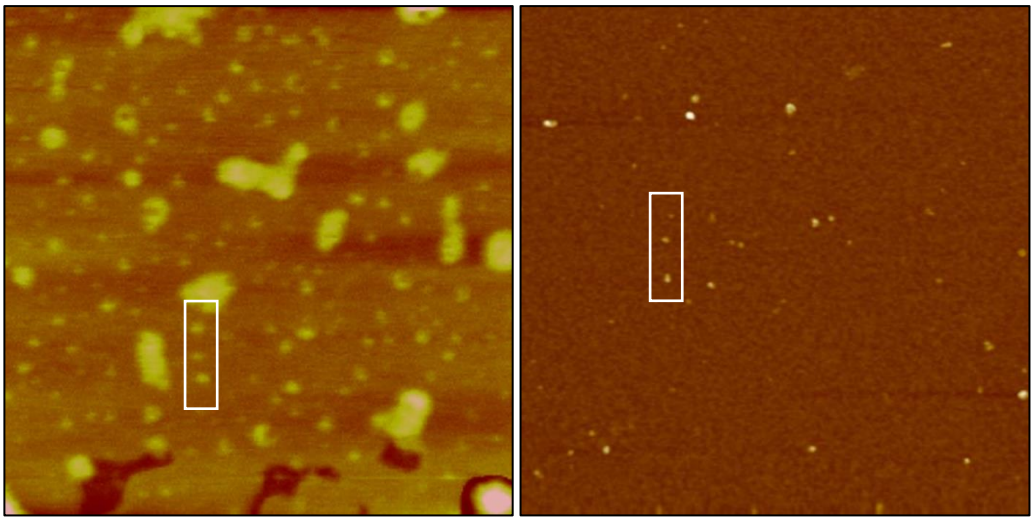

Figure 2.28 *AFM image of the synthesised gold nanoparticles (left) and of the particles obtained after capping (right). The particles outlined were used to calculate the size. Window sizes: 1.2x1.2 μm and 1.1x1.1 μm.*

Indeed, a clear difference was noted between both images. While the gold nanoparticle dispersion yielded a heterogeneous sample of particles with sizes ranging from 24 nm to 33 nm, the possibly capped particles exhibited a much more homogeneous dispersion with 22 nm. These results suggest that the capping was successful as there was some modification on the particles that prevented its aggregation. This hypothesis should be confirmed in the future by Scanning Electron Microscopy / Transmission Electron Microscopy (SEM/TEM) studies.

The UV-vis spectra of both dispersions of capped and uncapped gold particles were traced for comparison. The results are presented in **Figure 2.29**.

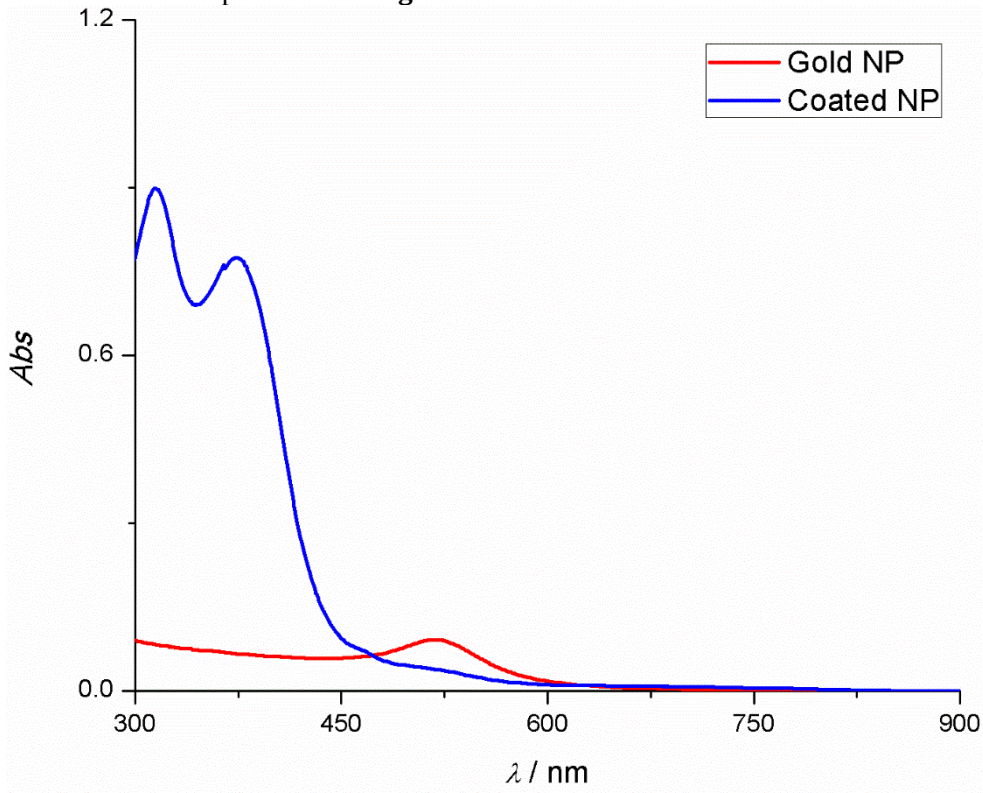

Figure 2.29 *UV-vis spectra for the gold-based Nano-particles.*

The data collected from the UV-vis spectra is recorded in **Table 2.11**.

Table 2.11 *UV-vis spectra data for Gold NP and Coated NP.*

	λ / nm	**Abs**
Gold NP	518	0.092
Coated	315	0.899
NP	374	0.775

The sole band that is observed for the gold nanoparticle solution at 518 nm is according to the literature and confirms the synthesis of these particles, in spite of their size. In the case of the capped nanoparticles, the band attributed to gold is no longer recorded in the spectrum and two other bands at wavelengths consistent with metal-ligand or ligand-metal charge transfer are observed. This fact provides further proof that the gold nanoparticles were actually coated with a transition metal compound.

2.5 Thermal analysis

The results presented in section 2.5 were obtained during a Short Term Scientific Mission (COST Action CM1305 – ECOSTBio) of mine to the research group of Prof Yann Garcia, at the Institute of Condensed Matter and Nanosciences (ICMN/MOST), Université Catholique de Louvain, Belgium. The compounds were synthesised by Dr Ana I. Vicente and Dr Paulo N. Martinho, except for TA4 which was synthesised by me.

DSC measurements were conducted on previously synthesised spin crossover compounds that exhibited abrupt spin transitions, so that this phenomenon would be greater understood.

2.5.1 Silicon modified Schiff-base Fe^{III} complexes

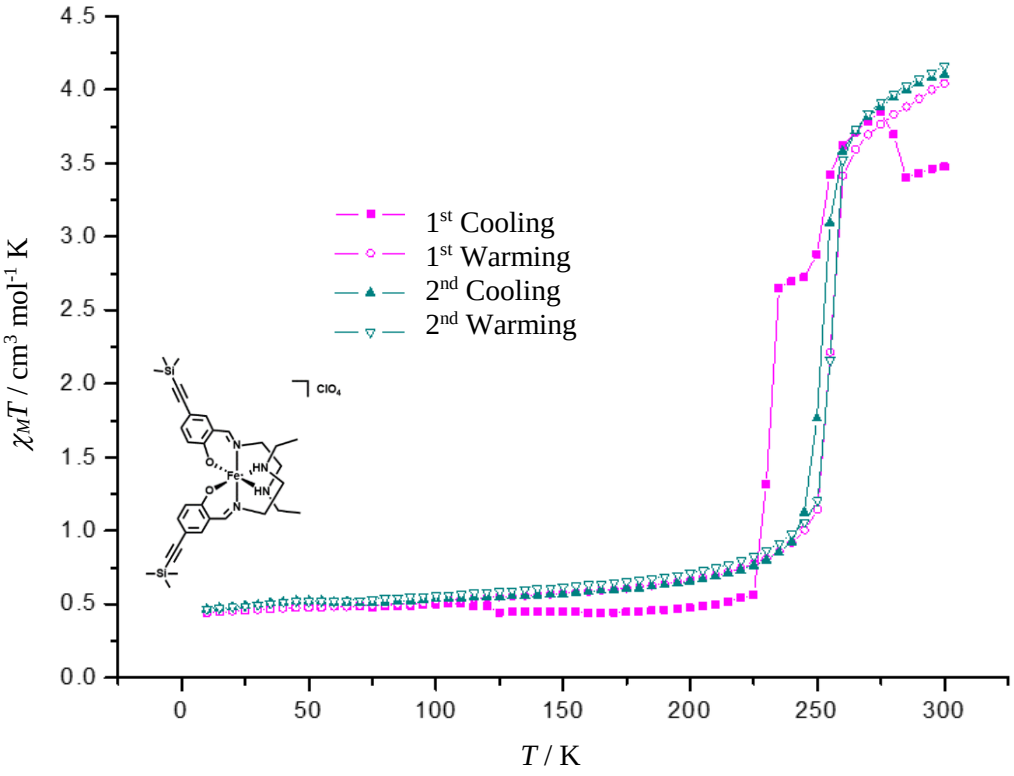

Figure 2.30 *$\chi_M T$ vs T plot for* ***TA1****.*

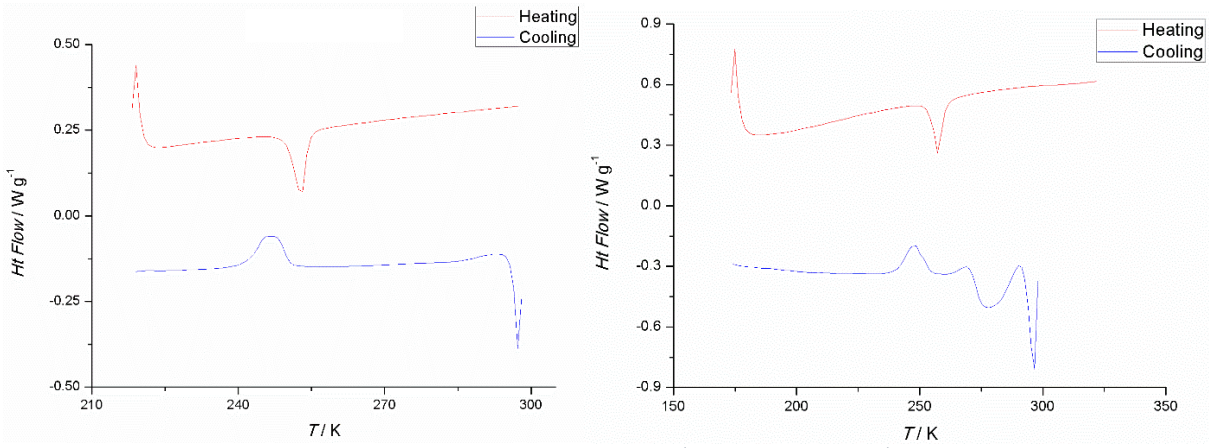

Figure 2.31 *DSC curves for* ***TA1*** *at 5 K min^{-1} (left) and 10 K min^{-1} (right).*

Upon cooling to 173 K from 273 K, a wide endothermic peak is observed around 248 K (19.08 mJ). Although the measurement at 10 K min^{-1} suggests there may be two adjacent peaks, a single wide peak is observed when the scan rate is reduced to 5 K min^{-1}. Subsequent heating to 323 K revealed an

exothermic peak at 258 K (-18.24 mJ). These results are in agreement with the magnetic profile for the compound, since the peaks coincide with the temperatures at which the spin transitions occurs, both on the cooling and the heating segments, and a small magnetic hysteresis (10 K) is observed in both measurements.

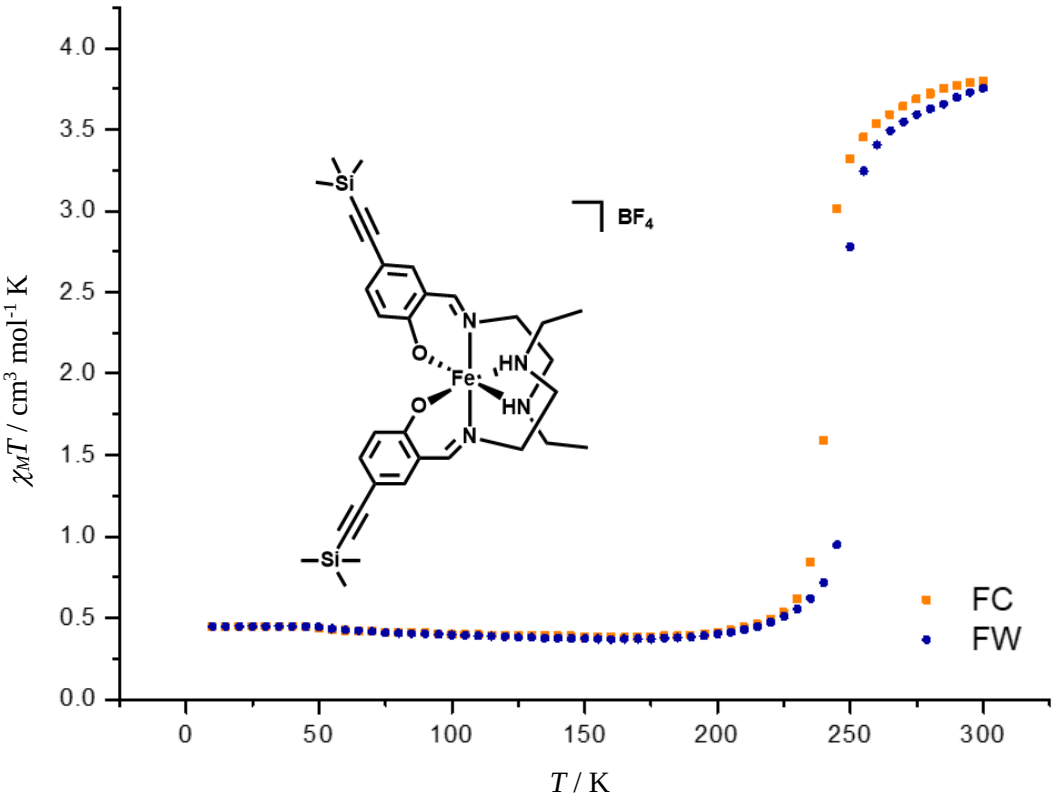

Figure 2.32 $\chi_M T$ *vs T plot for* ***TA2****.*

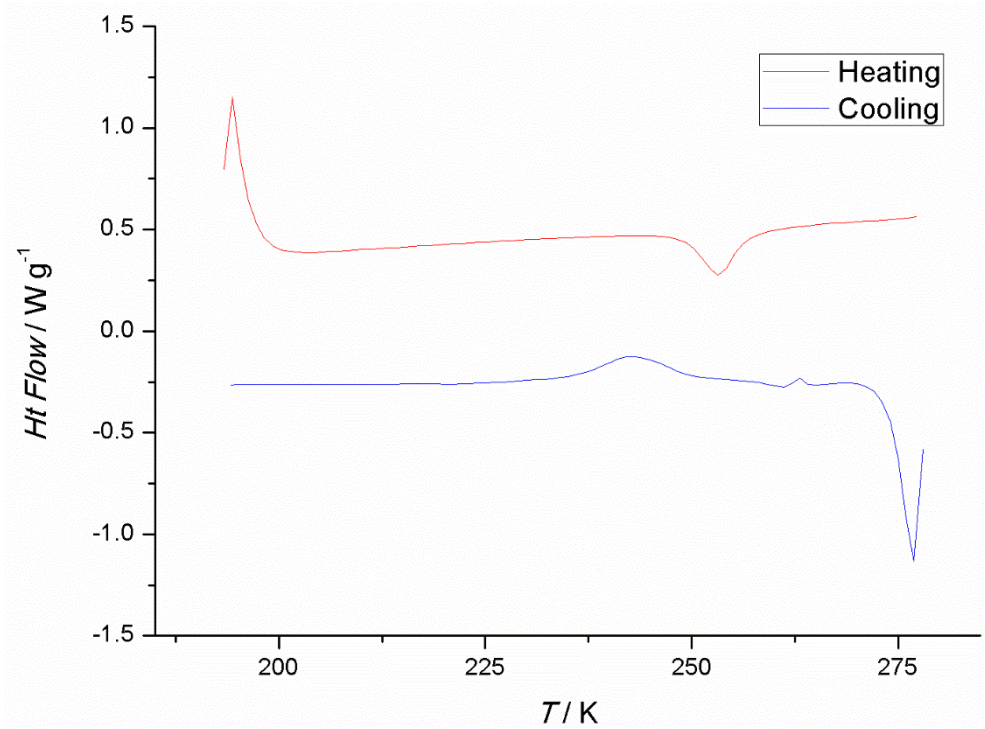

Figure 2.33 DSC curve for ***TA2*** *at 10 K min*$^{-1}$*.*

Upon cooling from 273 K to 173 K, a small endothermic peak was identified at 263 K (0.39 mJ) which may be attributed to possibly a rotation of the phenyl rings. Another wide endothermic peak was observed at 242 K (13.28 mJ). Subsequent heating to 278 K showed an exothermic peak around 253 K (-13.66 mJ). The large peaks are in agreement with the spin transitions observed in the magnetic measurements. The small hysteresis (9 K wide) is also in agreement with the SQUID magnetometry results.

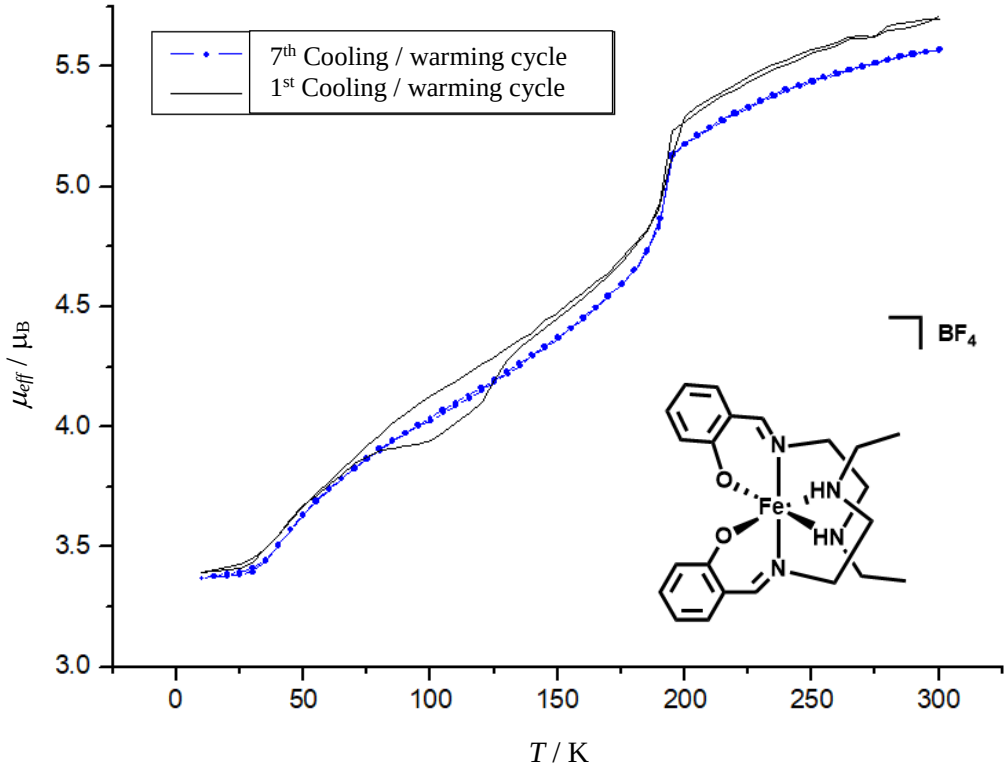

Figure 2.34 *$\chi_M T$ vs T plot for* ***TA3****.*

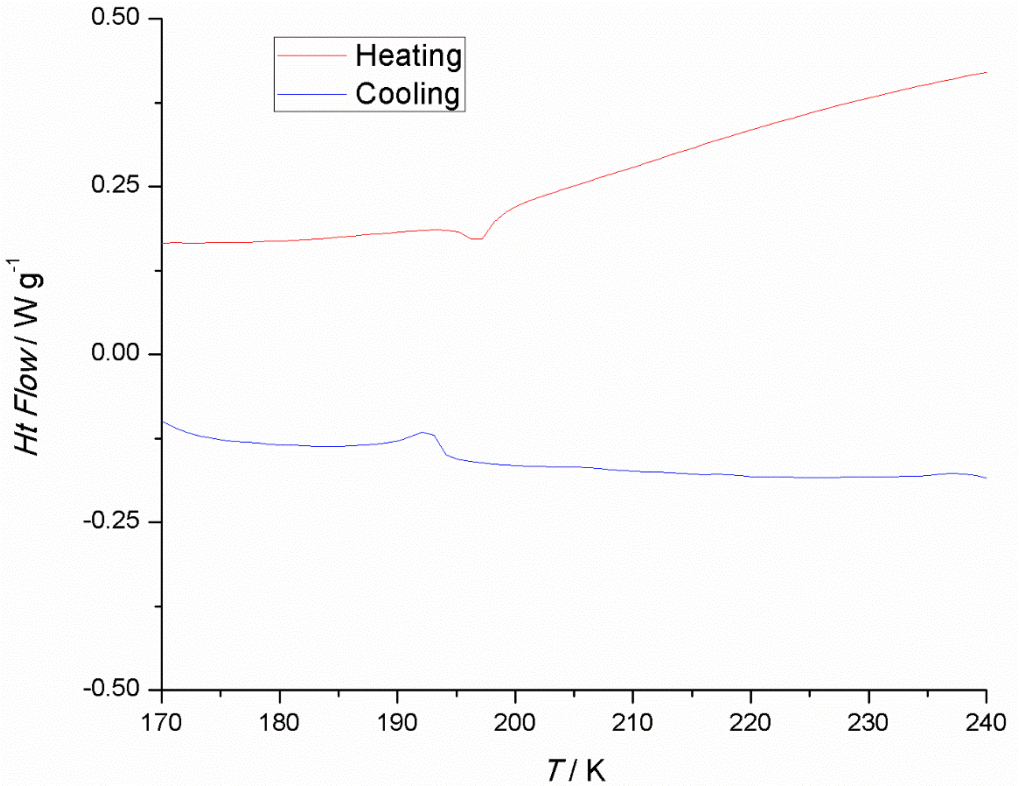

Figure 2.35 *DSC curve for* ***TA3*** *at 10 K min^{-1}.*

Upon cooling from 240 K to 170 K, a small thermal anomaly was identified at 194 K (0.60 J g^{-1}) which seems to correspond to the small and abrupt spin transition observed in the magnetic data. Subsequent heating to 240 K showed another thermal anomaly around 197 K (-0.65 J g^{-1}). The remaining gradual spin transition is not observed in the DSC curve.

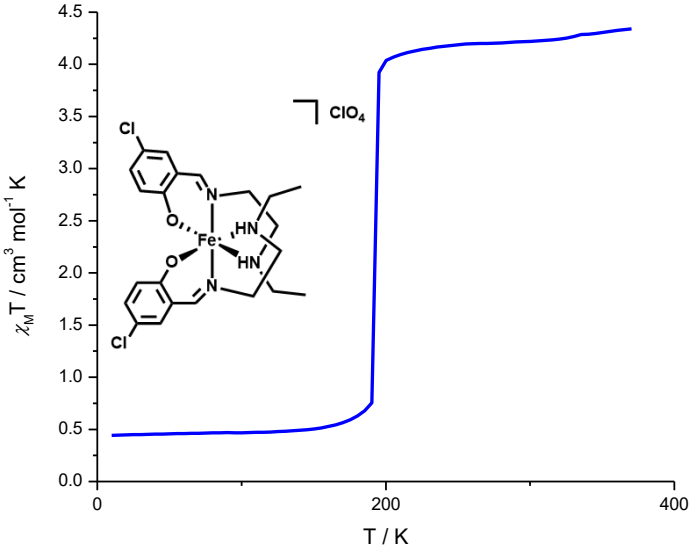

Figure 2.36 *$\chi_M T$ vs T plot for* ***TA4****.*

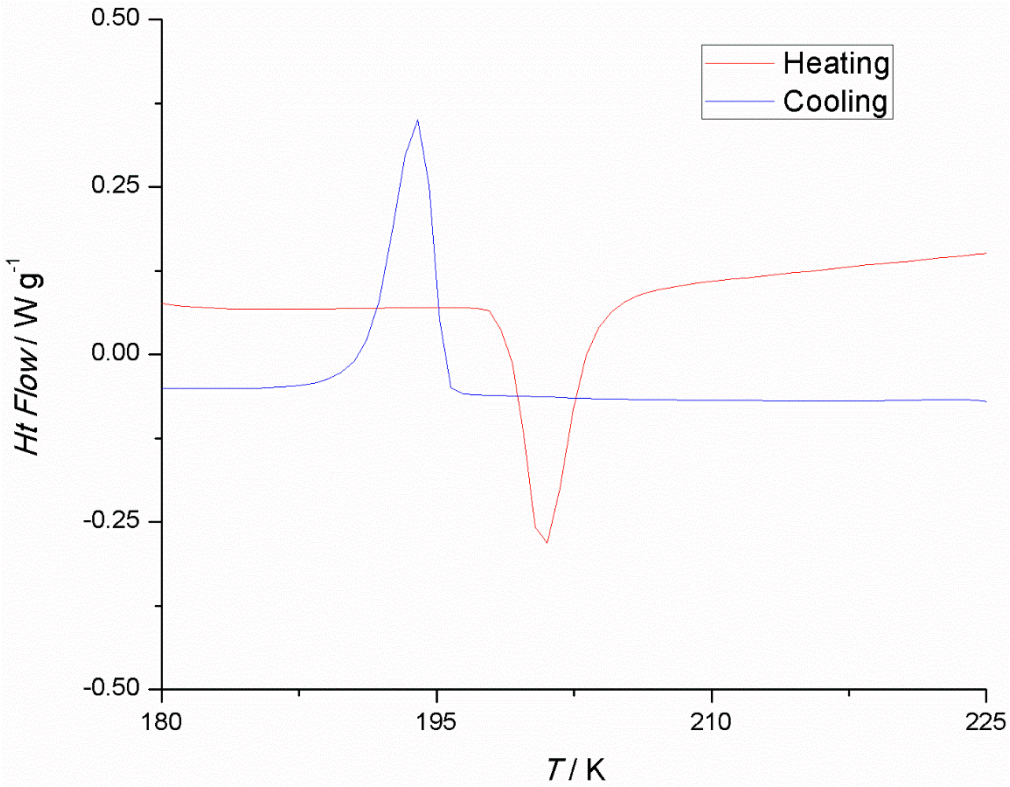

Figure 2.37 *DSC curve for* ***TA4*** *at 10 K min^{-1}.*

Upon cooling from 225 K to 180 K, a large endothermic peak was identified at 194 K (41.52 mJ) which clearly corresponds to the spin transition and is in complete agreement with the magnetic data. Subsequent heating to 225 K showed a large exothermic peak around 200 K (-39.89 mJ). The large peaks are in agreement with the spin transitions observed in the magnetic measurements. The small hysteresis (6 K wide) was not observed in the magnetic profile.

3 Conclusions

In the present thesis, as was proposed, several iron compounds and architectures with spin crossover potential were synthesised, although there is some work yet to be fulfilled.

In total, eight crystals were obtained from mononuclear compounds. Two crystals were obtained from the combination of known cations to the group and the tetrafluoroborate anion and their magnetic profiles was analysed. Both compounds are found in the LS state at low temperatures and exhibit gradual and incomplete spin transitions. The trend that is reported in the literature, relating the halogen size and $T_{1/2}$, is also verified in these compounds. However, it was not confirmed by the DFT calculations, suggesting that intermolecular interactions are to be behind this phenomenon. In the future, the crystal with an iodine substituent in the phenolic rings should be obtained and the crystals should be further characterised by Mössbauer spectroscopy and SCXRD.

Five crystals were obtained from the combination of known cations to the group and the tetraphenylborate anion in different solvents and their magnetic profiles were analysed. The two crystals obtained in DMF were found in the LS state and exhibited gradual and incomplete transitions, with the chlorine substituted compound exhibiting much higher $T_{1/2}$. The Mössbauer spectrum obtained for the latter is in agreement with the SQUID magnetometry results and suggests that there is a population of two different isomers at room temperature in these crystals. The crystal obtained in methanol exhibited a complicated spin crossover behaviour, with gradual and abrupt steps and stabilises in the HS state upon solvent evaporation. The crystals obtained in acetonitrile both exhibited gradual spin transitions and the chlorine substituted compounds seems to contain solvent molecules in its structure since the compound stabilises in the HS state upon warming to 370 K. The $T_{1/2}$ was higher for the compounds with larger halogens, in general, as was confirmed by DFT calculations. In the future, all these crystals should be analysed by Thermogravimetric analysis, in order to determine if and which solvent may be incorporated in their structures and the crystallisation conditions should all be tuned in order to get crystals without any solvent. Also, the crystals should be characterised by Mössbauer spectroscopy and SCXRD.

A crystal obtained from a compound with an analogous hexadentate ligand was also obtained. The magnetic studies showed that the compound stabilises in the LS state, suggesting that the added rigidity of the ligand does not allow for the spin crossover phenomenon. In the future, the crystal should be characterised by SCXRD and Mössbauer spectroscopy.

Four binuclear compounds were also obtained and characterised. All four exhibited a constant $\chi_M T$ value throughout the magnetic analysis and antiferromagnetic coupling between the iron centres at low temperatures. DFT calculations provided structures in the HS state at room temperature and confirmed the antiferromagnetic coupling that was observed by SQUID magnetometry. This coupling has a lesser extent in the compound with symmetric ligands, as expected. In the future, SCXRD should be obtained for the remaining three compounds and Mössbauer spectra should be obtained for them all.

A powder with FT-IR and colour consistent with the proposed cage was also obtained. SQUID magnetometry showed an almost constant $\chi_M T$ value throughout the experiment and antiferromagnetic coupling between the iron centres at low temperatures. In the future, a crystal should be obtained from this powder and should be characterised by SCXRD, as well as Mössbauer spectroscopy. Anion incorporation studies by NMR titration are also to be conducted, in order to study the supramolecular capabilities of the supposed cage.

Nano-sized particles were obtained of a SCO transition metal compound in polymeric matrix. Their size is dependent on the amount of polymer added during the synthesis, however there is not a proportionality relationship, apparently. AFM imaging showed rather homogeneous dispersions of spheres with sizes ranging from 10 nm and 27 nm, however these values are likely to correspond to

aggregates and the actual particles are much smaller. NANO-sizer measurements on dispersions of the two samples synthesised with the least amount of polymer registered sizes of 1.75 nm and 2.16 nm. These latter results should describe the sizes of the actual particles with greater accuracy. SQUID magnetometry showed some SCO behaviour in every sample, however the transitions are very gradual and incomplete, which suggests that there is very low cooperativity between the iron centres and is in agreement with what is expected for nano-particle dispersions. The curve obtained by PXRD is consistent with the existence of nano-sized structures and UV-Vis spectroscopy confirmed the presence of the desired transition metal compound. In the future, these nano-particles should be characterised by SEM and TEM in order to correctly determine their size and morphology.

Nano-rods of the same compound were also obtained through a pressure method. The nano-rods were self-assembled in a cover-slip and later observed through AFM imaging. In the future, these nano-structures are to be characterised by Raman spectroscopy, in order to determine their magnetic behaviour.

Gold nano-particles were obtained from a published synthesis and apparently capped with a transition metal compound, through a Sulphur-Gold bond. A capping procedure was performed inside a reactor for 72h. AFM imaging suggest that the modification of the gold nano-particles prevented particle aggregation and resulted in a more homogeneous dispersion. UV-Vis spectroscopy also confirmed a modification on the nano-particles and some seemingly charge transfer bands may be observed. In the future, the magnetic behaviour of these particles should be determined and they should be characterised by SEM and TEM.

Finally, Differential Scanning Calorimetry was employed in previously synthesised SCO compounds, during a STSM by the MSc candidate. While the abrupt spin transitions were easily characterised by DSC, this was not the case for the gradual SCO.

4 Experimental

4.1 Synthesis

All reactants and solvents were purchased either from Sigma-Aldrich or Acros and used without further purification. The Elemental Analyses were conducted at Universidade de Vigo. Some values are not within acceptable range, which suggests that the crystalline samples that were used for pyrolysis were contaminated with powder.

Synthesis of [Fe(5-F-salEen)$_2$]BF$_4$. N-ethylethylenediamine (0.50 mmol) was added to a methanol solution (20 ml) of 5-fluorosalicylaldehyde (0.50 mmol) and stirred for 30 minutes. A methanol solution (20 ml) of iron(II) chloride (0.25 mmol) and sodium tetrafluoroborate (0.25 mmol) was filtered to the previously prepared solution, which was stirred for another 30 minutes, affording the [Fe(5-F-salEen)$_2$]BF$_4$ complex upon air oxidation. Black needle-shaped crystals were obtained after solvent evaporation at 313.15 K and recovered via filtration. Yield: 33%. Elemental analysis calculated (%) for $C_{22}H_{28}BF_6FeN_4O_2$: C 47.09, H 5.03, N 9.98; found: C 48.40, H 4.78, N 9.92. FTIR: ν=1068 cm^{-1} (BF_4^-, s), ν=1468 cm^{-1} (BF_4^-, s), ν=1633 cm^{-1} (C=N, s).

Synthesis of [Fe(5-Cl-salEen)$_2$]BF$_4$. N-ethylethylenediamine (0.50 mmol) was added to a methanol solution (20 ml) of 5-chlorosalicylaldehyde (0.50 mmol) and stirred for 30 minutes. A methanol solution (20 ml) of iron(II) chloride (0.25 mmol) and sodium tetrafluoroborate (0.25 mmol) was filtered to the previously prepared solution, which was stirred for another 30 minutes, affording the [Fe(5-Cl-salEen)$_2$]BF$_4$ complex upon air oxidation. Black needle-shaped crystals were obtained after solvent evaporation at 313.15 K and recovered via filtration. Yield: 33%. Elemental analysis calculated (%) for $C_{22}H_{28}BCl_2F_4FeN_4O_2$: C 44.48, H 4.75, N 9.43; found: C 39.83, H 4.05, N 7.95. FTIR: ν=1069 cm^{-1} (BF_4^-, s), ν=1456 cm^{-1} (BF_4^-, s), ν=1631 cm^{-1} (C=N, s).

Synthesis of [Fe(5-I-salEen)$_2$]BF$_4$. N-ethylethylenediamine (0.50 mmol) was added to a methanol solution (20 ml) of 5-iodosalicylaldehyde (0.50 mmol) and stirred for 30 minutes. A methanol solution (20 ml) of iron(II) chloride (0.25 mmol) and sodium tetrafluoroborate (0.25 mmol) was filtered to the previously prepared solution, which was stirred for another 30 minutes. It was not possible to grow any crystals or powder from this solution.

Synthesis of [Fe(5-F-salEen)$_2$]BPh$_4$. N-ethylethylenediamine (0.50 mmol) was added to a dimethylformamide/acetonitrile solution (20 ml) of 5-fluorosalicylaldehyde (0.50 mmol) and stirred for 30 minutes. A dimethylformamide/acetonitrile solution (20 ml) of iron(II) chloride (0.25 mmol) and sodium tetraphenylborate (0.25 mmol) was filtered to the previously prepared solution, which was stirred for another 30 minutes, affording the [Fe(5-F-salEen)$_2$]BPh$_4$ complex upon air oxidation. Black needle-shaped crystals were obtained after solvent evaporation at 313.15 K and recovered via filtration. Yield: 24%. Elemental analysis calculated (%) for $C_{46}H_{48}BF_2FeN_4O_2$: C 69.62, H 6.10, N 7.06; found: C 67.20, H 5.95, N 6.85. FTIR: ν=1624 cm^{-1} (C=N, s), ν=732 cm^{-1} (BPh_4^-, s), ν=707 cm^{-1} (BPh_4^-, s).

Synthesis of [Fe(5-Cl-salEen)$_2$]BPh$_4$. N-ethylethylenediamine (0.50 mmol) was added to a dimethylformamide/acetonitrile solution (20 ml) of 5-chlorosalicylaldehyde (0.50 mmol) and stirred for 30 minutes. A dimethylformamide/acetonitrile solution (20 ml) of iron(II) chloride (0.25 mmol) and sodium tetraphenylborate (0.25 mmol) was filtered to the previously prepared solution, which was stirred for another 30 minutes, affording the [Fe(5-Cl-salEen)$_2$]BPh$_4$ complex upon air oxidation. Black needle-shaped crystals were obtained after solvent evaporation at 313.15 K and recovered via filtration. Yield: 47%. Elemental analysis calculated (%) for $C_{46}H_{48}BCl_2FeN_4O_2$: C 66.85, H 5.85, N 6.78; found: C 65.67, H 5.87, N 7.49. FTIR: ν=1658 cm^{-1} (C=N, s), ν=730 cm^{-1} (BPh_4^-, s), ν=706 cm^{-1} (BPh_4^-, s).

Synthesis of [Fe(5-I-salEen)$_2$]BPh$_4$. N-ethylethylenediamine (0.50 mmol) was added to a methanol solution (20 ml) of 5-iodosalicylaldehyde (0.50 mmol) and stirred for 30 minutes. A methanol solution (20 ml) of iron(II) chloride (0.25 mmol) and sodium tetraphenylborate (0.25 mmol) was filtered to the previously prepared solution, which was stirred for another 30 minutes, affording the [Fe(5-I-salEen)$_2$]BPh$_4$ complex upon air oxidation. Black needle-shaped crystals were obtained after solvent evaporation at 313.15 K and recovered via filtration. Yield: 20-30%. Elemental analysis calculated (%) for $C_{46}H_{48}BI_2FeN_4O_2$: C 54.74, H 4.79, N 5.55; found: C 52.97, H 4.79, N 5.41. FTIR: ν=1653 cm^{-1} (C=N, s), ν=731 cm^{-1} (BPh_4^-, s), ν=705 cm^{-1} (BPh_4^-, s).
Synthesis of [Fe(5-I-triEen)]ClO$_4$. Triethylenetetramine (0.50 mmol) was added to a methanol solution (20 ml) of 5-iodosalicylaldehyde (0.50 mmol) and stirred for 30 minutes. A methanol solution (20 ml) of iron(II) chloride (0.25 mmol) and sodium perchlorate (0.25 mmol) was filtered to the previously prepared solution, which was stirred for another 30 minutes, affording the [Fe(5-I-triEen)]ClO$_4$ complex upon air oxidation. Black needle-shaped crystals were obtained after solvent evaporation at 313.15 K and recovered via filtration. Yield: 49%. Elemental analysis calculated (%) for $C_{23}H_{30}ClFeI_2N_4O_6$: C 34.38, H 3.76, N 6.97. FTIR: ν=1626 cm^{-1} (C=N, s), ν=1090 cm^{-1} (ClO_4^-, s), ν=628 cm^{-1} (ClO_4^-, s).

Synthesis of the Fe^{II} cages. 2-Pyridinecarboxaldehyde (0.91 ml) was added to a dry acetonitrile solution (10 ml) of 4,4-Methylene-bis(2-chloroaniline) (0.46 mmol) under N_2 atmosphere. One drop of hydrogen chloride was added and the solution was stirred for 30 minutes. Afterwards, iron(II) trifluoromethanesulfonate (0.30 mmol) was added and the reaction mixture was stirred for 48 hours at 323 K. The final purple powder was obtained by precipitation after the addition of diisopropyl ether. Yield: 32%. FTIR: ν=1630 cm^{-1} (C=N, s), ν=1030 cm^{-1} ($CF_3SO_3^-$, s).

Synthesis of [Fe(5-I-salEen)$_2$]ClO$_4$ particles. N-ethylethylenediamine (0.04 ml, 0.4 mmol) was added to a methanol solution (13 ml) of 5-iodosalicylaldehyde (99.0 mg, 0.4 mmol) and stirred for 30 minutes. Iron(II) perchlorate hydrate(75.0 mg, 0.2 mmol) was dissolved in Millipore water (17 ml) and the same desired amount of polyethylene glycol was added to both solutions. After 10 minutes of stirring, the PEG/Fe solution was added dropwise to the PEG/ligand solution. The final black dispersion was stirred for 4 hours after which it was filtered and the particles were washed with Millipore water and methanol.
Synthesis of the Nano-rods. [Fe(5-I-salEen)$_2$]ClO$_4$ crystals, obtained as previously published,[88] were dissolved in a mixture of ethanol and acetonitrile, yielding a solution with a concentration of 1.5x10^{-3} M. A 20 μl drop of this solution was then transferred to a glass microscope slide and covered with a glass cover slip. Constant pressure was applied for 48 hours. The Nano-rods were formed on the surface of the cover slips as the solvent evaporated.

Synthesis of the gold nanoparticles. An aqueous solution (20 ml) containing 4 ml 1% (w/v) trisodium citrate and 0.08 mL 1% tannic acid was prepared. Afterwards, a second aqueous solution containing 1 ml 1% (w/v) chloroauric acid in 80 ml Millipore water was prepared. Both solutions were heated up to 333 K for 2 minutes. Then the reducing solution was quickly added to the gold solution and the resulting mixture is refluxed. After 10 minutes, the colloidal dispersion was cooled to room temperature and stored in a refrigerator. A red charge-stabilized colloidal dispersion (~100 mL) of spherical gold nanoparticles (~1012 particles/mL) was thus obtained in water.[94]
Synthesis of 5-Chloromethyl-salicylaldehyde. The synthesis of 5-Chloromethyl-salicylaldehyde followed a previously published procedure,[95] although in smaller quantity. Salicylaldehyde (5 ml, 47.13 mmol) was added to a stirred solution containing concentrated hydrochloric acid (50 ml) and formaldehyde 37 wt % in H_2O (3.6 ml) and the resulting mixture was stirred for 24 hours at room

temperature. The precipitate was filtered, dissolved in diethyl ether and, finally, evaporated. Recrystallization from n-hexane yielded the desired product.

Synthesis of the capped gold nanoparticles. N-ethylethylenediamine (88.0 mg, 1.0 mmol) was added to a methanol (20 ml) solution of the freshly synthesised 5-Chloromethyl-salicylaldehyde (171.0 mg, 1.0 mmol) and the mixture was stirred for 30 minutes. Iron(II) perchlorate (160.0 mg, 0.5 mmol) was dissolved in methanol (20 ml) and the resulting solution was filtered to that containing the ligand. After another 30 minutes of stirring, 2-ethanedithiol (94.0 mg, 1.0 mmol) was added and the mixture was left stirring at room temperature for 72 hours. A black powder precipitated and was recovered and washed with methanol. Finally, 28.0 mg of this compound were added to a reactor, as well as 25 ml of the gold nanoparticle aqueous suspension and the reactor was heated to 373 K for 48 hours. A yellow solution resulted from the previously red solution.

4.2 Characterisation

Fourier-transform infrared spectroscopy. Infrared spectra were obtained from KBr pellets using a Nicolet FTIR with 1 cm^{-1} resolution, between 400 cm^{-1} and 4000 cm^{-1}.

Magnetic measurements. Magnetisation measurements as a function of temperature were performed using a SQUID magnetometer (Quantum Design MPMS). The curves were obtained at 1000 Oe for temperatures ranging between 10 and 370 K, on cooling and heating modes, using a 5 K min^{-1} scan rate, unless otherwise specified. Settle mode was used for all temperatures stabilisation. The collected data were corrected for diamagnetic contributions. The Mössbauer measurements were performed on a device equipped with a ^{57}Co radioactive source as 14.4 keV gamma rays provider, a proportional counter which detected the gamma rays passing through the sample, and a multichannel analyzer (CMCA-550) which kept the data counts and transferred data to the computer.
To perform a measurement, the source was moved in a triangular waveform with a Doppler velocity from -4.0 mm s^{-1} to 4.0 mm s^{-1} generated by Mössbauer drive unit (MR-260A). The sample was kept stationary between the source and the detector. The spectrum was recorded using Wissoft 2003 software and fitted in Recoil software using Lorentzian site analysis method. The isomer shifts (δ) of the samples are in with reference of isomer shift (δ) of metallic α-Fe.

Structural characterisation. Crystals suitable for single-crystal X-ray analysis were grown as described in the synthetic procedure. Selected crystals were covered with Fomblin (polyfluoroether oil) and mounted on a nylon loop. The data was collected at 296 K on a Bruker D8 Venture diffractometer equipped with a Photon 100 detector and an Oxford Cryostem Cooler, using graphite monochromated Mo-Kα radiation (λ = 0.71073 Å). The data was processed using the APEX3 suite software package, which includes integration and scaling (SAINT), absorption corrections (SADABS) and space group determination (XPREP). Structure solution and refinement were done using direct methods with the programs SHELXS-14 inbuilt in APEX and WinGX-Version 2014.1[96] software packages. All non-hydrogen atoms were refined anisotropically and the hydrogen atoms were inserted in idealized positions and allowed to refine riding on the parent carbon atom. Amine hydrogen atoms were located in difference Fourier peak and refined isotropically. The molecular diagrams were drawn with Mercury,[97] included in the software package.

DFT calculations. Density Functional Theory calculations[54] were performed using the Amsterdam Density Functional program package (ADF).[98–100] Gradient corrected geometry optimizations, without symmetry constraints, were performed for the mononuclear compounds using the Local Density Approximation of the correlation energy (Vosko-Wilk-Nusair),[101] and the Generalized Gradient Approximation (B3LYP* exchange and correlation functional).[102,103] Relativistic effects were treated with the ZORA approximation.[104] Unrestricted calculations were performed for S = 1/2 and S = 5/2 states. The core orbitals were frozen for C, N, O, (1s) and Fe (1s-3p). Triple ζ Slater-type orbitals (STO) were used to describe the valence shells B, C, and N (2s and 2p). One polarization function was added to C, N, O, and Fe (single ζ, 3d, 4f). Triple ζ Slater-type orbitals (STO) were used to describe the valence shells of H (1s) augmented with one polarization function (single ζ 2s, 2p).[105] In order to calculate the isotropic interaction parameters, gradient corrected geometry optimizations, without symmetry constraints, were performed using the Local Density Approximation of the correlation energy (Vosko-Wilk-Nusair),[101] and the Generalized Gradient Approximation (B3LYP* exchange and correlation functional).[102,103] Relativistic effects were treated with the ZORA approximation.[104] Unrestricted calculations were performed for the S = 5 state. Triple ζ Slater-type orbitals (STO) were used to describe the valence shells B, C, and N (2s and 2p). One polarization function was added to C, N, O, and Fe (single ζ, 3d, 4f). Triple ζ Slater-type orbitals (STO) were used to describe the valence shells of H (1s) augmented with one polarization function (single ζ 2s, 2p).[105] Finally, Unrestricted calculations were performed for the S = 0 state according to the Broken Symmetry Approach.[89] The structures were modelled after the structures of the complexes obtained through single crystal X-ray crystallography for the same or similar compound. The structures were visualized with Chemcraft.[106]

Thermal analysis. The DSC studies were carried out under N_2 (g) atmosphere, on a DSC821 instrument from Mettler Toledo, equipped with a cryostat. 2-3 mg of sample were encapsulated at room temperature in a 40 μl aluminium pan, hermetically sealed and formerly pierced. The samples were subjected to an isothermal step of 1 min at the starting temperature, followed by a dynamic step until the desired temperature, at a scan rate of 5 or 10 K min^{-1}. The samples were maintained at this temperature for 2 min in order to reach equilibrium and subsequently subjected to a final dynamic step at the same scan rate. The temperature and heat flow scales of the apparatus were calibrated, at 10 K min^{-1}, over the temperature range 132-193 K with pure cyclopentane (99%, Acros, T_{trs}= 138.06 K, Q_{trs}= 4.91 J g^{-1}).[107] An empty 40 μl aluminium pan, identical to the one used as sample holder, was used as reference, to obtain a reliable baseline.

AFM imaging. A 40 μl drop of $1x10^{-5}$ M dispersions of nanoparticles was deposited on a cleaved Mica substrate purchased from Veeco and dried with pure N_2. Atomic Force Microscopy (AFM) was carried out in a Multimode 8 HR coupled to nanoscope V, produced by Bruker, using Peak Force Tapping mode under ScanAsyst Control. The images were acquired in ambient conditions, using etched silicon tips with a spring constant of ca. 0.4 N/m (SCANASYST-AIR, Bruker), at a scan rate of ca. 1 Hz.

Crystallinity assessment. Powder X-ray diffraction measurements were performed using a Philips X-ray diffractometer (PW 1730) with automatic data acquisition (APD Philips v3.6B), using Cu Kα radiation (λ = 0.15406 nm) and working at 40 kV/30 mA, in a continuous scan from 7.0080 to 59.9970 (2Θº), with each step taking 80.0100 s and widening 0.0170 (2Θº), at 298.15 K.

Particle size measuments. Particle size measurements were carried out with a NANO-flex 180º DLS Size from Particle Metrix, using $1x10^{-5}$ M dispersions.

UV-Vis spectroscopy. UV-Vis spectra were collected in a UV-1601 spectrometer from Shimadzer between 1000-200 nm.

DSC measurements. The DSC studies were carried out under N_2(g) atmosphere, on a DSC821 instrument from Mettler Toledo, equipped with a cryostat. 2-3 mg of sample were encapsulated at room temperature in a 40 μl aluminium pan, hermetically sealed and formerly pierced. The samples were subjected to an isothermal step of 1 min at the starting temperature, followed by a dynamic step until the highest temperature achieved, at a scan rate of 5 or 10 K min^{-1}. The samples were maintained at this temperature for 2 min in order to reach equilibrium and subsequently subjected to a final dynamic step at the same scan rate. The temperature and heat flow scales of the apparatus were calibrated, at 10 K min-1, over the temperature range 132-193 K with pure cyclopentane (99%, Acros, T_{trs}= 138.06 K, Q_{trs}= 4.91 J g^{-2}).[107] An empty 40 μl aluminium pan, identical to the ones used as sample holders, was used as a reference, to obtain a reliable baseline.

5 References

[1] A. D. McNaught, A. Wilkinson, M. Nic, J. Jirat, B. Kosata, A. Jenkins, *IUPAC. Compendium of Chemical Terminology (the "Gold Book")*, Blackwell Scientific Publications, Oxford, **1997**.

[2] C. E. Housecroft, A. G. Sharpe, *Inorganic Chemistry*, **2005**.

[3] P. S. Matsumoto, *J. Chem. Educ.* **2005**, *82*, 1660.

[4] L. Pauling, *Jounal Chem. Soc.* **1948**, *0*, 1461–1467.

[5] L. Pauling, *The Nature of the Chemical Bond and the Structure of Molecules and Crystals: An Introduction to Modern Structural Chemistry*, Cornell University Press, **1960**.

[6] M. C. Favas, D. L. Kepert, *J. Chem. Soc. Dalt. Trans.* **1978**, *0*, 793–797.

[7] R. J. Gillespie, *J. Chem. Educ.* **2004**, *81*, 298.

[8] E. König, S. Kremer, *Theor. Chim. Acta* **1971**, *23*, 12–20.

[9] C. J. Ballhausen, *Int. J. Quantum Chem.* **1971**, *5*, 373–377.

[10] J. J. Stephanos, A. W. Addison, in *Electron, Atoms, Mol. Inorg. Chem.*, Academic Press, **2017**, 331–401.

[11] R. L. Carlin, *Magnetochemistry*, Springer-Verlag, **1986**.

[12] P. Gütlich, H. A. Goodwin, *Top. Curr. Chem.* **2004**, *233*, 1–47.

[13] L. D. Landau, E. M. Lifshitz, in *Electrodyn. Contin. Media*, Elsevier Ltd., **1984**, 130–179.

[14] R. Boča, in *Curr. Methods Inorg. Chem.*, Elsevier Ltd., **1999**, 345–370.

[15] A. B. Gaspar, M. Seredyuk, *Coord. Chem. Rev.* **2014**, *268*, 41–58.

[16] P. Gütlich, Y. Garcia, H. Spiering, in *Magn. Mol. to Mater.*, **2003**, 271–344.

[17] L. Cambi, L. Szegö, *Berichte der Dtsch. Chem. Gesellschaft A B Ser.* **1931**, *64*, 2591–2598.

[18] P. Gütlich, Y. Garcia, H. A. Goodwin, *Chem. Soc. Rev.* **2000**, *29*, 419–427.

[19] H. A. Goodwin, *Top. Curr. Chem.* **2004**, *234*, 23–47.

[20] P. Gütlich, A. B. Gaspar, Y. Garcia, *Beilstein J. Org. Chem.* **2013**, *9*, 342–391.

[21] F. Grandjean, G. J. Long, B. B. Hutchinson, L. Ohlhausen, P. Neill, J. D. Holcomb, *Inorg. Chem.* **1989**, *28*, 4406–4414.

[22] J. R. Galán-Mascarós, E. Coronado, A. Forment-Aliaga, M. Monrabal-Capilla, E. Pinilla-Cienfuegos, M. Ceolin, *Inorg. Chem.* **2010**, *49*, 5706–5714.

[23] C.-F. Sheu, S. M. Chen, G.-H. Lee, Y. H. Liu, Y.-S. Wen, J. J. Lee, Y.-C. Chuang, Y. Wang, *Eur. J. Inorg. Chem.* **2013**, *2013*, 894–901.

[24] Y. Garcia, P. Gütlich, *Spin Crossover Transit. Met. Complexes II* **2004**, 49–62.

[25] P. Gütlich, E. Bill, A. X. Trautwein, *Mössbauer Spectroscopy and Transition Metal Chemistry*, Springer Science & Business Media, **2013**.

[26] M. G. Cowan, J. Olguín, S. Narayanaswamy, J. L. Tallon, S. Brooker, *J. Am. Chem. Soc.* **2012**, *134*, 2892–2894.

[27] B. Warner, J. C. Oberg, T. G. Gill, F. El Hallak, C. F. Hirjibehedin, M. Serri, S. Heutz, M.-A. Arrio, P. Sainctavit, M. Mannini, et al., *J. Phys. Chem. Lett.* **2013**, *4*, 1546–1552.

[28] A. Cannizzo, C. J. Milne, C. Consani, W. Gawelda, C. Bressler, F. van Mourik, M. Chergui, *Coord. Chem. Rev.* **2010**, *254*, 2677–2686.

[29] S. Decurtins, P. Gütlich, C. P. Köhler, H. Spiering, A. Hauser, *Chem. Phys. Lett.* **1984**, *105*, 1–4.

[30] J.-F. Létard, *J. Mater. Chem.* **2006**, *16*, 2550–2559.

[31] S. Hayami, Z. Z. Gu, Y. Einaga, Y. Kobayasi, Y. Ishikawa, Y. Yamada, A. Fujishima, O. Sato, *Inorg. Chem.* **2001**, *40*, 3240–3242.

[32] L. Salmon, G. Molnár, S. Cobo, P. Oulié, M. Etienne, T. Mahfoud, P. Demont, A. Eguchi, H. Watanabe, K. Tanaka, *New J. Chem.* **2009**, *33*, 1283–1289.

[33] M. Shatruk, H. Phan, B. A. Chrisostomo, A. Suleimenova, *Coord. Chem. Rev.* **2015**, *289–290*, 62–73.

[34] M. Griffin, S. Shakespeare, H. J. Shepherd, C. J. Harding, J.-F. Létard, C. Desplanches, A. E. Goeta, J. A. K. Howard, A. K. Powell, V. Mereacre, *Angew. Chemie - Int. Ed.* **2011**, *50*, 896–900.

[35] M. K. Panda, T. Runčevski, S. C. Sahoo, A. A. Belik, N. K. Nath, R. E. Dinnebier, P. Naumov, S. Chandra Sahoo, A. A. Belik, N. K. Nath, *Nat. Commun.* **2014**, *5*, 4811.

[36] A. I. Vicente, A. Joseph, L. P. Ferreira, M. de D. Carvalho, V. H. Rodrigues, M. Duttine, H. P Diogo, M. Eduardo Minas da Piedade, M. J. Calhorda, P. N. Martinho, *Chem. Sci.* **2016**, *7*, 4251-4258.
[37] W. Phonsri, D. J. Harding, P. Harding, K. S. Murray, B. Moubaraki, I. A. Gass, J. D. Cashion, G. N. L. Jameson, H. Adams, *Dalt. Trans.* **2014**, *43*, 17509–17518.
[38] W. Phonsri, D. S. Macedo, C. G. Davies, G. N. L. Jameson, B. Moubaraki, K. S. Murray, *Dalt. Trans.* **2017**, *46*, 7020–7029.
[39] W. Phonsri, D. S. Macedo, K. R. Vignesh, G. Rajaraman, C. G. Davies, G. N. L. Jameson, B. Moubaraki, J. S. Ward, P. E. Kruger, G. Chastanet, *Chem. - A Eur. J.* **2017**, *23*, 7052–7065.
[40] H. S. Scott, B. Moubaraki, N. Paradis, G. Chastanet, J.-F. Létard, S. R. Batten, K. S. Murray, *J. Mater. Chem. C* **2015**, *3*, 7845–7857.
[41] W. Zhang, F. Zhao, T. Liu, M. Yuan, Z.-M. Wang, S. Gao, *Inorg. Chem.* **2007**, *46*, 2541–2555.
[42] M. Sorai, J. Ensling, P. Gütlich, *Chem. Phys.* **1976**, *18*, 199–209.
[43] D. Gentili, F. Liscio, N. Demitri, B. Schäfer, F. Borgatti, P. Torelli, B. Gobaut, G. Panaccione, G. Rossi, A. Degli Esposti, *Dalt. Trans.* **2016**, *45*, 134–143.
[44] D. Sertphon, D. J. Harding, P. Harding, K. S. Murray, B. Moubaraki, J. D. Cashion, H. Adams, *Eur. J. Inorg. Chem.* **2013**, *2013*, 788–795.
[45] J. Tao, R.-J. Wei, R.-B. Huang, L.-S. Zheng, *Chem. Soc. Rev.* **2012**, *41*, 703–737.
[46] I. Šalitroš, O. Fuhr, M. Ruben, *Materials (Basel).* **2016**, *9*, 585–595.
[47] R. J. Wei, B. Li, J. Tao, R. Bin Huang, L. S. Zheng, Z. Zheng, *Inorg. Chem.* **2011**, *50*, 1170–1172.
[48] J. Luan, J. Zhou, Z. Liu, B. Zhu, H. Wang, X. Bao, W. Liu, M. L. Tong, G. Peng, H. Peng, *Inorg. Chem.* **2015**, *54*, 5145–5147.
[49] W. Phonsri, P. Harding, L. Liu, S. G. Telfer, K. S. Murray, B. Moubaraki, T. M. Ross, G. N. L. Jameson, D. J. Harding, *Chem. Sci.* **2017**, *8*, 3949–3959.
[50] M. Fumanal, F. Jiménez-Grávalos, J. Ribas-Arino, S. Vela, *Inorg. Chem.* **2017**, *56*, 4474–4483.
[51] N. Nassirinia, S. Amani, S. J. Teat, O. Roubeau, P. Gamez, *Chem. Commun.* **2014**, *50*, 1003–1005.
[52] M. Sorai, *Top. Curr. Chem.* **2004**, *235*, 153–170.
[53] M. Swart, M. Güell, M. Solà, *Phys. Chem. Chem. Phys.* **2011**, *13*, 10449–10456.
[54] R. G. Parr, W. Yang, *Density-Functional Theory of Atoms and Molecules*, **1989**.
[55] H. Paulsen, A. X. Trautwein, *Top. Curr. Chem.* **2004**, *235*, 197–219.
[56] N. D. M. Hine, J. Dziedzic, P. D. Haynes, C.-K. Skylaris, *J. Chem. Phys.* **2011**, *135*, 204103.
[57] I. Gudyma, V. Ivashko, A. Bobák, *Nanoscale Res. Lett.* **2017**, *12*, 101–106.
[58] S. Grimme, J. Antony, S. Ehrlich, H. Krieg, *J. Chem. Phys.* **2010**, *132*, 154104.
[59] G. Kotliar, S. Y. Savrasov, K. Haule, V. S. Oudovenko, O. Parcollet, C. A. Marianetti, *Rev. Mod. Phys.* **2006**, *78*, 865–951.
[60] J. Kuneš, I. Leonov, P. Augustinský, V. Křápek, M. Kollar, D. Vollhardt, *Eur. Phys. J. Spec. Top.* **2017**, *226*, 2641–2675.
[61] H. Hagiwara, A. Kawano, T. Fujinami, N. Matsumoto, Y. Sunatsuki, M. Kojima, H. Miyamae, *Inorganica Chim. Acta* **2011**, *367*, 141–150.
[62] B. Weber, *Coord. Chem. Rev.* **2009**, *253*, 2432–2449.
[63] A. Arroyave, A. Lennartson, A. Dragulescu-Andrasi, K. S. Pedersen, S. Piligkos, S. A. Stoian, S. M. Greer, C. Pak, O. Hietsoi, H. Phan, *Inorg. Chem.* **2016**, *55*, 5904–5913.
[64] T. M. Ross, S. M. Neville, D. S. Innes, D. R. Turner, B. Moubaraki, K. S. Murray, *Dalton Trans.* **2010**, 149–159.
[65] W. Phonsri, L. Darveniza, S. Batten, K. Murray, *Inorganics* **2017**, *5*, 51.
[66] A. Michalowicz, J. Moscovici, B. Ducourant, D. Cracco, O. Kahn, *Chem. Mater.* **1995**, *7*, 1833–1842.
[67] W. Vreugdenhil, J. H. Van Diemen, R. A. G. De Graaff, J. G. Haasnoot, J. Reedijk, A. M. Van Der Kraan, O. Kahn, J. Zarembowitch, *Polyhedron* **1990**, *9*, 2971–2979.
[68] M. Ohba, K. Yoneda, G. Agusti, M. C. Muñoz, A. B. Gaspar, J. A. Real, M. Yamasaki, H. Ando, Y. Nakao, S. Sakaki, *Angew. Chemie - Int. Ed.* **2009**, *48*, 4767–4771.
[69] S. M. Neville, G. J. Halder, K. W. Chapman, M. B. Duriska, B. Moubaraki, K. S. Murray, C. J. Kepert, *J. Am. Chem. Soc.* **2009**, *131*, 12106–12108.

[70] D. Aravena, Z. A. Castillo, M. C. Muñoz, A. B. Gaspar, K. Yoneda, R. Ohtani, A. Mishima, S. Kitagawa, M. Ohba, J. A. Real, *Chem. - A Eur. J.* **2014**, *20*, 12864–12873.
[71] M. C. Muñoz, J. A. Real, *Coord. Chem. Rev.* **2011**, *255*, 2068–2093.
[72] Z. Yan, W. Liu, Y. Y. Peng, Y. C. Chen, Q. W. Li, Z. P. Ni, M. L. Tong, *Inorg. Chem.* **2016**, *55*, 4891–4896.
[73] D. Y. Wu, O. Sato, Y. Einaga, C. Y. Duan, *Angew. Chemie - Int. Ed.* **2009**, *48*, 1475–1478.
[74] L. Stoleriu, M. Nishino, S. Miyashita, A. Stancu, A. Hauser, C. Enachescu, *Phys. Rev. B* **2017**, *96*, 064115.
[75] A. Sugahara, H. Kamebuchi, A. Okazawa, M. Enomoto, N. Kojima, *Inorganics* **2017**, *5*, 50.
[76] E. J. Devid, P. N. Martinho, M. V. Kamalakar, I. Salitros, Ú. Prendergast, J.-F. Dayen, V. Meded, T. Lemma, F. Evers, R. Gonales-Prieto, *ACS Nano* **2015**, 4496–4507.
[77] A. K. Geim, K. S. Novoselov, *Nat. Mater.* **2007**, *6*, 183–191.
[78] S. Ossinger, H. Naggert, L. Kipgen, T. Jasper-Toennies, A. Rai, J. Rudnik, F. Nickel, L. M. Arruda, M. Bernien, W. Kuch, *J. Phys. Chem. C* **2017**, *121*, 1210–1219.
[79] A. Holovchenko, J. Dugay, M. Giménez-Marqués, R. Torres-Cavanillas, E. Coronado, H. S. J. van der Zant, *Adv. Mater.* **2016**, *28*, 7228–7233.
[80] K. S. Kumar, I. Šalitroš, Z. Boubegtiten-Fezoua, S. Moldovan, P. Hellwig, M. Ruben, *Dalt. Trans.* **2017**, *47*, 35–35.
[81] A. C. Aragonès, D. Aravena, J. I. Cerdá, Z. Acís-Castillo, H. Li, J. A. Real, F. Sanz, J. Hihath, E. Ruiz, I. Díez-Pérez, *Nano Lett.* **2016**, *16*, 218–226.
[82] T. Jasper-Tönnies, M. Gruber, S. Karan, H. Jacob, F. Tuczek, R. Berndt, *J. Phys. Chem. Lett.* **2017**, *8*, 1569–1573.
[83] J. Burgess, M. V. Twigg, in *Encycl. Inorg. Bioinorg. Chem.*, John Wiley & Sons, Ltd, Chichester, UK, **2011**.
[84] K. P. Kepp, *Coord. Chem. Rev.* **2016**, *344*, 363–374.
[85] H. S. Scott, R. W. Staniland, P. E. Kruger, *Coord. Chem. Rev.* **2018**, *362*, 24–43.
[86] D. J. Harding, P. Harding, W. Phonsri, *Coord. Chem. Rev.* **2016**, *313*, 38–61.
[87] A. B. Koudriavtsev, A. F. Stassen, J. G. Haasnoot, M. Grunert, P. Weinberger, W. Linert, *Phys. Chem. Chem. Phys.* **2003**, *5*, 3666–3675.
[88] F. F. Martins, A. Joseph, H. P. Diogo, M. E. Minas da Piedade, L. P. Ferreira, M. de D. Carvalho, S. Barroso, M. J. Romão, M. J. Calhorda, P. N. Martinho, *Eur. J. Inorg. Chem.* **2018**, *2018*, 2976–2983.
[89] E. Ruiz, J. Cano, S. Alvarez, P. Alemany, *J. Comput. Chem.* **1999**, *13*, 1391-1400.
[90] O. Kahn, *Molecular Magnetism*, VHC Publishers, Inc., New York, **1942**.
[91] L. Zhang, J.-J. Wang, G.-C. Xu, J. Li, D.-Z. Jia, S. Gao, *Dalt. Trans.* **2013**, *42*, 8205.
[92] G. A. Dorofeev, A. N. Streletskii, I. V. Povstugar, A. V. Protasov, E. P. Elsukov, *Colloid J.* **2012**, *74*, 675–685.
[93] J. Turkevich, P. C. Stevenson, J. Hillier, *Discuss. Faraday Soc.* **1951**, *11*, 55.
[94] E. J. Devid, Exploring Charge Transport Properties and Functionality of Molecule-Nanoparticle Ensembles, Universiteit Leiden, **2015**.
[95] P. U. Naik, G. J. McManus, M. J. Zaworotko, R. D. Singer, *Dalt. Trans.* **2008**, *0*, 4834.
[96] L. J. Farrugia, *J. Appl. Crystallogr.* **2012**, *45*, 849–854.
[97] C. F. Macrae, P. R. Edgington, P. McCabe, E. Pidcock, G. P. Shields, R. Taylor, M. Towler, J. van De Streek, *J. Appl. Crystallogr.* **2006**, *39*, 453–457.
[98] G. te Velde, F. M. Bickelhaupt, E. J. Baerends, C. Fonseca Guerra, S. J. A. van Gisbergen, J. G. Snijders, T. Ziegler, *J. Comput. Chem.* **2001**, *22*, 931–967.
[99] C. Fonseca Guerra, J. G. Snijders, G. Te Velde, E. J. Baerends, *Theor. Chem. Acc.* **1998**, *99*, 391–403.
[100] "ADF2013, SCM, Theoretical Chemistry, Vrije Universiteit, Amsterdam, The Netherlands, http://scm.com,"
[101] S. H. Vosko, L. Wilk, M. Nusair, *Can. J. Phys.* **1980**, *58*, 1200–1211.
[102] M. Reiher, O. Salomon, B. A. Hess, *Theor. Chem. Acc.* **2001**, *107*, 48–55.
[103] O. Salomon, M. Reiher, B. A. Hess, *J. Chem. Phys.* **2002**, *117*, 4729–4737.
[104] E. van Lenthe, A. Ehlers, E.-J. Baerends, *J. Chem. Phys.* **1999**, *110*, 8943–8953.
[105] E. van Lenthe, E. J. Baerends, *J. Comput. Chem.* **2003**, *24*, 1142–1156.

[106] Chemcraft Program. http://chemcraftprog.com/index.html [last acessed 22.08.2016]. G. A. Andrienko, **2016**.
[107] E. Gmelin, S. M. Sarge, *Pure Appl. Chem.* **1995**, *67*, 1789–1800.

6 Supporting information

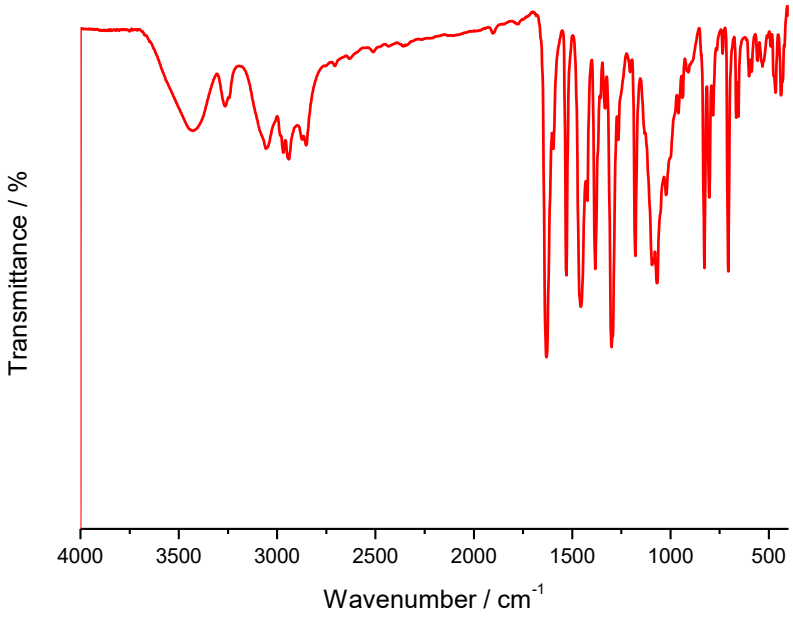

Figure 6.1 *FTIR spectrum for complex* ***M2****.*

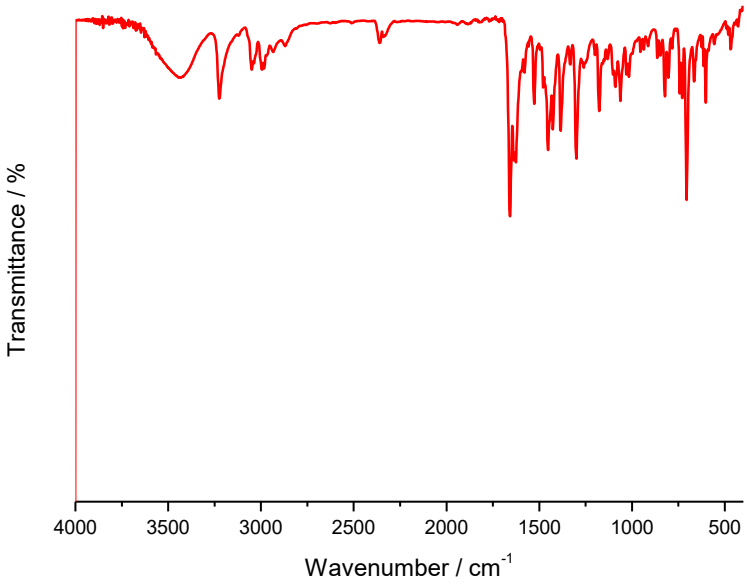

Figure 6.2 *FTIR spectrum for complex* ***M4****.*

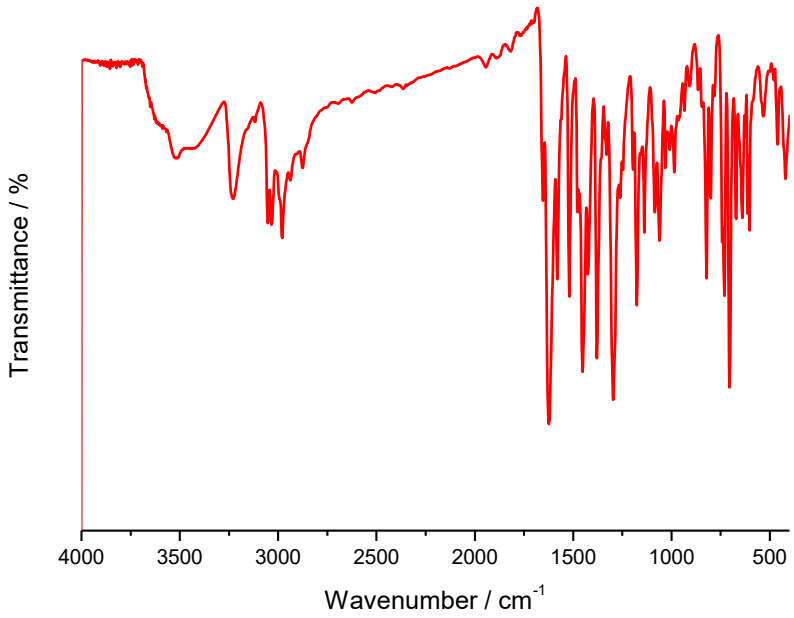

Figure 6.3 *FTIR spectrum for complex* ***M5****.*

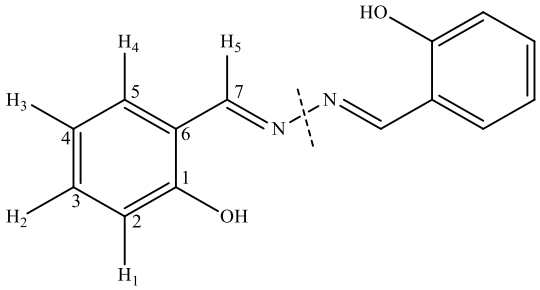

Scheme 6.1 *Numbering scheme for* L_1*.*

Table 6.1 *^{1}H NMR peaks obtained for* L_1 *(s=singlet, d=doublet, t=triplet).*

	^1H *NMR*	H_1	H_2	H_3	H_4	H_5
L_1	Multiplicity	d	t	t	d	s
	Chemical shift / ppm	6.99	7.40	6.98	7.70	9.00

Table 6.2 *^{13}C APT NMR peaks obtained for* L_1*.*

	^{13}C *APT*	C_1	C_2	C_3	C_4	C_5	C_6	C_7
L_1	Chemical shift / ppm	159	120	134	117	131	118	163

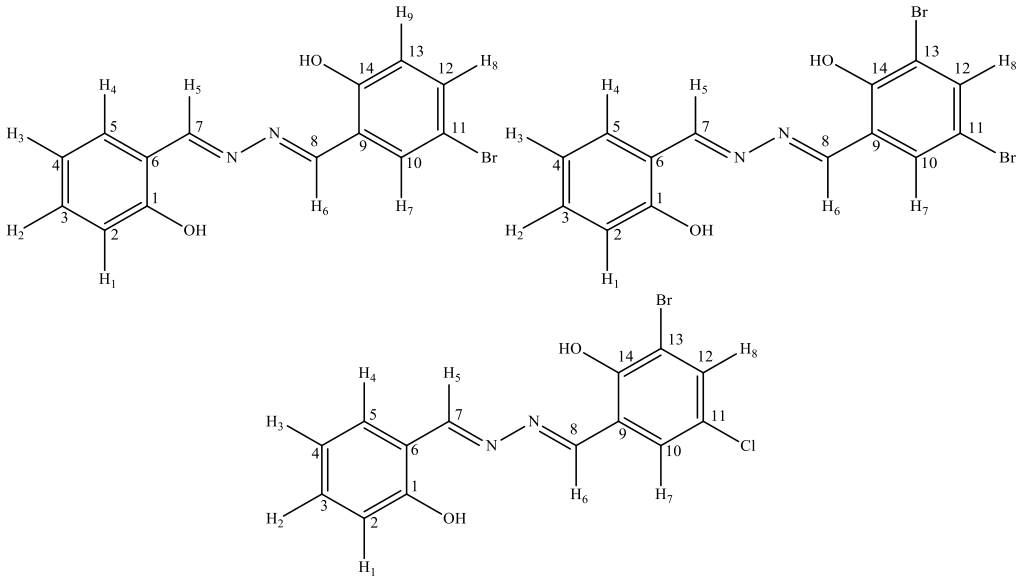

Scheme 6.2 *Numbering scheme for the asymmetric ligands L_2 (top left), L_3 (top right) and L_4 (bottom).*

Table 6.3 *^{1}H NMR peaks obtained for the asymmetric ligands L_2, L_3 and L_4 (s=singlet, d=doublet, t=triplet).*

	^{1}H NMR	*H_1*	*H_2*	*H_3*	*H_4*	*H_5*	*H_6*	*H_7*	*H_8*	*H_9*
L_2	Multiplicity	d	t	t	d	s	s	s	d	d
	Chemical shift / ppm	6.97	7.40	6.98	7.70	9.01	8.93	7.90	7.53	6.96
L_3	Multiplicity	d	t	t	d	s	s	s	s	---
	Chemical shift / ppm	6.99	7.42	6.97	7.72	9.08	8.97	7.88	7.93	---
L_4	Multiplicity	d	t	t	d	s	s	s	s	---
	Chemical shift / ppm	6.99	7.42	6.96	7.73	9.09	8.99	7.77	7.86	---

Table 6.4 *^{13}C APT NMR peaks obtained for L_2, L_3 and L_4.*

	^{13}C APT	*C_1*	*C_2*	*C_3*	*C_4*	*C_5*	*C_6*	*C_7*	*C_8*	*C_9*	*C_{10}*	*C_{11}*	*C_{12}*	*C_{13}*	*C_{14}*
L_2	Chem. shift / ppm	159	---	133	---	131	118	163	160	121	132	111	135	---	158
L_3	Chem. shift / ppm	158	116	134	119	130	118	163	162	110	134	120	137	112	154
L_4	Chem. shift / ppm	159	117	134	120	130	120	164	163	111	131	123	135	118	155

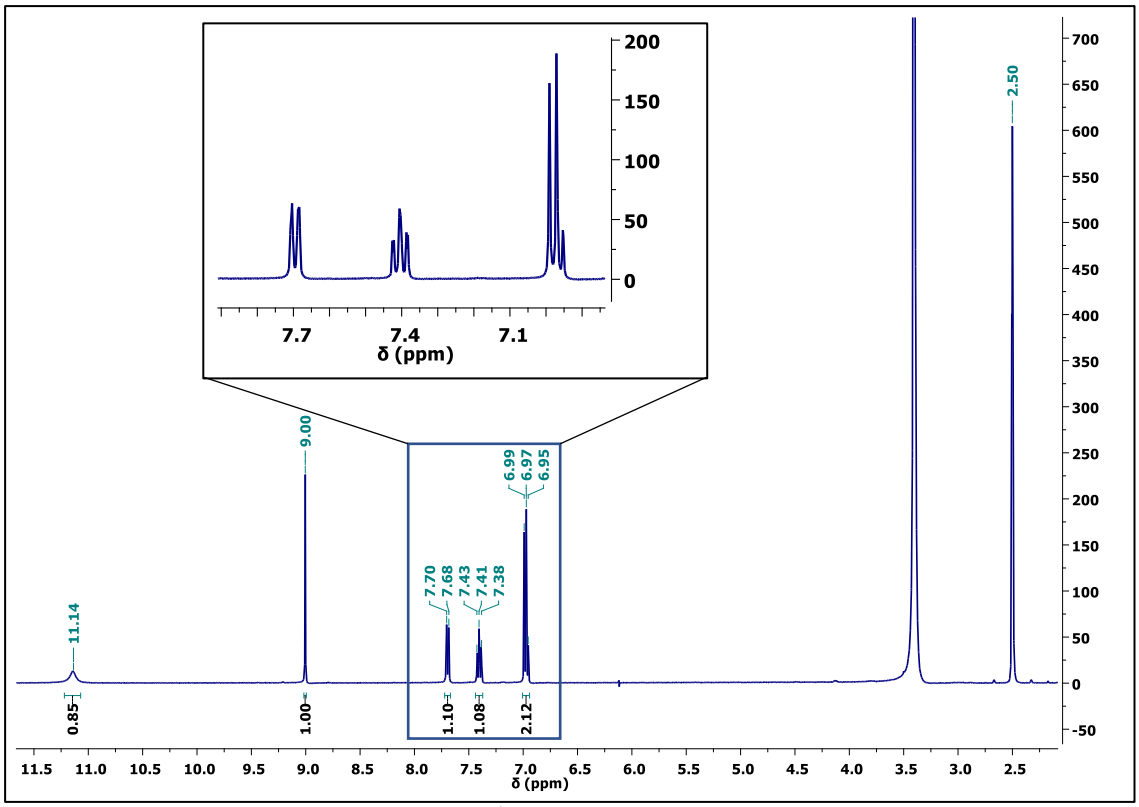

Figure 6.4 *^{1}H NMR spectrum obtained for L_1.*

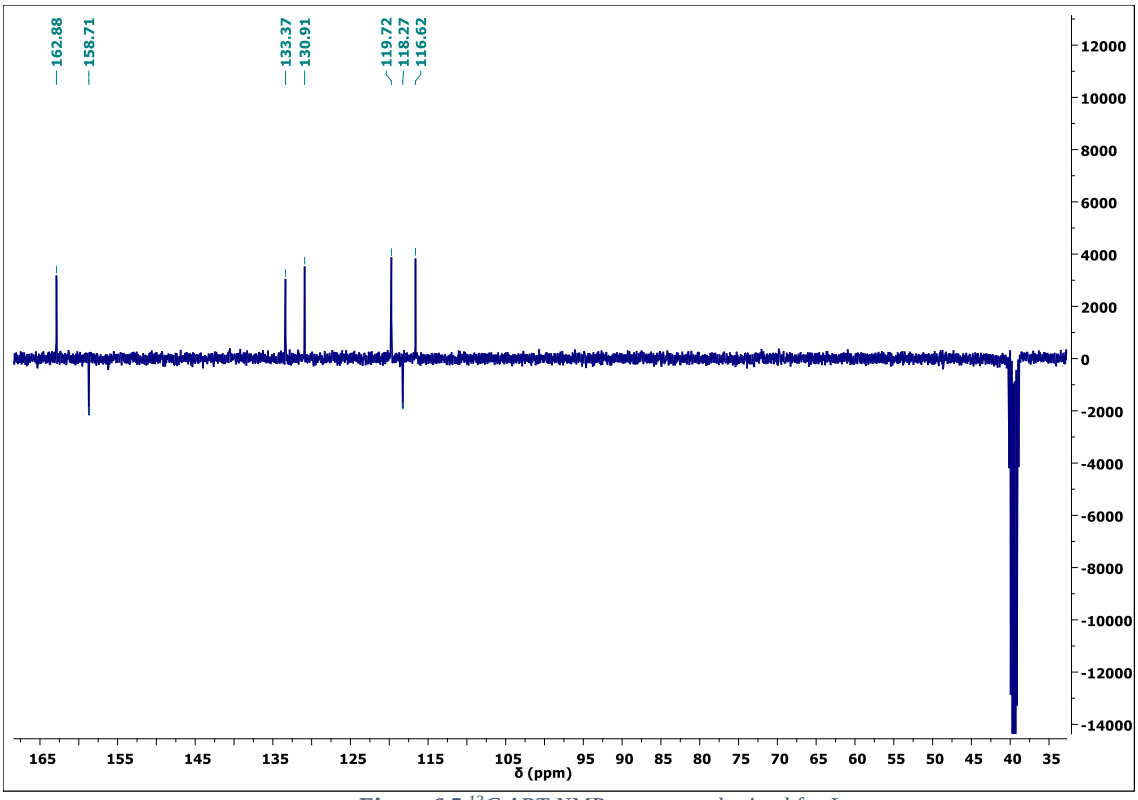

Figure 6.5 *^{13}C APT NMR spectrum obtained for L_1.*

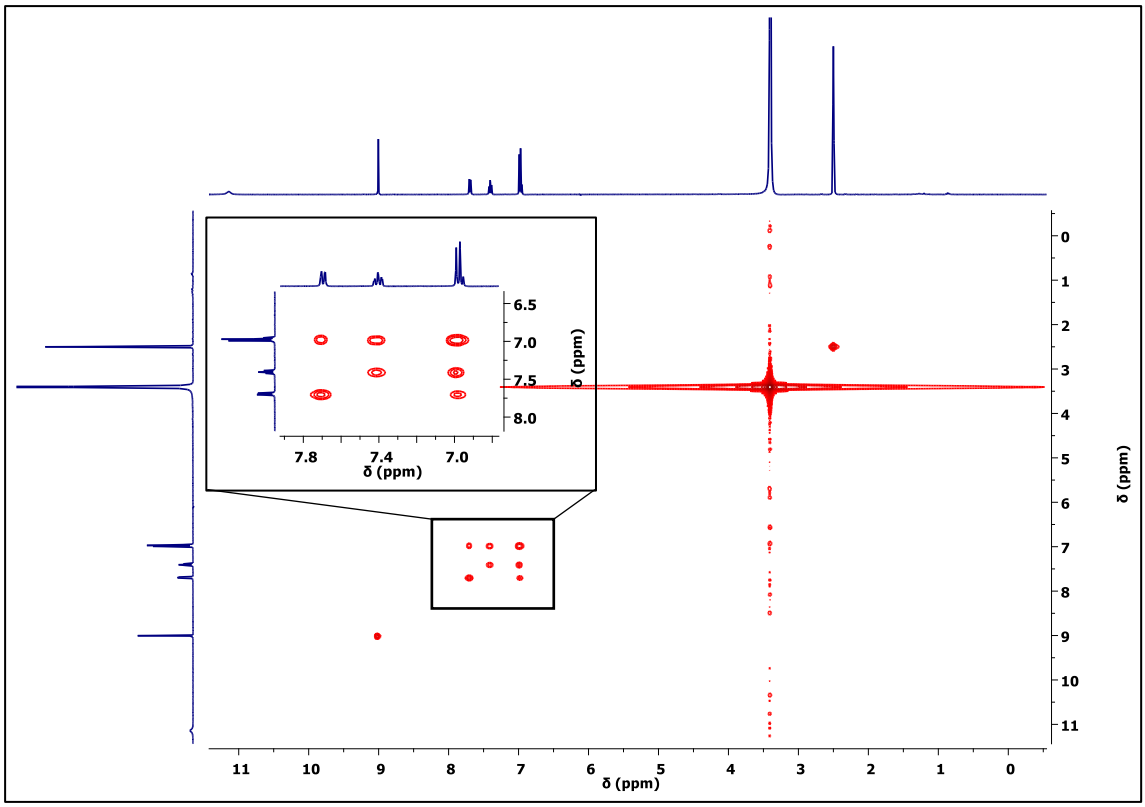

Figure 6.6 *COSY NMR spectrum obtained for L_1.*

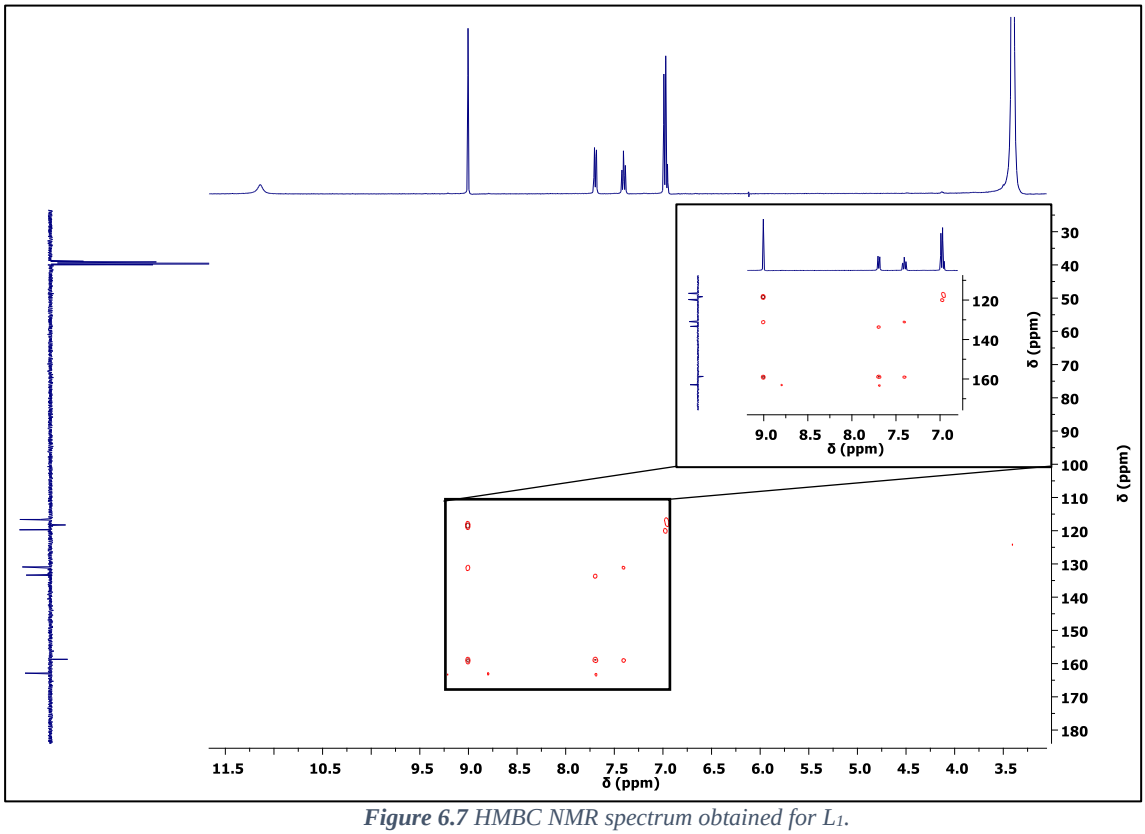

Figure 6.7 *HMBC NMR spectrum obtained for L_1.*

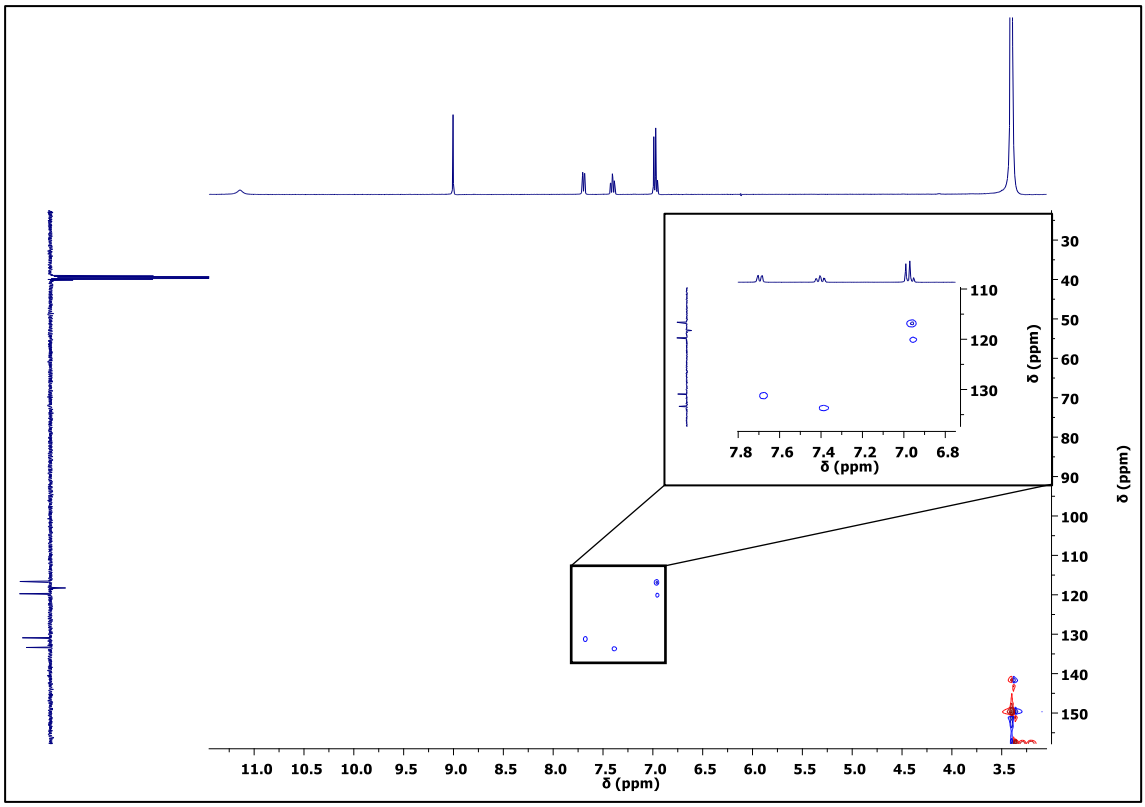

Figure 6.8 *HSQC NMR spectrum obtained for L_1.*

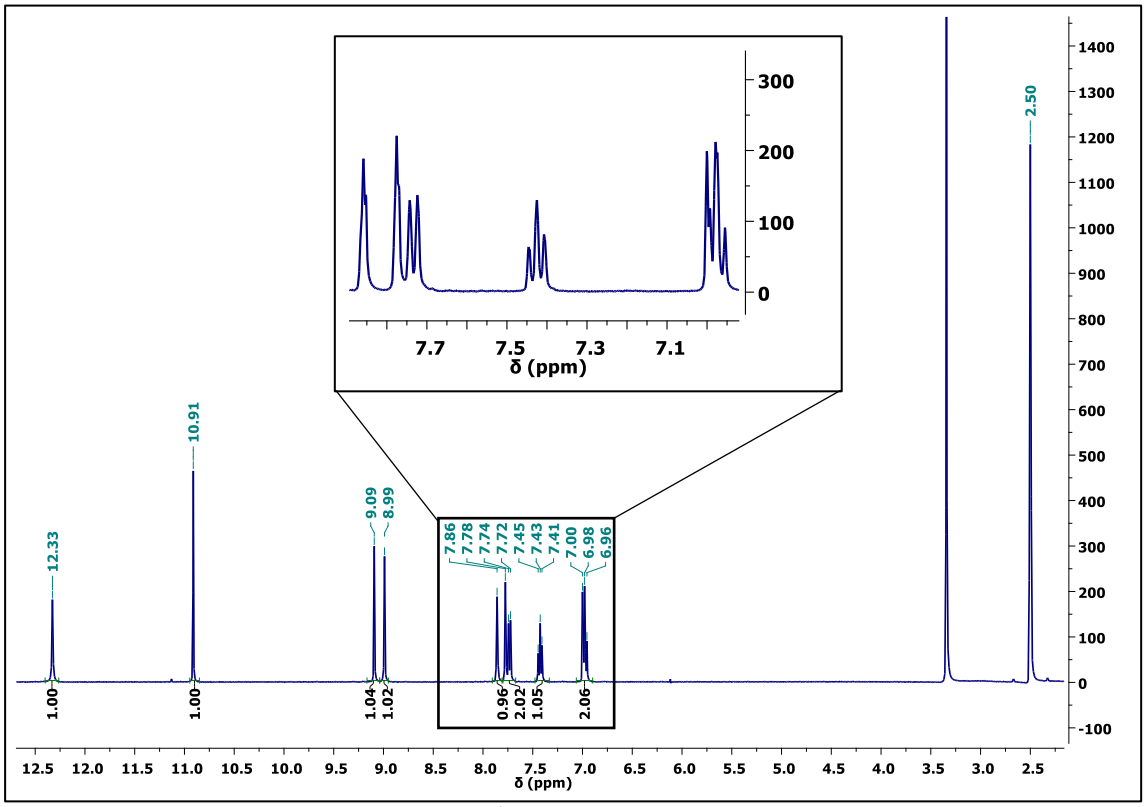

Figure 6.9 *^{1}H NMR spectrum obtained for L_4.*

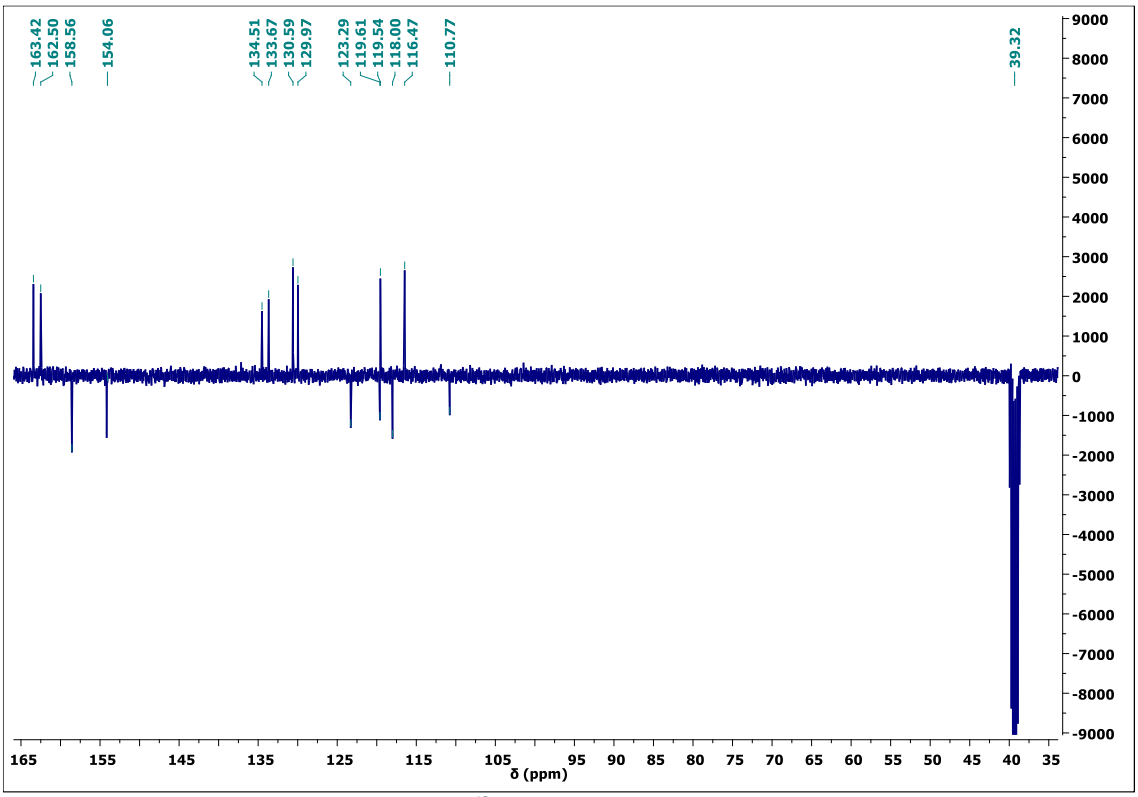

Figure 6.10 *^{13}C APT NMR spectrum obtained for L4.*

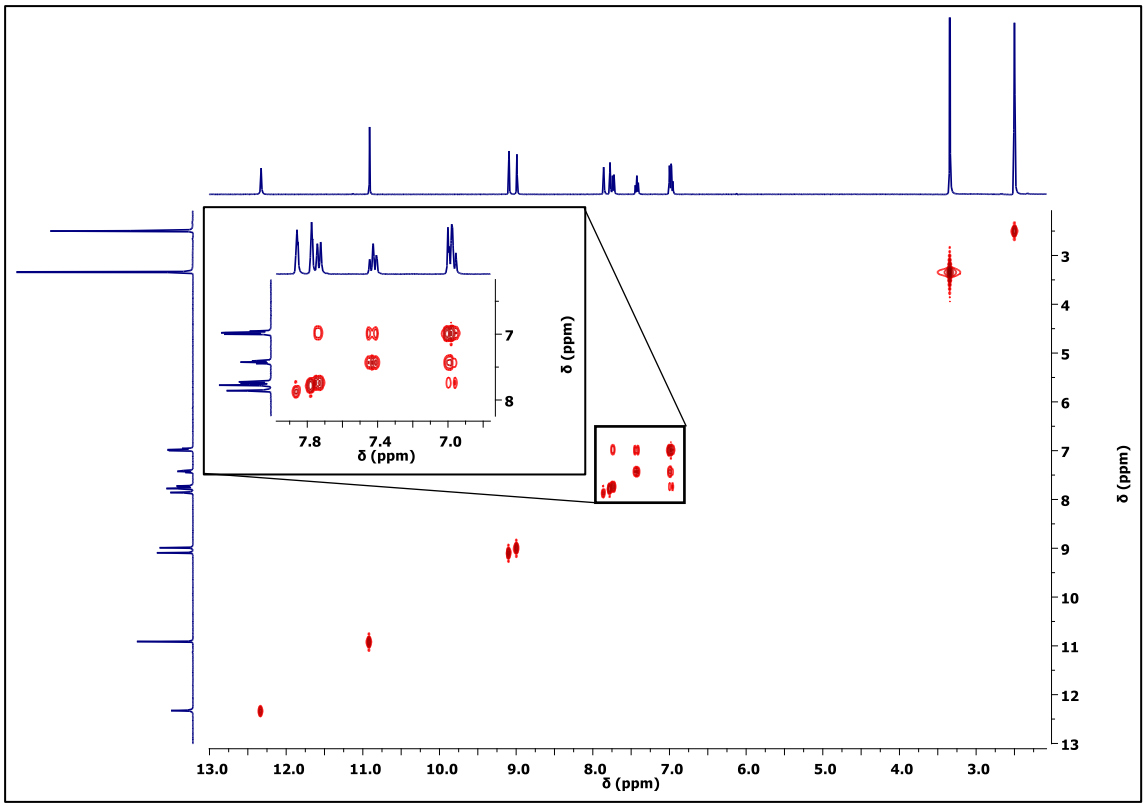

Figure 6.11 *COSY NMR spectrum obtained for L4.*

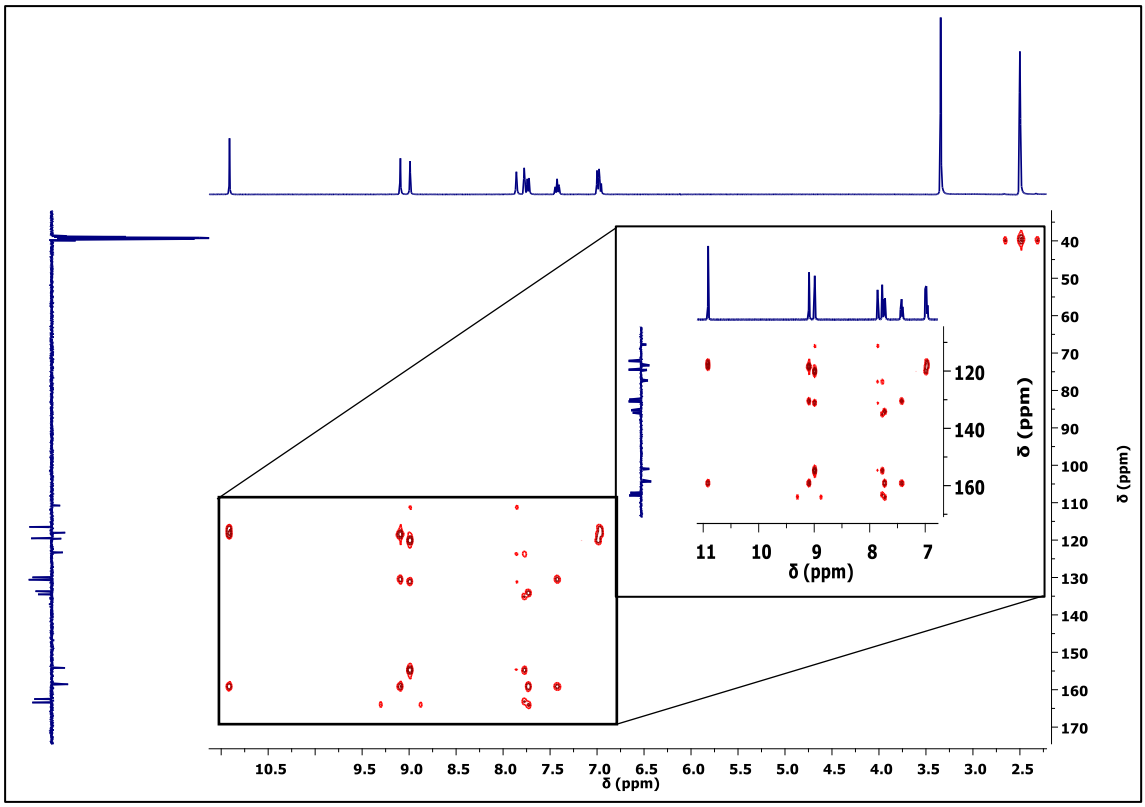

Figure 6.12 *HMBC NMR spectrum obtained for L4.*

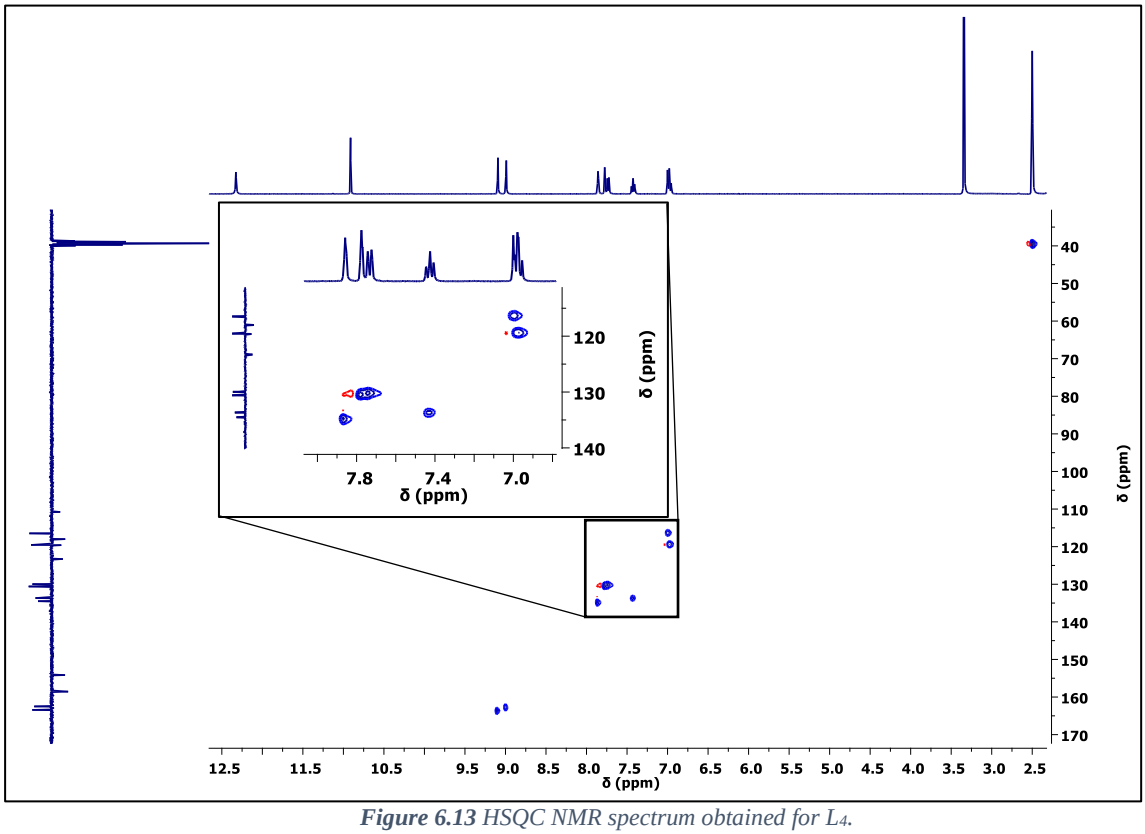

Figure 6.13 *HSQC NMR spectrum obtained for L4.*

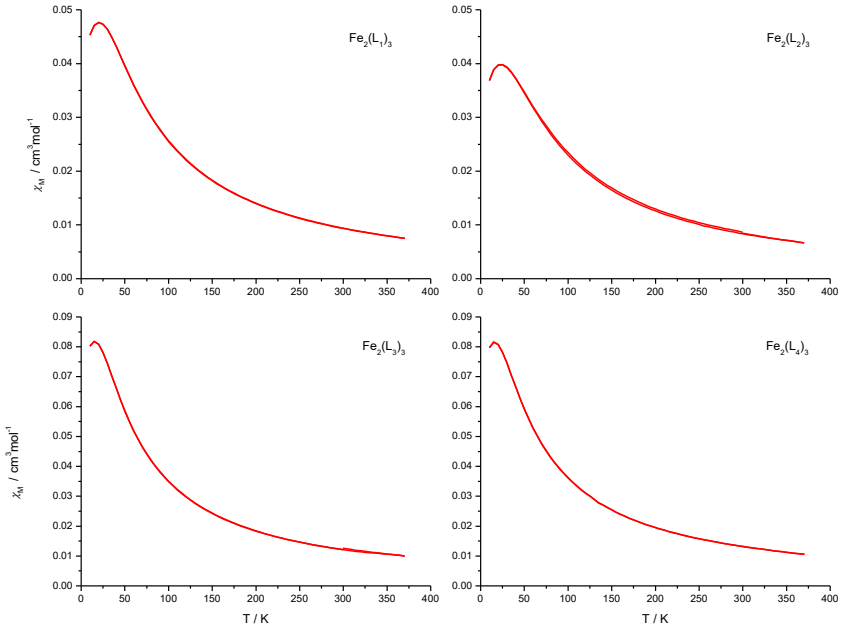

Figure 6.14 *χ_M vs T plots for the $Fe_2(L_x)_3$ compounds.*

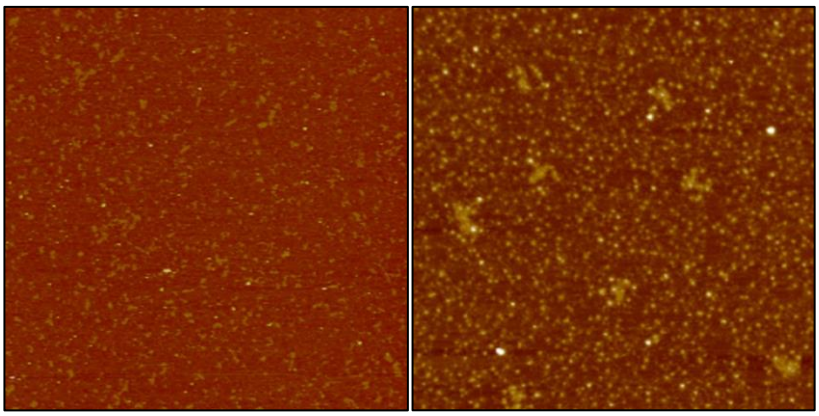

Figure 6.15 *AFM images of the particles synthesised with 0.70 (left) and 1.00 (right) PEG. Window sizes are 3x3 μm.*

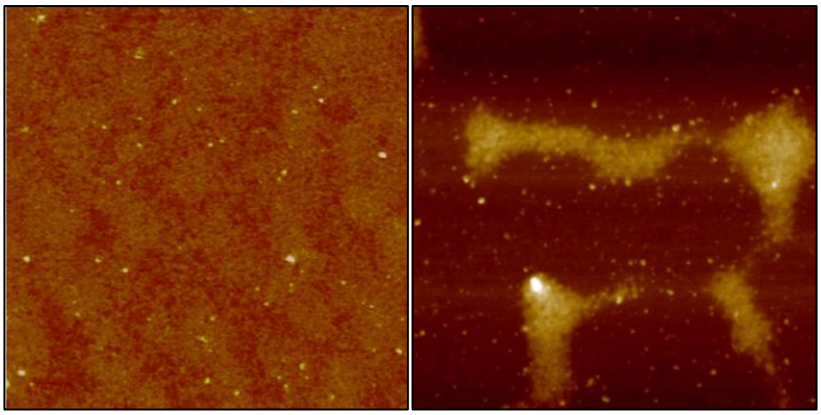

Figure 6.16 *AFM images of the particles synthesised with 1.50 (left) and 2.00 (right) PEG. Window sizes are 1x1 μm.*